Impurity Control by Intrinsic and Pellet Induced Instabilities in Fusion Devices
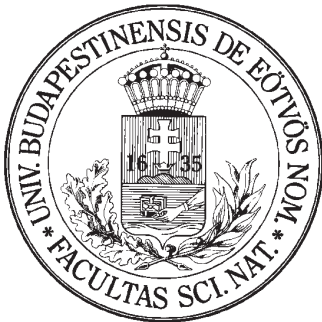
Eva Belonohy
MTA KFKI RMKI

PhD Thesis

[2011] | ELTE TTK

Contents

Chapter 1

Introduction to Fusion

In the dawn of humanity man has learned how to control fire and make his life easier. Since then progresses of mankind were coupled to discovery and domestication of new energy resources and technical advances. Now, at the beginning of the 21st century we are learning to control fusion plasma, the energy source of our Sun, and aim at demonstrating the use of controlled thermonuclear fusion in the first International Experimental Thermonuclear Reactor, ITER.

This chapter provides an introduction to basic plasma physics and fusion concepts aimed at readers new to this captivating field. It is by no means meant to be comprehensive, rather aims to provide a glossary for concepts used in the forthcoming chapters. A good introduction to the field of fusion plasma physics can be found in [1-3] The experimental and theoretical background will be presented in Chapter 2, whereas Chapter 3 will introduce the plasma diagnostics and the respective analytical methods used in the thesis before moving on to the main results in the following two chapters. Major abbreviations have been collected under *Notations* at the end of the thesis for quick reference including a short explanation and the page number where they had been first introduced. Please use this as a reference guide as well as the cited articles and books when encountering unknown concepts or diagnostics.

1.1 The energy problem

Energy powers the modern world. Our technological society uses an enormous amount of energy that is expected to double/triple in the present century (figure 1-1). Furthermore the projected population growth coupled with the increasing advances of the developing countries make it a great challenge to provide clean, safe and affordable energy resources in the coming years. Fossil fuels - as gas, coil, oil - formed millions of years ago from the remains of prehistoric plants and animals, make about 80% of our energy. By burning these fuels, the

generated carbon-dioxide (CO_2) retains the heat of earth in the atmosphere (greenhouse effect) that led to an increase of 0.6° C in Earth's average temperature in the last century and at present trend is expected to increase to 1.1-6.4° C by the end of this century [4]. The Green-house effect results in extreme weather conditions as heavy storms and intense heat waves in addition to the use of fossil fuels causing acid rains and health degenerating smog in major cities. Fossil fuels are furthermore not evenly distributed around the world (70% in the Middle East) leading to political tension and many countries seeking energy independence. Finally at present's rate of use, fossil fuels will run out eventually – oil (~40 years), gas (~50 years) and coil (~300 years) [5].
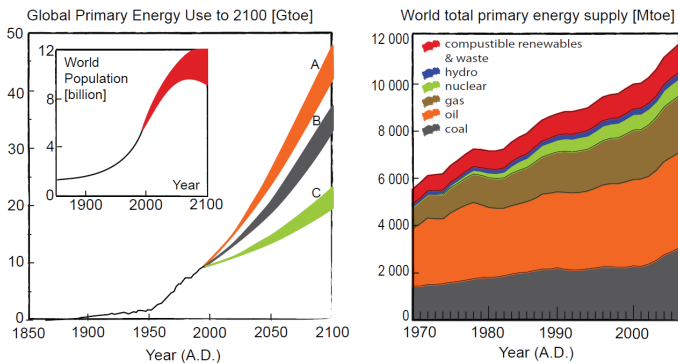
Figure 1-1 *Global energy consumption from 1850 including prediction to 2100 for three scenarios and the world total primary energy supply by energy carrier from 1971 [source: EFDA CSU]*

In order to preserve our environment, we need to find and develop alternative energy sources that do not emit CO_2. At present alternative energy resources include nuclear energy from fission (5.8%[1]) and renewable energy resources as biomass and waste (10.0%[1]), Hydropower (2.2%[1]) as well as wind, solar and geothermal energy (together 0.7%[1]) [6]. Although there is a fast development of renewable energy resources in the last years, it will take decades until they can produce a reasonable share of our energy consumption and it is unlikely that they could ever deliver majority of the energy demand. Fission although inevitable at present, has some disadvantages due to its safety, radioactive waste, availability of Uranium and political issues. A developing competitive future energy concept is fusion

---

[1] Percentage of the present total primary energy resources in the world.

power. Fusion is a clean, safe and durable energy source that would nicely complement the renewable energy resources in the energy mix in the future.

1.2 Fusion

Fusion is the process in which two light atomic nuclei fuse together releasing a large amount of energy coming from the strong force binding the atomic nuclei. On Earth, the most promising fusion concept for energy production is based on the reaction of two light atomic nuclei, the Hydrogen isotopes Deuterium (D, $_1H^2$) and Tritium (T, $_1H^3$) to generate energy by forming an α-particle Helium (α, $_2He^4$) and a neutron (n, $_0n^1$). This reaction proceeds at the highest rate for the lowest temperature among the candidate reactions.

$$\text{Fusion reaction:} \qquad D + T \quad \rightarrow \quad \alpha\ (3.52\ MeV) \ + n\ (14.1\ MeV) \qquad (1\text{-}1)$$
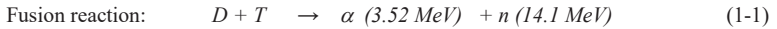
Deuterium, the first fusion reaction element can be found in ordinary water (35mg D in 1 litre water). The other fusion reaction element Tritium, being a radioactive element with a short half-life of only 12.3 years, does not occur in nature in reasonable quantities. Tritium thus will have to be created from Lithium using the neutron produced in the fusion reactions. The procedure is called **Tritium breeding** creating another α-particle as well in the process.

$$\text{Tritium breeding:} \qquad _3Li^6 \ + \ n_{slow} \quad \rightarrow \quad T \ + \ \alpha \qquad (+\ 4.8\ MeV) \qquad (1\text{-}2)$$
$$_3Li^7 \ + \ n_{fast} \quad \rightarrow \quad T \ + \ \alpha \ + n \qquad (-\ 2.5\ MeV) \qquad (1\text{-}3)$$
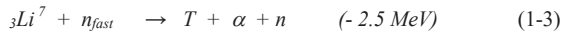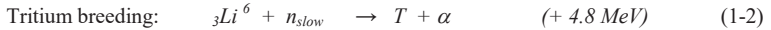
Lithium can be found in huge amounts both in Earth's crust and in the world seas (7.4% Li^6 and 92.6% Li^7). The primary fuels of fusion are thus in fact Deuterium and Lithium, and they are available abundantly around the world, thereby providing energy independence. They are present in enough quantities to meet the energy demand for millions of years (10 mg D and 15 mg T is required to provide energy for the whole lifetime of a single citizen of a developed country).

Another attractive property of fusion is that it is inherently safe. No runaway reaction is possible as the fusion reaction stops in seconds if fuel is not continuously supplied to the reactor or the sensitive fusion conditions cease. Regarding environmental issues no Greenhouses gases are emitted, as the only gas produced by the fusion reaction is Helium, a harmless and inert gas found also in Earth's atmosphere. There is also no external radiation hazard as the primary fuels of a fusion reactor, Deuterium and Lithium are both non-

3

radioactive elements. The Tritium breeding takes place inside the reactor, thus no transport of the radioactive Tritium is needed during operation, except for a very small amount for the first start-up. Even in the worst conceivable scenario the released amount of the radioactive material would be so small, that evacuation of the near-bye population would not be required. During operation, the first-wall elements and the vessel of the fusion power plant are activated by the neutrons produced in the fusion reaction. By using low-activation materials, this radiation lifetime can be reduced to about a 100 years, thus there would be no burden on future generations.

The success or failure of a fusion reactor is closely tied to three essential parameters: **temperature** (T)**, density** (n) **and confinement time** (τ). In a simple zero-dimensional steady state analysis of the energy balance in D-T mixture, the continuous loss of energy (P_{loss}) is balanced by the plasma heating ($P_{heating}$) and the power of the fusion generated α-particles (P_α).

$$\text{Power balance:} \qquad P_{loss} = P_{heating} + P_\alpha \tag{1-4}$$

The power loss term is defined by the ratio of the thermal energy (W) of the plasma to its energy confinement time (τ_E), a quantity characterizing the loss rate due to both radiation and transport processes such as diffusion, convection, charge exchange and others.

$$\text{Energy loss term:} \qquad P_{loss} = \frac{W}{\tau_E} \qquad \text{where } W = \int_V 3 \cdot n \cdot T \cdot d^3 x \tag{1-5}$$

Here we assume that the D-T mixture is in quasineutral plasma state with equal temperature for electrons and ions. For D-T reaction the highest thermonuclear power per unit volume is obtained when the Deuterium density (n_D) equals the Tritium density (n_T). Based on the mass ratio, four fifth of the reaction energy is carried by the neutron (leaving the plasma without any interaction) and one fifth by the α-particle, that is confined by the magnetic field and thus transfers its energy through collisions to the plasma.

$$\alpha\text{-particle term:} \qquad P_\alpha = \int_V \frac{1}{4} n^2 \cdot \langle \sigma \cdot \overline{v} \rangle \cdot \varepsilon_\alpha d^3 x \tag{1-6}$$

where the ion density is $n = n_D + n_T$, ε is the energy per reaction, $\varepsilon_\alpha = \varepsilon / 5$ is the energy of the a-particle per fusion reaction, and $\langle \sigma \cdot \overline{v} \rangle$ is the mean D-T reaction rate per unit density for reaction cross-section (σ) and relative velocity of species (**v**).

The fusion reactor becomes self-sustaining without further applied heating when enough energy is retained from collisions with the generated α-particles. This condition, when $P_{loss}=P_\alpha$ is called **ignition** (by analogy with burning of fossil fuels). To reach ignition sufficiently high energy is required, where D-T ion collisions release energy at a high enough rate. This happens around particle energies of 10-20 keV where the reaction rate can be approximated as $\langle \sigma \cdot \bar{v} \rangle = 1.1 \cdot 10^{-24} T^2$ $m^3 s^{-1}$. The power balance gives the condition for the ignition in form of the **fusion triple product**, assuming homogenous density and temperature for simplicity (valid only in the 10-20keV range as at about 50keV the reaction rate reaches its maximum and the temperature stops increasing):

Fusion triple product (D-T reaction): $n \cdot T \cdot \tau_E > 3 \cdot 10^{21}$ m^{-3} keV s (1-7)

The ignition condition sets the requirements on density, temperature and confinement time as the product of these three key quantities needs to be kept high. Their importance can be easily understood. Nuclei mutually repel each other due to their positive charge, but on the other hand they have to come into a very close vicinity of each other for the strong force acting on the nucleus to take over and make them fuse. Thus in order to prevail over the electrical repulsive force, the particles need to collide with very large velocities, that is provided by high temperatures in fusion. The actual temperature[2] is in reality (~10keV) less than required to overcome the Coulomb barrier (~500 keV) due to quantum mechanical tunnelling and the reacting high energy tail of the particles' Maxwellian distribution. On the other hand to achieve conditions for suitable amount of fusion reactions an appropriate amount of fusion material is necessary and the energy losses have to be kept sufficiently low. Thus the density and confinement time are equally important.

Typical values of the triple product variables can be $n = 10^{20}$ m^{-3}, $T = 10$ keV and $\tau_E = 3$ s. Although the required values for the triple product have all been reached in fusion devices, they have not been reached in the same experiment. The aim of the fusion experiments and their operational regimes are to maximise the fusion product and reach this value in a single experiment.

---

[2] In plasma physics temperature is commonly given in electron volts (1eV=11 605 K), as the average energy of the plasma particles is about $k_B \cdot T$, where k_B is the Boltzmann constant.

1.3 Theoretical description of plasmas

At temperatures well below the one required by the ignition condition, molecules fall apart into atoms, and atoms into free nuclei and free electrons. This state is called **plasma**[3], the fourth state of matter. 99% of the visible universe is in this state, mostly making up stars and nebulae in between. On Earth plasmas include lightning, flames, the Aurora Borealis, fluorescent light tubes or plasma screens using tiny plasma discharges. At high temperatures plasmas are practically composed of charged particles only and thus can be confined by magnetic fields. Characteristic parameters of present magnetically confined fusion plasmas are summarized in table 1-1.

Table 1-1 Typical characteristic parameters of fusion plasmas in magnetic devices

	Fusion plasmas
Density	10^{19}-10^{21} m^{-3}
Temperature	10-40 keV, >150 million K [Sun core: 15 million K]
Pressure	0.1 – 5 atmospheres
Magnetic Field	1-5 T
Plasma Volume	1-100 m^3

Plasma is an ionized gas, composed of mainly electrons, ions, and some neutral particles. Similar to normal gas, its key parameters are plasma density and temperature. It however differs in two basic characteristics, its charge and high electrical conductivity. Its high charge density results in quasineutrality as any significant separation of its species leads to large restoring electrostatic forces. The current resulting from the relative drift of the electrons and ions may provide an important part of the confining magnetic field (in some devices) and crossing the magnetic field, the formed magnetic force balances the plasma pressure gradient. These properties are also commonly defined as collective behaviour of the plasma, where the fields generated by the motion of the charged particles affect the motion of the other charged particles far away.

Plasma dynamics is governed by the self-consistent interaction of large number of charged particles and electromagnetic fields. In principle to define the time evolution: a) given the trajectory ($\mathbf{x}_{(t)}$) and velocity ($\mathbf{v}_{(t)}$) of every particle, the electric ($\mathbf{E}_{(\mathbf{x},t)}$) and magnetic

---

[3] Greek word for 'molded' or 'formed'. It was first introduced by the Czech Jan Evangelista Purkinje to describe the clear fluid remaining after removal of all corpuscular material in blood. In 1922 Irvin Langmuir proposed that electrons, ions and neutrals of ionized gas could be similarly considered as corpuscular bodies in a kind of fluid medium and called this plasma.

field ($\mathbf{B}_{(\mathbf{x},t)}$) can be calculated using Maxwell's equations, whereas simultaneously b) the forces on every particle can be calculated given the instantaneous electric and magnetic field from the Lorentz equation used to update the particle trajectories and velocities. Although this is a clear concept, it is impractical to implement mainly due to the statistically large number of particles. In practice instead of evaluating the whole complex behaviour of the system, the studies focus on a particular phenomenon and model a limited range of behaviour with a specific point of view. The understanding of the plasma is then developed from the different point of views describing a wide range of observed phenomena.

In the **kinetic theory** instead of keeping track of every particle trajectory, the plasma is characterized by a distribution function $f_{(\mathbf{x},\mathbf{v},t)}$ characterizing groups of particles of the same velocity (**v**) at a given location (**x**) and time (t). By calculating the rate of change in a small area in phase-space and by including particle collisions (characterized by constrained sources and sinks in phase-space) we obtain the Boltzmann equation.

$$\text{Boltzmann equation:} \quad \frac{\partial f_\sigma}{\partial t} + \frac{\partial}{\partial \underline{x}}(\underline{v} \cdot f_\sigma) + \frac{\partial}{\partial \underline{v}}(\underline{a} \cdot f_\sigma) = \sum_\alpha C_{\alpha\sigma}(f_\sigma) \tag{1-8}$$

where $C_{\alpha\sigma}(f_\sigma)$ is the collision operator measuring the rate of change of the distribution function f_σ due to collisions of species σ and α, and the particle acceleration given by the Lorentz force is $\underline{a} = (q/m) \cdot (\underline{E} + \underline{v} \times \underline{B})$. The collisionless form of the equation, when the collision term (the right side of the equation) is set to zero, is called the Vlasov equation.

Fluid theories, such as the two-fluid theory and the single-fluid magneto-hydrodynamic (MHD) theory, involve alternative averages of the Vlasov equation. In the **two-fluid theory** average of the velocity is taken over all particles of a given species (with mass m_σ and charge q_σ) at a given location and the plasma is characterized by the species density ($n_{\sigma(\mathbf{x},t)}$), mean velocity ($\mathbf{u}_{\sigma(\mathbf{x},t)}$) and pressure ($\mathbf{P}_{\sigma(\mathbf{x},t)}$) defined relative to the species mean velocity.

$$\text{Species density:} \quad n_\sigma(\underline{x},t) = \int f_\sigma(\underline{x},\underline{v},t)d\underline{v} \tag{1-9}$$

$$\text{Mean velocity:} \quad \underline{u}_\sigma(\underline{x},t) = \frac{\int \underline{v} \cdot f_\sigma(\underline{x},\underline{v},t)dv}{n_\sigma(\underline{x},t)} \tag{1-10}$$

$$\text{Pressure tensor:} \quad P_\sigma(\underline{x},t) = m_\sigma \int (\underline{v} - \underline{u}_\sigma(\underline{x},t)) \cdot (\underline{v} - \underline{u}_\sigma(\underline{x},t)) \cdot f_\sigma(\underline{x},\underline{v},t)d\underline{v} \tag{1-11}$$

In the simpler one-fluid **MHD picture** the momentum is averaged over all particles of all species. The plasma is then characterized by the total mass density ($\rho_{(x,t)}$), center of mass velocity ($\mathbf{U}_{(x,t)}$) and pressure ($\mathbf{P}_{(x,t)}$) defined relative to the center of mass velocity.

Total mass density:
$$\rho = \sum_\sigma m_\sigma \cdot n_\sigma \qquad (1\text{-}12)$$

Center of mass velocity:
$$\underline{U} = \frac{1}{\rho} \sum_\sigma m_\sigma \cdot n_\sigma \cdot \underline{u}_\sigma \qquad (1\text{-}13)$$

MHD pressure:
$$\underline{P}_{MHD} = \sum_\sigma \int m_\sigma \cdot (\underline{v} - \underline{U}) \cdot (\underline{v} - \underline{U}) \cdot f_\sigma d\underline{v} \qquad (1\text{-}14)$$

The MHD theory relies on the following necessary assumptions: a) charge-neutrality of the plasma, b) the phenomenon under study is slow compared to the speed of light and finally c) the time scale of the phenomenon is long compared the electron and ion cyclotron times. The theory provides self-consistent description of phenomena satisfying the above assumptions based on five basic equations as follows.

1) The MHD continuity equation can be derived by taking the zeroth moment of the Vlasov equation, integrating it over the velocity and summing over the present particle species.

MHD continuity equation:
$$\frac{\partial \rho}{\partial t} + \nabla \cdot (\rho \cdot \underline{U}) = 0 \qquad (1\text{-}15)$$

2) The MHD equation of motion is obtained by taking the first moment of the Vlasov equation, multiplied by the species mass (m_σ) and summing over the different species with thermal velocity distribution.

Current density:
$$\underline{J} = \sum_\sigma n_\sigma \cdot q_\sigma \cdot \underline{u}_\sigma \qquad (1\text{-}16)$$

MHD equation of motion:
$$\rho \left(\frac{\partial}{\partial t} + \underline{U} \cdot \nabla \right) \cdot \underline{U} = \underline{J} \times \underline{B} - \nabla \cdot \underline{P}_{MHD} \qquad (1\text{-}17)$$

where the bracket defines a convective derivative.

3-4) In case of the Maxwell equations, assuming low frequencies and the charge neutrality lead to the simplification of the four equations to two.

8

Faraday's law: $\qquad \nabla \times \underline{E} = -\dfrac{\partial \underline{B}}{\partial t}$ (1-18)

Ampere's law: $\qquad \nabla \times \underline{B} = \mu_0 \cdot \underline{J}$ (1-19)

where μ_0 is the magnetic constant (called permeability of free space as well).

5) Finally Ohm's law takes the following form:

Ohm's law: $\qquad \underline{E} + \underline{U} \times \underline{B} = \eta \cdot \underline{J}$ $\qquad$ where η is the plasma resistivity. (1-20)

The MHD theory is often used to calculate the plasma force equilibrium and a large part of plasma waves and instabilities.

1.4 Magnetic fusion devices

In a magnetic fusion device, plasma is confined by magnetic field as charged particles traverse along the magnetic field lines on Larmor trajectories. To avoid particle losses at the ends a straight cylinder is bent creating closed field lines (toroidal vessel). Due to the curvature and gradient of the magnetic field in toroidal geometry, slow drift motions of the charged particles arise primary in the vertical direction. To compensate this drift, the magnetic field lines are wound helically inside the torus as indicated in figure 1-2a, as this way the fast charged particle motion along the field lines can compensate for the drifts. The way the restricting magnetic field geometry is created defines two major construction lines, the **tokamaks** and the **stellarators**. Figure 1-2 illustrates these two concepts including the standard geometry notations used in these devices, i.e. the toroidal (long way around the torus), poloidal (short way around the torus) and radial coordinates. As the toroidal magnetic field of a tokamak is proportional to $B_t \sim 1/R$ where R is the major radius, the inboard side is often called high field side (**HFS**) and the outboard side low field side (**LFS**) of the device.

The difference between the stellarators and tokamaks in the way the helical magnetic field is generated necessary for stable equilibrium. In a tokamak, presently the leading concept for a fusion reactor, the plasma is used as a secondary winding with a central transformer and the inductively generated toroidal plasma current supplies the poloidal component. The helical field is a combination of the toroidal field supplied by the toroidal coils and this poloidal field component. In contrast, in stellarators all confining magnetic field components are produced by a complex, 3D external coil system with negligible plasma

current flowing through the plasma. The produced helical magnetic field lines define so called **flux surfaces**, i.e. span nested toroidal surfaces of constant poloidal magnetic flux. Due to the small Larmor radius (typically <mm) particles travel significantly faster along the magnetic field line compared to the perpendicular direction, thus the plasma quantities equal out on the flux surfaces on a very short time scale. Therefore the radial evolution of plasma quantities, called **profile** given in flux coordinates can describe the whole plasma equilibrium.
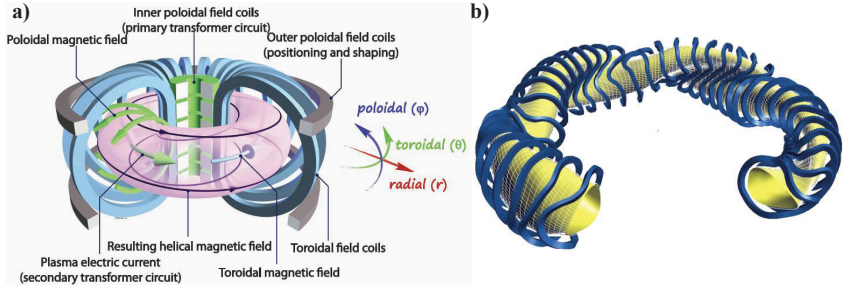
Figure 1-2 The magnetic coil configuration of a tokamak (source: EFDA-JET) and stellarator device with a possible plasma geometry. In case of the stellarator, only 4/5 of the coil structure and plasma is shown, to illustrate the different toroidal plasma cross-sections of stellarators in contrast to the axisymmetrical structure of the tokamak. The standard geometry notations, the toroidal, poloidal and radial directions are indicated as well,

Plasma refuelling is done mainly by periodic injection of cryogenic **pellets** (ice cubes) of Hydrogen isotopes and the less effective gas puffing. Conventional plasma heating methods include neutral particle beams and resonant electromagnetic waves to complement **Ohmic** heating in tokamaks (resulting from the resistance to the plasma current caused by electron-ion collisions), as this becomes ineffective at high temperatures (the resistivity decreases with the electron temperature $\eta \sim T_e^{-3/2}$). **N**eutral **B**eam **I**njection, alias **NBI** is based on the concept of high energy neutral particles – unaffected by the magnetic field – injected into the plasma, where after ionisation they get confined in the plasma and the energy is gradually transferred to the plasma electrons and ions through Coulomb collisions. In case of radiofrequency heating the energy is transferred from the external source to the plasma by electromagnetic waves as the plasma absorbs the energy of the incident wave at given resonant frequencies. Based on the species and frequency there is **E**lectron **C**yclotron **R**esonance **H**eating (**ECRH**) and **I**on **C**yclotron **R**esonance **H**eating (**ICRH**). In an operating

reactor the generated α-particles will maintain the required plasma temperature (**α-particle heating**) during plasma operation (at start-up the conventional systems need to be used). The α-particles carrying 20% of the energy from the fusion reaction remain confined in the plasma due to their positive charge and lose their energy to other particles in the plasma. At ignition the **fusion gain (Q)** – the ratio of the fusion power to the input power – approaches infinity. The two main construction lines, the tokamaks and stellarators aim to optimize fusion gain at a high value where some additional heating method is still used to control the plasma in a possibly steady-state operation.

In early experiments plasmas were polluted with impurities due to strong plasma-wall interaction. To minimise this interaction **limiter**s were placed on the vacuum vessel to define a **L**ast **C**losed magnetic **F**lux-**S**urface (**LCFS**) of the then circular cross-section of the plasma. The idea is that outside this, in the so-called **S**crape **O**f **L**ayer (**SOL**) region magnetic field lines terminate on the limiters, thus the carried heat and impurity generation are localised to a small area. Nowadays larger devices favour to use additional magnetic coils to create so-called X-point(s), where the poloidal magnetic field is zero. In this case the last closed flux surface is called separatrix. In such a configuration outside the separatrix the magnetic field lines are diverted into a region of the vessel, called the **divertor**, where they cross solid material surfaces, the divertor plates. A relatively closed divertor region optimizes pumping and reduces impurity backflow to the plasma. These concepts are illustrated below in a typical poloidal cross-section of a tokamak device and plasma in figure 1-3.
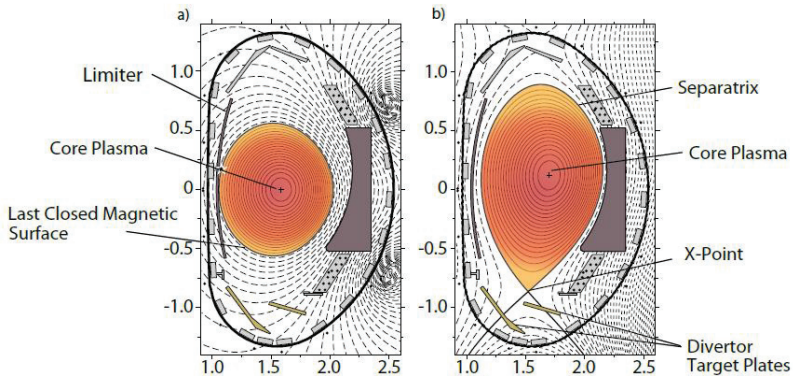

Figure 1-3 Poloidal cross-section of a tokamak plasma (figure based on [5])

11

Plasma behaviour and stability is especially sensitive to the magnetic structure. To describe this structure locally the **safety factor** (q) is commonly used. It denotes the number of times the given helical field line goes around the torus toroidally for a single poloidal turns. In tokamaks typical q values are of unity in the plasma center increasing to 2-8 towards the plasma edge. In divertor tokamak experiments q95, the safety factor at 95% of the poloidal flux is commonly used as the edge q value as at the separatrix q becomes infinite. Below q=1 the plasma is locally unstable, whereas for q_{edge} <2, it is globally unstable. In a tokamak the q-profile strongly depends on the plasma current profile, with higher values indicate higher ratio of toroidal magnetic field (B_t) to the poloidal field (B_p) generated by the plasma current, thus is less prone to potentially hazardous current-driven instabilities. If R>>a (major plasma radius>>minor plasma radius) the safety factor can be obtained from the poloidal and toroidal field as:

Safety factor: $\quad q = \dfrac{r \cdot B_t}{R \cdot B_p}$, $\quad$ where r is the plasma radius $\hspace{2cm}$ (1-21)

In the optimized, almost current-free stellarators the inverse of the safety factor that is the so-called **rotational transform / iota** (ι) is used and some, like the W7-AS advanced stellarator, can be characterized by flat iota profiles.

1.5 Plasma instabilities

Instabilities play a complex dual role in fusion physics. On one side they seriously deteriorate plasma performance by either leading to the loss of plasma control (large-scale instabilities) or significantly enhanced radial transport of particles and energy (small scale instabilities), whereas at other instances can provide the much needed cross-field impurity transport cleaning the plasma to prevent accumulation and radiation collapse. Instabilities are driven by various inhomogeneities in the plasma: current, pressure, density and temperature. In addition there are instabilities that are driven by the non-maxwellian velocity distribution, especially by a population of suprathermal (fast) particles.

In the MHD picture, the free energy contained in the equilibrium configuration comes from either the kinetic energy of the plasma or the energy of the magnetic field generated by the plasma. That is instabilities are driven either by the current gradients or the pressure gradient combined with adverse magnetic field curvature, the possible source terms in the MHD equation of motion. The resulting instabilities are then further classified as ideal or resistive modes. Ideal instabilities occur even if the plasma were perfectly conducting, whereas resistive types depend on the finite resistivity of the plasma. In the ideal case the

magnetic flux is conserved, the topology remains the same, whereas in the resistive case the magnetic topology changes, field lines are torn and reconnected. Magnetic islands form in case of tearing modes and are a nonlinear solution of the MHD equations. Stabilizing effect of MHD modes may arise from the bending, compression and good curvature (centre of curvature is opposite to the pressure gradient) of the magnetic field lines.

Instabilities can have an infinite spectrum of possible modes, based on their form $exp[i \cdot (m \cdot \theta - n \cdot \phi)]$ each characterized by m poloidal and n toroidal mode numbers. Modes of different poloidal mode numbers may also couple at a given radial location and create compound mode number spectra. The stabilizing effect of line bending is at minimum at magnetic surfaces where q matches the mode number of the instability ($m/n=q$) thus resonance occurs at these rational surfaces[4]. The stabilization is stronger for high-m modes so these modes occur only strongly localized around the resonant surface while low mode number modes are not localized (although their corresponding resonant surface must lie inside the plasma or close to its surface).

Two types of edge relevant MHD instabilities and their combinations are of special interest regarding impurity control. **Ballooning modes** are high-n mode number pressure gradient driven instabilities strongly localized on the outboard side of the torus around their respective resonant surface (m/n). In case of the localized modes the appropriate average curvature of the magnetic field balances the effect of the pressure gradient, i.e. stabilizes in the inner side ('good curvature region') and destabilizes on the outer side of the tokamak ('bad curvature region'). The **kink/peeling modes** are a low-n mode number branch of current-driven instabilities in the ideal/resistive picture respectively located at the plasma edge. Instabilities can be stabilized (i.e. suppressed) or destabilized (i.e. triggered) by external means such as waves and particles.

1.6 Confinement regimes and impurity control in fusion devices

Confinement and the related transport of energy and particles are in the frontline of fusion plasma physics research. In the absence of instabilities, the cross-field transport (i.e. perpendicular to the main, toroidal magnetic field) results from binary particle collisions only. This so-called **classical** (cylindrical geometry) or **neo-classical transport** (toroidal geometry, including drift orbit effects) can be derived analytically or numerically. The calculated transport coefficients however lie orders of magnitude lower than found in experiments. The observed **anomalous transport** is believed to be driven by plasma micro-turbulence. The

---

[4] Rational surfaces are magnetic flux surfaces with rational safety factors, i.e. q=m/n where m and n are integers.

topic of anomalous transport is inherently complex with highly non-linear turbulent processes interacting through many drives and suppressors on multiple scales. Through the last couple of years remarkable progress has been made in the field of transport theory and simulation codes with many types of instabilities described eloquently summarized in [7]. Although recent numerical simulations give reasonable estimates to transport levels, still many fundamental phenomena are an open question and the physical understanding and prediction of turbulence-driven (anomalous) transport remains one of the key issues of modern fusion-oriented plasma physics.

It is generally accepted that nonlinear interaction of unstable waves can generate sheared flows in the plasma. These reduce transport by taking out energy from turbulence or by shearing turbulent eddies. This is a highly nonlinear self-organisation of turbulence and flows, and is believed to be the main reason for the complexity of transport phenomena. In several cases transitions occur in the system. The most important example is the low (standard) confinement mode alias **L-mode** and the high (improved) confinement mode commonly referred to as **H-mode**. In H-mode the energy confinement time nearly doubles compared to conventional L-mode scenarios due to the development of a transport barrier (pedestal) in the plasma edge. A strong sheared flow observed in the edge region is believed to be a key ingredient of the L-H transition, but a predictive theory is not yet available. The L-H transition is observed both in tokamaks and stellarators alike. In contrast to the many differences between the two devices, the transport processes and turbulence appears to be very similar.

The high particle confinement of the H-mode regime is a two-edged advantage. On one side it is the very desirable feature making the construction of fusion reactor realisable at our present technological and financial state, on the other hand the confined particles include **impurities** of higher atomic numbers leading to much higher radiation levels (radiation scales with square of the atomic number) that can effectively shut down the plasma through the severe radiation losses. In a future fusion reactor, fuel dilution by Helium produced in the fusion reaction would also be a problem. Impurity control is thus the major decisive issue of any confinement regime.

The most common H-mode scenario involves **E**dge **L**ocalised **M**odes, in short **ELM**s that are MHD instabilities driven by the steep pressure and/or current gradient in the pedestal area. They are empirically categorized into several classes. Type I (large ELMs) occur usually in the best performance plasmas, whereas types II and III are observed usually at lower performance. These transient instabilities help relieve the impurity concentration in the

machine by periodically expulsing an amount of material. On the other hand type-I ELMs also pose a major thread to fusion devices as they – without proper control – can damage the first-wall components thereby possibly reducing the lifetime of the ITER divertor to merely a couple of discharges. Mitigation of ELMs is essential and the major ELM control techniques relying on external actuators are mini-pellet injections and edge magnetic field ergodization. With proper mitigation technique to reduce ELM sizes, the Type I ELMy H-mode is selected as a reference scenario for the future ITER fusion reactor.

The other direction of H-mode studies focus on ELM-free regimes where the steady-state operation is assured by other instabilities relieving the plasma of the dreaded impurities through continuous edge MHD activity. The two main instabilities are the **Quasi-Coherent (QC) modes** and the **Edge Harmonic Oscillations (EHO)** that are believed to have an effect on particle transport. The corresponding ELM-free H-modes in tokamaks are referred to as the **Enhanced D-alpha (EDA)** mode and the **Quiescent H-mode (QHM)** respectively. The underlying mechanism of these instabilities is still poorly understood and is lacking in satisfactory theory. In stellarators the stable ELM-free H-mode is called **High Density H-mode (HDH)** and the related impurity transport mechanism has not been found yet.

The two major topics of the thesis thus deal with controlling the impurity concentration in H-mode plasmas by investigating a) an ELM mitigation and fuelling technique, the pellet injections mainly at the ASDEX Upgrade tokamak and b) plasma instabilities in the High Density H-mode of the W7-AS stellarator and their relation to impurity transport to locate the mechanism responsible for the low impurity concentration of this regime.

1.7 The road toward fusion reactors

September 1-13, 1958 marked the Second United Nations International Conference on the Peaceful Uses of Atomic Energy, or better known as the second "Atoms for Peace" conference held on the shores of Lake Geneva. The declassification of fusion research was the first step toward the very broad international collaboration that led us – 50 years later – to a variety of fusion devices shown in figure 1-4.

Tokamak research began at the Kurchatov Institute in Russia, the word Токамак itself a Russian abbreviation for "**to**roidalnaya **ka**mera and **ma**gnitnaya **k**atushka", that is for "toroidal chamber with magnetic coils". In 1968 at the 3rd IAEA Conference on Plasma Physics soviet scientists announced that they have achieved electron temperature over 1 keV in a tokamak type of device, a stunning value far superior to any other group's achievements. After an independent measurement confirmed the results, many national programs quickly

switched to the tokamak design and it remained the leading concept reflected in the design of the first experimental fusion reactor, ITER as well.

Figure 1-4 *40 years achievements of fusion history – the triple product versus the central ion temperature*

The major advantage of this design is its simplicity given its axisymmetric geometry. There are, however, also two major draw-backs to tokamaks coupled to the current in the plasma itself that produces the poloidal magnetic field component required for confinement. First the transformer-like electrical setup of the tokamak limits the duration of the discharge, as it cannot provide continuous current in the plasma, the secondary winding. Thus it can only operate in pulsed intervals instead of steady-state. Secondly severe plasma current driven instabilities can lead to the loss of plasma control such as disruptions where the plasma current collapses in an uncontrolled way. Special attention is paid to avoid or mitigate these instabilities deteriorating the plasma performance.

Stellarator (stella meaning star in Latin) is one of the oldest toroidal fusion concepts, the idea originating from Lyman Spitzer in Princeton (~1950). The complex 3D geometry of the magnetic coil systems makes it a major technological challenge for construction, thus its step back compared to tokamaks. Its almost current-free setup however enables continuous

operation and good confinement qualities due to the lack of current-driven instabilities. These excellent qualities have stellarators there for a possible come-back.

This work focuses mainly on results obtained at two devices: the ASDEX Upgrade (AUG) tokamak and Wendelstein 7-AS (W7-AS) stellarator and compares the stellarator results to that of the Alcator C-Mod tokamak.

- **ASDEX Upgrade** [8] is a midsize tokamak experiment that has been in operation at the Max-Planck-Institut für Plasmaphysik (IPP) in Garching, Germany since 1990. Its name as in **A**xial **S**ymmetrix **D**ivertor **Ex**periment Upgrade, indicates that it is a successor of the first tokamak experiment (ASDEX) with a poloidal divertor. Besides edge and divertor physics, its focus lies in testing alternative first-wall elements (AUG is the only full-tungsten device compared to most common carbon first-wall devices) and the study of avoiding, stabilizing and mitigating different plasma instabilities.

- **Wendelstein 7-AS** (1988-2002) [9] was the first of the advanced stellarators, where the magnetic field has been optimized numerically. It was a modular, low magnetic shear stellarator with a five-fold symmetry. Its optimized island divertor concept, where the plasma is bounded by a separatrix formed by naturally occurring magnetic islands enabled W7-AS to reach high confinement out of reach of other stellarators. Furthermore an ohmic transformer provided possibility for additional configuration control via toroidal plasma current that enabled the studies related to the effect of the magnetic shear on confinement and MHD stability.

- The **Alcator C-Mod** tokamak [10] is the last in the Alcator series at the Massachusetts Institute of Technology (MIT), USA, a unique tokamak line famous for its very high toroidal magnetic fields (up to 12T). The high plasma current proportional to the magnetic field (to B_t/R at constant q, where R is the major radius of the device) enables the achievement of very high densities (up to 10^{21} m^{-3}) providing data in relevant parameter regimes unreachable for other tokamaks.

A comparison of these devices regarding the main technical and plasma parameters is given in table 1-2.

Essential fusion power plant technologies will be deployed for the very first time in the ITER device, the international thermonuclear fusion reactor experiment ('iter' is also the Latin word for 'the way'). ITER is intended as a single experimental link between present tokamak devices and an industrial prototype of fusion reactor. First plasma is expected for 2019, whereas full-power Deuterium-Tritium operation is planned for 2027. To demonstrate the reactor relevance of the stellarator concept, the **Wendelstein 7-X (W7-X)** device is built

in IPP Greifswald, Germany. Starting 2014, its design and superconducting coils will allow for long to quasi-steady state operation under stable, current-free conditions close to that of a power plant.

DEMO, as the demonstration power plant is generally referred to, will be the first fusion reactor experiment to generate electricity. The neutrons, that carry 80% of the fusion energy, escape the confining magnetic field being neutral. Reaching the wall, they are slowed down, and the generated thermal energy is transformed into electricity in the standard way as in a conventional power plant. That is the coolant circulated through the walls is passed through a heat exchanger to produce steam in order to drive turbines. Based on the ITER and W7-X results, the construction of DEMO can perhaps start around 2035 with first plasma about 10 years later. Commercial power plants could be then available around in the second half of this century, roughly about a century after the famous Geneva Conference and the declassification of fusion research.

Devices	ASDEX Upgrade	Alcator C-Mod	Wendelstein 7-AS
R [m]	1.65	0.67	2
a [m]	0.5	0.21	< 0.18
t_{pulse} [s]	< 10	< 2	< 1
B_t [T]	3.1	8	2.6
n_e [m^{-3}]	10^{20}	10^{21}	10^{20}
P_{NBI} [MW]	20	0	3
P_{ECRH} [MW]	2x2	0	2.6
P_{ICRH} [MW]	6	5	2

Table 1-2 *Technical data and typical plasma parameters of major plasma devices*
[R - major radius, a - minor radius, t_{pulse} – typical pulse length, B_t - toroidal magnetic field, n_e - electron density, external heating systems: P_{NBI} - NBI, P_{ECRH} – ECRH, P_{ICRH} - ICRH heating power]

1.8 Thesis motivation

I.) Plasma fuelling and ELM mitigation by pellet injection: The injection of cryogenic hydrogen isotope pellets into fusion plasmas is considered to be a promising way to achieve plasma fuelling in modern tokamaks and is a standard tool for ELM mitigation as well. In early experiments pellets were injected from the magnetic low field side, as technically the outboard side of the tokamak was easier accessible. This however led to rapid mass losses of the pellets, as a drift due to the magnetic field gradient drifts the deposited material always in the positive major radius direction, i.e. outward of the plasma [11]. After this discovery a major change in the setup of fuelling systems took place. Although technically more complicated, the fuelling systems were adapted to the high field side (inner) of the tokamak to take advantage of the drift effects. In this case the ablatant particles are accelerated toward the center of the plasma, thereby achieving a significantly higher plasma fuelling efficiency. Thus HFS pellet injection is presently chosen to be the key fuelling scenario of ITER.

It has been observed that pellets trigger ELMs and thus by injection of small pellets the ELM frequency and size can be controlled thereby reducing the power load onto the divertor plates [12]. Experiments conducted at ASDEX Upgrade suggest that a pellet of a fraction of the fuelling pellet size passing at a given location is sufficient to destabilize the pedestal locally and trigger an ELM [13]. Although this technique has still to be investigated in a larger parameter range for proper extrapolation, code simulations indicated that shallow small pellets have the potential for ELM pacing in reactor size experiments and thus has been selected as one of the mitigation techniques in ITER.

In the case of both fuelling (large pellets at low repetition rate) and ELM mitigation (small pellets at high repetition rate) the **penetration depth** of the pellet is a key factor. As mentioned before in fuelling deep pellet penetration into the hot target plasma beyond the pedestal is required to improve the efficiency of particle fuelling. On the other hand, penetration at least half way to the top of the pedestal is required for ELM pacing by pellets. Furthermore, deeper penetration also improves the achievable plasma operation parameters by causing longer particle confinement time.

Multi-machine pellet data concerning LFS injections were collected worldwide into the International Pellet Ablation Database in 1997 and an LFS penetration depth scaling was given with respect to four ablation relevant parameters as suggested by theory [14]. For the HFS pellet injections however, a systematic statistical analysis and the establishment of an empirical scaling law was limited until now by the scarce availability of an extensive and validated pellet dataset. To support the design of the ITER pellet injection system, there is

thus an inevitable need for thorough analysis based on a qualified HFS pellet injection dataset and the establishment of empirical scaling laws such as an HFS pellet penetration depth scaling on the ablation relevant pellet and plasma parameters.

The first part of the thesis describes the development of a HFS pellet ablation database based on ASDEX Upgrade and Tore Supra. A HFS penetration depth scaling is derived on the ASDEX Upgrade dataset by statistical analysis. Also a comparison is made with the existing empirical LFS penetration depth scaling and to theoretical models. The magnetic field dependence of pellet ablation is further investigated by dedicated pellet experiments conducted at the ASDEX Upgrade tokamak.

Results II.) Edge instabilities in the High Density H-mode regime In recent years increasing interest has been devoted to stable ELM-free H-modes with similar plasma performance to ELMy H-modes where the increased particle transport at the edge is driven by a different continuous edge fluctuation. In case of stellarators this type of H-mode has been found only at W7-AS inadvertently, where the High Density H-mode [15] aiming at high densities along high confinement and has been proven to be a liable, promising alternative to operating in Type-I ELMy H-mode. It has been found that impurities are both screened and flushed out of the plasma, whereas the confinement of the fuel, i.e. Hydrogen isotope particles increases. The fusion power increases with square of the density, thus the combination of very high densities and quasi-steady state stable conditions makes this H-mode a very promising candidate for a future fusion reactor. Despite extensive experimentation this mechanism responsible for the low impurity confinement in the HDH-mode however could not be identified. The HDH mode has also been attempted at the Large Helical Device (**LHD**), the other large-scale advanced stellarator experiment at the National Institute for Fusion Science (NIFS) in Japan. The failure to reproduce the HDH mode in LHD points to the missing element in the understanding of this H-mode. Due to its many advantages and potential to be a reactor operational regime the HDH mode has been also selected as a desired operational scenario of the future W7-X stellarator.

The extrapolation of the HDH mode to different operational ranges such as that of W7-X is not yet resolved, thus better understanding of this regime is essential. The central question is the mechanism responsible for the low impurity confinement that only involves particles of higher atomic numbers. The second part of this thesis thus focuses on the investigation of edge instabilities in fluctuation measurements of HDH plasmas regarding their relation to impurity transport, as the mechanism is thought to reside in the plasma edge.

Chapter 2

Experimental Findings and Related Theories

This chapter describes the different H-modes and their corresponding instabilities controlling the impurity concentration with special interest on the HDH mode of the W7-AS device. The chapter finishes with an overview on the core of a common ELM mitigation technique, pellets and the related theoretical ablation theories.

2.1 H-mode

H-mode had been discovered on 4th February 1982 at the 'old' ASDEX tokamak (Garching, Germany, presently known as HL-2A, China) [16] showing improved particle confinement and a substantial increase of the energy content at constant heating power. These clear advantages, making the construction of a fusion reactor presently realisable, made its importance known from the very start. In 1992 H-mode had been observed for the very first time in a non-tokamak type device, at the W7-AS stellarator [17]. Since then several other helical devices achieved H-mode as well and the common characteristic features in the different devices make H-mode a generic regime of toroidal confinement.

Common feature of H-mode is the sudden disappearance of edge turbulence whereas at the same time its driving forces, the edge gradients, increase. Close correlation had been observed in the dynamics of turbulence and flows [18] thus supporting the belief that sheared poloidal flows residing in the plasma edge can be responsible for the diminution of turbulent transport, reducing the micro-turbulence otherwise limiting confinement. The improved particle and energy confinement is caused by the development of an edge transport barrier (reduced transport region) just inside the separatrix. Figure 2-1 illustrates typical electron density and temperature profiles corresponding to L-mode (blue squares) and H-mode (red

circles) respectively indicating the radial region of steep gradients called pedestal area in the latter case due to the transport barrier. The L-H transition requires some level of heating power with this threshold power depending on the plasma density. The L-H mode transition is however not yet fully understood and is an area of active fusion research.
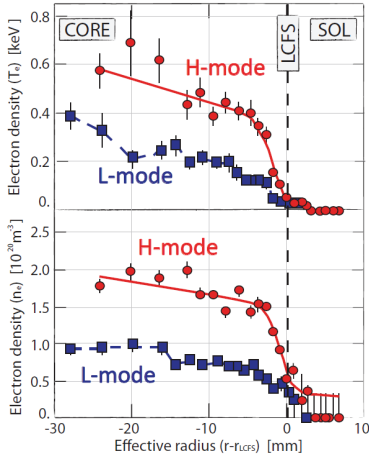

Figure 2-1 Electron density and temperature profiles for L- and H-mode plasmas respectively. The main plasma regions, the core plasma, the scrape-of-layer (SOL), and the last closed fluxed surface (LCFS) are indicated.

In a reactor H-mode high fusion gain (goes with the square of the electron density), steady-state (that is stability, non-inductive current drive, α-particle heating) and impurity control is essential. The following key concepts have to be generally taken into account in a tokamak design:

a) *high fusion triple product:* requires the scenario to obtain high pressure (n·T) and energy confinement time (τ_E) values. By increasing the density above the empirically found **Greenwald density limit** (n_{GW}) [19], the plasma tends to end in a disruption. The Greenwald fraction, the density normalized to the Greenwald limit, is often quoted instead of the density.

Greenwald fraction: $f_{GW}=n/n_{GW}$ where $n_{GW}=I_p/(\pi \cdot a^2)$ (2-1)

where I_p is the plasma current and a is the minor plasma radius.

The energy confinement time is also often normalized to the generally accepted H98(y,2) H-mode energy confinement time scaling [20] and referred to as **H** or **H98(y,2) factor**.

H-factor: $\quad\quad\quad\quad\quad H98(y,2)=\tau_E/\tau_E^{H98(y,2)}$ $\quad\quad\quad$ (2-2)

where W is the global plasma energy and P is the applied heating power.

H98(y,2) confinement time scaling:

$$\tau_E^{H98(y,2)} \sim I_p^{0.93} \cdot B_t^{0.15} \cdot P^{-0.69} \cdot n_e^{0.41} \cdot M^{0.19} \cdot R^{1.97} \cdot \varepsilon^{0.58} \cdot \kappa^{0.78} \quad\quad (2\text{-}3)$$

where M is the averaged mass number, R the major plasma radius, ε the aspect ratio ($\varepsilon=R/a$) and κ is the elongation defined here as $\kappa=S/(\pi \cdot a^2)$ with S being the plasma cross-sectional area.

b) *steady-state operation:* the desired steady-state operation cannot be reached by the traditional inductive current drive as it is inherently pulsed. To obtain long pulse length the toroidal current producing the poloidal component of the confining magnetic field should be generated non-inductively by the additional heating systems (NBI, ICRH, ECRH) and/or by taking advantage of a self-generated plasma current called bootstrap current. The **bootstrap current** is a neoclassical effect associated with trapped particle orbits in the presence of a plasma pressure gradient. For high fraction of non-inductive current drive low collisionality and high β values are important. Collisionality is the frequency of particle collisions that can be calculated (in the pedestal area) according to the neoclassical formula as

Collisonality: $\quad\quad \nu^*=R \cdot q_{95} \cdot \varepsilon^{-3/2} \cdot \lambda_{ee}^{-1}$ where $\lambda_{ee}=1.727 \cdot 10^{17} \cdot T^2/n/\ln\Lambda$ $\quad$ (2-4)

where λ_{ee} is the electron-electron coulomb collision mean free path with $\ln\Lambda$ being the Coulomb logarithm.

Due to its high temperature plasma, ITER will operate at very low collisionality, a regime with optimal current drive efficiencies.

Finally β is the plasma pressure normalized to the magnetic pressure with its value commonly normalised to the Troyon scaling [21].

β: $\quad\quad\quad\quad\quad \beta=2 \cdot \mu_0 \cdot n \cdot e \cdot (T_e+T_i)/B^2$ $\quad\quad\quad$ (2-5)

where μ_0 is the magnetic permeability and e the electric charge.

Normalised β: $\beta_N = \beta / \beta^{Troyon}$ where $\beta^{Troyon} = I_p / (a \cdot B_t)$ (2-6)

High β operation below the β limit (destabilizing major MHD events) is important to reach high pressure values (high plasma performance) and thus also obtain high bootstrap current for the non-inductive current drive.

c) *detachment*: in the divertor area the plasma can be attached or detached from the divertor plates. Detachment means that a layer of plasma in front of the divertor undergoes a thermal instability which increases its visible line radiation power and decreases its temperature. This layer radiates off most of the incoming power, thereby distributing it over a much larger area. Reactor relevant plasmas have to be at least partially detached to reduce heat loads on the divertor plates to acceptable levels.

Stellarators with their 3D magnetic coil geometry producing the confining magnetic field have two major advantages over tokamaks. No inductive current or current drive is required as they are inherently steady-state. As they do not have a strong plasma current, they are also not prone to current driven disruptive instabilities. As this sets the Greenwald limit in tokamaks, stellarators are also capable of very high density operation provided particle transport can be controlled. Stellarators on the other hand are substantially more complicated to build which results in a huge increase in cost. Furthermore without sufficient optimization they have poor confinement compared to tokamaks. An energy confinement scaling exists for stellarators as well in the following form of the international stellarator scaling ISS95 [22]:

Confinement time: $\tau_E^{ISS95} \sim a^{2.21} \cdot R^{0.65} \cdot P^{-0.59} \cdot n_e^{0.51} \cdot B_t^{0.83} \cdot \iota_{2/3}^{0.4}$ (2-7)

where $\iota_{2/3}$ is the rotational transform at the 2/3 of the plasma radius.

In both magnetic configuration instabilities play a key role both as defining the accessible parameter regime for stable operation as well as in case of specific edge instabilities for lowering the impurity concentration. In fact H-mode regimes are commonly categorized by their way of tackling or perhaps not handling the impurity problem that is after their key edge instability or lack of it (e.g. ELMy H-modes or ELM-free H-modes). Some regime names are slurred between the different fusion experiments. For example

Quiescent H-mode can mean a stable regime with a specific governing instability in one case, and an unstable regime with impurity accumulation in the other. The diversity in the names of the different or similar H-mode regimes clearly indicates the lack of understanding in confinement physics. For better separation and comparison, a summary of the main features of the different H-modes relevant for this thesis is given in table 2-1.

Table 2-1: *Characteristics of different H-mode regimes: collisionality regime, impurity accumulation and presiding MHD activity controlling the impurity concentration.*

Regime	Device	Collisionality	Impurity accumulation	Instability
ELMy	AUG	low/high	No	ELMs
	W7-AS	low/high	No	ELMs
QHM	DIII-D	low	No	EHOs
	AUG	low	yes/no	none/EHOs
EDA	Alcator C-Mod	high	No	QC
H*	W7-AS		Yes	None
HDH	W7-AS	High	No	Not yet identified

2.1.1 H-mode with edge localized modes

ELMy H-mode is the most common H-mode present in all devices capable of reaching H-mode. ELMs are transient instabilities defining the dynamics of the plasma edge. They repulse particles out of the plasma, thereby reducing the edge pressure and providing sufficient cleansing of the plasma of impurities. ELMs however strongly reduce the tokamak performance as confinement properties among them energy, particle, impurity and momentum is affected by these strong events. If uncontrolled they also pose a severe danger to first wall elements by significant power loads on the solid surfaces thereby limiting the machines lifetime to even possibly a few days. Deeply coupled to most H-mode regimes, they were also first observed on the 'old' ASDEX tokamak [23].

ELMs are believed to be the result of destabilization of ideal MHD waves in the pedestal region driven by large edge pressure and current gradients. Although not yet fully understood, significant progress has been achieved in the peeling-ballooning model of ELMs [24-26] leading to the reliable understanding of the ELM onset and dynamics in the moderate to high collisionality pedestal regime. Typical H-mode pressure and current profile is shown in figure 2-2. The pedestal region is characterized by steep pressure gradient and corresponding large bootstrap current. The model states that the free energy in the large pressure gradient and current drives peeling, ballooning or coupled peeling-ballooning

modes that constrain the maximum pressure at the pedestal top triggering ELMs at this pressure value. Experiments generally agree with this model, the pressure gradients are at the value where the MHD modes became unstable. The edge current distribution is however very difficult to measure. Some measurements [27] indicate a change in the edge current density during the ELM cycle supporting the model. The ELM crash starts on the outer side of the torus with the density perturbation propagating toward the inner side with the ion sound velocity, consistent with the ballooning type theoretical interpretation. High time resolution temperature and density profile measurements [28] during the type-I ELM cycle however also show a saturation of the pedestal top pressure before the release of the new ELM, thus indicating that we do not yet have complete understanding of this phenomenon. Most notably there is no theory to predict the amount of energy (ELM size) released during an ELM event.
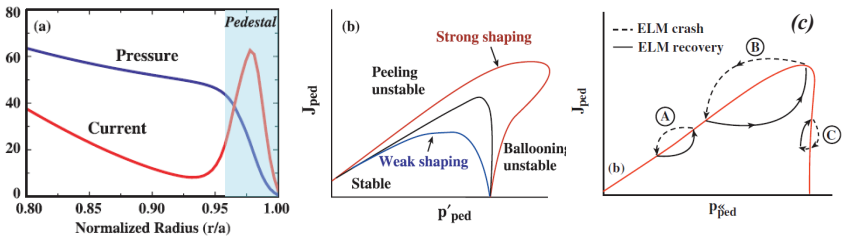

Figure 2-2 *Physics of ELMs:* **a)** *Typical H-mode pressure and current profiles. Schematic drawing of the* **b)** *ELM stability boundaries for different plasma shaping and* **c)** *the crash and recovery cycle of the three main ELM types as a function of edge current and pressure gradient. A: Type-III, B: Type-I and C: Type-II (Figure taken from [29])*

ELMs are generally classified into several categories. The most common types are labelled by roman numbers as Type-I, Type-II and Type-III that differ in frequency and magnitude. As shown in figure 2-3 they can go from narrow burst of large magnitude, to moderate burst separated in time and finally to small amplitude continuous excitation corresponding to Type-I, II and III respectively. In case of Type-III ELMy H-mode the continuous excitation keeps the edge pressure stabilized at a low level, thus eliminating the benefits of H-mode. This is not a desirable. Type-II ELMs represent the intermediate state. The average edge pressure gradient is stabilized at a reasonably high level, whereas the impurity levels are kept to an acceptable low level, thus making this a valuable operational

mode. Finally the large type-I ELMs can lead to no significant reduction in the energy confinement time but at the same time pose a threat by the corresponding high heat loads on the divertor targets and first wall elements. Transient heat loads associated with Type-I ELMs can reduce the lifetime of the divertor target plates drastically through erosion and/or sublimation to a few experimental days. Their amplitude needs to be controlled, thus there is a strong focus on ELM mitigation techniques in fusion research.
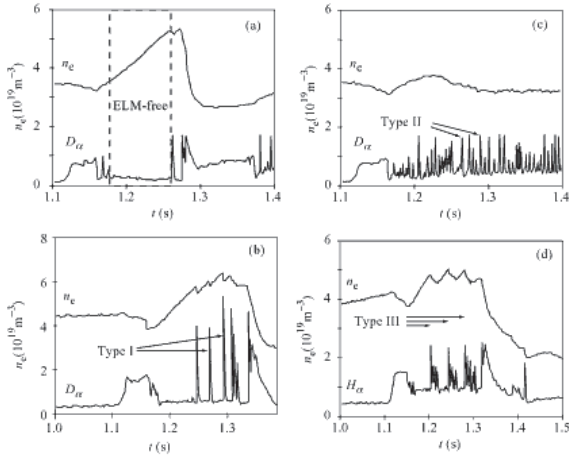

Figure 2- 3 *ELM categories based on D_α or H_α emission and electron density at ASDEX.*
a) ELM-free operation, b) type-I ELMs, c) type-II ELMs and d) type-III ELMs
(Figure taken from [30])

ELM mitigation techniques need to decrease ELM loads to plasma facing component to tolerable levels at the same time maintaining the required global confinement properties. An optimal tool thus would decrease the ELM size, with the least amount of reduction in the pedestal pressure and thus plasma performance. The two main techniques considered for ITER are edge magnetic field ergodization and pellet-induced ELMs. The use of resonant magnetic field perturbation induced by dedicated saddle-coils has been pioneered by DIII-D [31] and since then investigated in several other devices. Applying perturbation to the magnetic field structure at the edge increases cross-field transport and reduces the pressure gradient below the critical value. Although the method shows large potential, the results are not yet conclusive on the physical understanding and operational conditions. Pellet triggering [32] on the other hand is a robust reliable ELM mitigation method proven to work in all

regimes prone ELMs. This method relies on the experimental observation that the ELM frequency is inversely proportional to its size [33]:

$$\frac{\Delta W_{ELM}}{W} \cdot f_{ELM} \cdot \tau_E = 0.2 \qquad (2\text{-}8)$$

where ΔW_{ELM} and f_{ELM} are the ELM losses and frequency, W is the plasma energy and τ_E the plasma energy confinement time. By repetitive injection of small pellets, the frequency of ELMs can be increased, thus the heat loads decrease without contributing significantly to core fuelling.

2.1.2 H-modes without impurity transport relevant instability

Quiescent H-modes have very good confinement, capable of reaching the highest confinement values and best performance among H-modes in fusion. This can be however only achieved transiently. Due to increased particle confinement and the lack of edge instability increasing the impurity transport, impurities accumulate in the plasma core, thus the excessive radiation losses lead to back-transition or radiation collapse of the plasma. These H-modes are generally referred to as **ELM-free H-modes** in tokamaks and **Quiescent H-mode (H*)** in the W7-AS stellarator.

2.1.3 H-modes with edge harmonic oscillations

There are several H-modes with milder edge instabilities than ELMs avoiding the detrimental effect on the first-wall components. These processes also limit the impurity concentration to a tolerable level as well as provide good confinement with the possibility of steady-state operation coupled to benign plasma-wall interaction. The first of such instability is the **edge harmonic oscillation (EHO)** found in an ELM-free H-mode with stationary radiation levels in the low collisionality regime called **Quiescent H-mode (QHM)** at DIII-D [34,35]. The QHM has been subsequently demonstrated at ASDEX Upgrade [36,37], JT-60U [38] and JET [39]. At present the QHM mode is the only stationary ELM-free H-mode that is present in the low edge collisionality regime $\nu^* < 1$ relevant for future fusion reactors.

At ASDEX Upgrade the QHM-mode is obtained with NBI injection opposite to the plasma current direction (counter-injection, has lower heating efficiency as co-injection), improved geometry for good divertor pumping conditions and a larger distance between the plasma and first-wall elements. Compared to the typical Type-I ELMy H-mode, the density

values slightly decreased, whereas the energy confinement time and poloidal β improved (to about 10% above the ELMy H-mode values). It is not clear what causes the ELMs to disappear as the pedestal pressure is not reduced compared to the ELMy case. It is speculated whether the increased strong radial electric field (and associated ExB flow) shear observed during the phase can act as a stabilization for ELMs.

Beside strong m=1, n=1 fishbones in the plasma core characteristic of discharges with counter-injection, two characteristic MHD modes have been observed in the plasma edge by magnetic pick-up coil measurements as shown on figure 2-4:

a) *Edge harmonic oscillations* (EHOs) - a narrow-band n=1 oscillation with low frequencies around 10kHz and harmonics clearly visible up to n=11. Besides the magnetic coils, the mode is also observed on SXR[5], ECE[6] and reflectometry[7] measurements that were used to determine the radial localization of the mode, suggesting that it reside in the plasma edge just inside the separatrix (q~3). It is poloidally not localized as expected from a ballooning type of mode, but rather seems to originate from the X-point region. Higher fast particle densities measured by neutral particle analyser and correlation between the fast particle losses and the magnetic and divertor D_α data indicate a possible role of fast particles in the EHO cycle.

b) *High frequency oscillations* (HFOs) - high frequency oscillations around 350-500kHz with bursty structure found by fast magnetic pick-up coils with a sampling rate of 2.5MHz. They seem to rotate in the electron diamagnetic direction[8] and have a poloidal mode number around 6. These HFO bursts are phase-correlated with the EHO modes and their amplitude correlates with the divertor D_α intensity fluctuations suggesting a possible role in particle transport. Due to its characteristic high frequency that is out of range of other diagnostics, no more information could be obtained about this mode.

At present the relation and causality of the EHO and HFO modes is not clear, nor is there direct evidence on their driving mechanism. The presence and increased magnitude of the fast ion population in that local region may suggest that they might be a type of fast particle driven instabilities.

---

[5] Soft X-ray spectroscopy (SXR): plasma diagnostics with its signal proportional to $Z_{eff} \cdot n_e^2 \cdot T_e^{1/2}$ where Z_{eff} is the effective charge.
[6] Electron Cyclotron Emission (ECE) radiometer: plasma diagnostics measuring electron temperature profiles.
[7] Reflectometry: plasma diagnostics measuring electron density profiles.
[8] Direction of the diamagnetic drifts with net velocity $v_D = -(\text{grad } p \times B)/(q \cdot n \cdot B^2)$ where q is the charge.
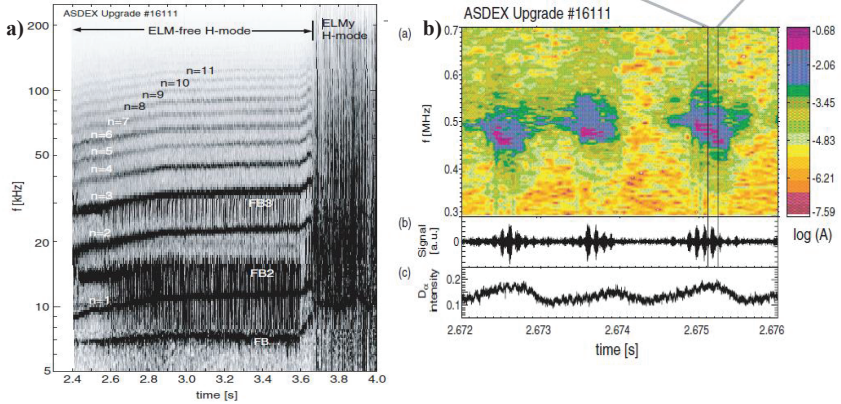
Figure 2-4 a) *Wavelet spectrogram of magnetic pick-up coil signal from the outboard midplane showing a coherent mode with harmonics labelled up to 11 beside strong fishbone (labelled FB) activity.* **b)** *FFT spectrogram of the fast pick-up coils showing bursts of HFO beside time traces the raw signal and the D_α intensity from the outer divertor. (Figures taken from [36])*
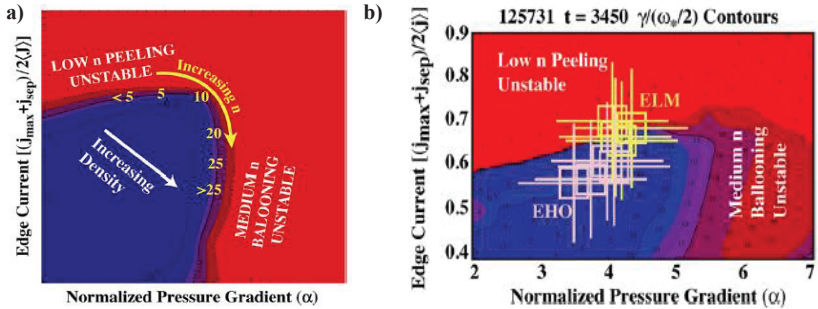

Figure 2-5 a) *Simplified peeling-ballooning stability diagram from ELITE of edge H-mode plasmas.* **b)** *Peeling-ballooning stability diagram from the ELITE code showing growth rate contours of the most unstable mode. ELM and EHO modes are calculated for a series of typical QHM discharges. (Figures taken from [35])*

At DIII-D the QHM mode has been obtained with similar conditions and properties and furthermore has recently extended to co-injection NBI pulses as well in a reactor-relevant collisionality and β regime. The QHM mode here is studied inside the peeling-ballooning picture (i.e. that the modes are driven by edge pressure gradient and edge current density) and modelled by the ELITE code [40,41]. Thus the EHO modes showing similar experimental properties as at AUG are thought to be a low n peeling mode driven unstable by rotational shear at the plasma edge slightly below the ELM stability limit (see figure 2-5). It is unclear why this mode becomes quasi-stationary.

2.1.4 H-mode with (quasi-)coherent oscillations

The EDA mode [42,43] was the first regime discovered at Alcator C-Mod, that provided particle and impurity control at steady-state density and radiated power conditions. It shows good core energy confinement, but lower edge particle confinement, thus whereas the energy is maintained in the plasma center, the impurities entering from the edge do not accumulate. No significant difference has been found comparing ohmic and ICRH heated EDA and Quiescent H-mode regimes, suggesting that fast particles do not play a major role here. The key parameters to reach EDA regime seem to be the plasma shape and the edge safety factor q95, e.g. in standard plasma shape $q_{95}>4$ has to be reached.
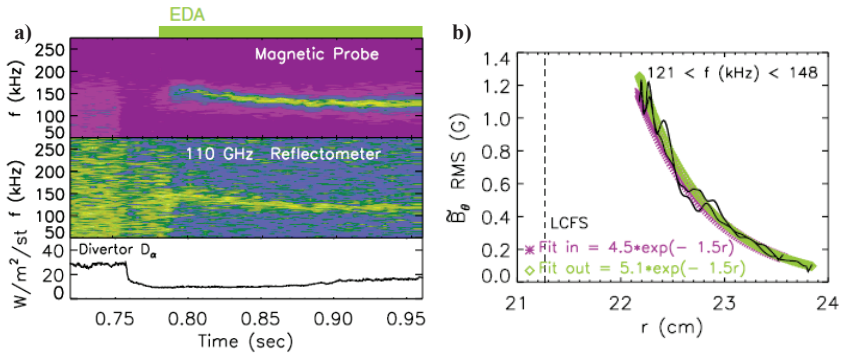

Figure 2-6 a) *Time evolution of auto-power spectra of a Mirnov magnetic and an edge reflectometer signal during the EDA mode showing the distinct narrow-band QC mode.*
b) *Radial decay of the QC mode in the EDA regime as measured by the fast-scanning probe (Figures taken from [44])*

The edge fluctuation present in EDA is called Quasi-Coherent (QC) mode shown in figure 2-6, observed on magnetic, density and potential fluctuations of Mirnov, edge reflectometry, phase contrast imaging[9] and fast-scanning Langmuir probe[10] signals respectively. It is a high frequency (f~50-120 kHz), short wavelength (k_{perp}~1.2 – 4 cm^{-1}) thus high mode number MHD mode localized in a narrow regime of few mms near the bottom of the density pedestal. Based on the fast scanning Mirnov coil measurements the amplitude of the QC mode is about $5 \cdot 10^{-4}$T extrapolated to the separatrix and based on the decay length along the major radius (shown in figure 2-6b), the toroidal mode number is high, around n~30. The mode is observed on the low field side with very high poloidal mode numbers ~ 100, suggesting a ballooning characteristic in the peeling-ballooning picture. No higher harmonics are detected, suggesting a purely sinusoidal mode. The QC mode propagates in the electron diamagnetic direction[11] and with its amplitude correlating well with the effective particle transport and with the potential and density fluctuations sufficiently being in phase to substantially enhance the edge particle transport. Indeed it appears to drive a time-averaged particle flux in the order of the total fuelling rate, thus it is believed to be responsible for the enhanced particle transport in the edge (shown in figure 2-7).
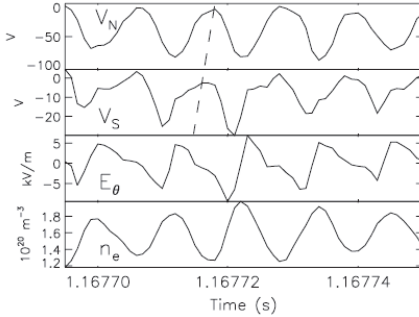

Figure 2-7 Time traces of raw Langmuir probe measurements from the north (N) and south (S) probe of a reciprocating probe, poloidal electric field and electron density showing the QC mode. The dashed line indicates the direction of propagation of the mode in the electron diamagnetic drift direction. The lower two plot shows that the QC mode is sufficiently in phase with the poloidal electric field and electron density to drive substantial particle transport. (Figure taken from [44])

To investigate the underlying physics of this mode, the EDA plasmas were modeled by the BOUT boundary-plasma turbulence code [45] that can model radially localized

---

[9] Phase contrast imaging: plasma diagnostics measuring density fluctuations with 2D spatial resolution in the plasma edge.
[10] Langmuir probe: plasma diagnostics measuring electron temperature and density fluctuations.
[11] Direction of the diamagnetic drifts with net velocity v_D= -(grad p x B)/(q·n·B^2) where q is the charge.

boundary-plasma turbulence by solving the Braginskii equations (collisional plasma in a two-fluid picture) in a realistic divertor configuration. The dominating instability found was identified as a resistive X-point mode [46], a type of resistive ballooning mode strongly influenced by magnetic geometry near the X-point [45,47]. It was found that the large pedestal pressure gradient with the locally unfavorable magnetic curvature drives this mode and is radially localized to the pedestal area. The mode is electromagnetic at the outboard midplane transforming into a electrostatic resistive mode near the X-point. The BOUT code also predicts the downward frequency sweep due to changes in the plasma rotation and the dependence on q_{95} as observed in the experiments. The characteristics of this resistive X-point mode are thus in very good agreement with the experimental description of the QC mode.

The EDA regime was partially reproduced on DIII-D and ASDEX Upgrade tokamaks, when the edge dimensionless parameters β, ν^*, ρ^* (Larmor radius normalized to the plasma radius) were matched and a similar edge fluctuation was observed. However due to the different operating window related to differences in the L-H threshold, steady-state ELM-free operation could not be reached (periodic ELMs, increasing edge densities) indicating that the strength of the mode was insufficient for the control of impurities. Similar QC fluctuations were observed in the 50-180kHz range were observed as well in PDX [48] and PBX-M [49] fusion experiments.

At the **JFT-2M** (R=1.31m, a=0.35m, $\kappa \leq 1.7$) tokamak [50] in Naka, Japan the **High Recycling Steady (HRS) H-mode** [51] is a high density ($n_e/n_{Gw}\sim0.7$), good confinement ($H_{98P}\sim1.6$), steady state H-mode regime with complete disappearance of large ELMs (smaller ELMs can still be observed). The HRS H-mode has been obtained under boronized first wall conditions (deposition of a thin boron layer by glow discharge process to improve vacuum conditions, reduce the number of impurities originating from the first wall) and low q_{95} ($2<q_{95}\leq3$) with co-, counter- and balanced NBI heating. The regime is compatible with their improved core confinement mode reaching transiently $\beta_N H_{98P}\sim6.2$.

Accompanying the HRS mode, **coherent magnetic fluctuations** were observed (shown in figure 2-8) with their appearance correlated with enhanced particle transport. The modes identified from magnetic measurements include a high frequency (f>200kHz) mode with intermediate mode number (n~7) and a low frequency (f~50-120kHz) mode with low n~1 mode number. The nature of these modes is still under investigation.
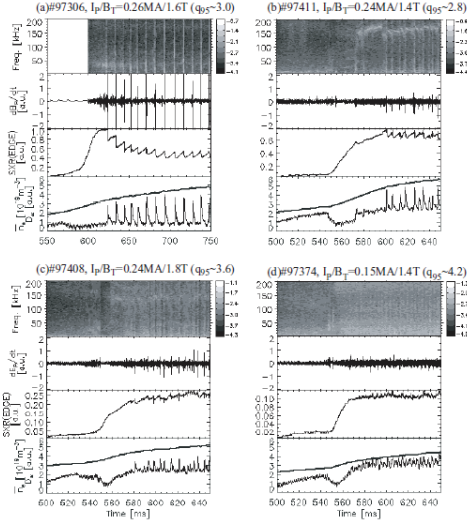
Figure 2-8 *Comparison of different types of H-mode at the JFT-2M after boronization. Spectral time history of magnetic fluctuations and time history of the edge SXR, line-averaged electron density and D_α intensity is shown for a) ELMy H-mode, b) combined Type-I ELMy and HRS H-mode, c) HRS with grassy-like ELMs and d) HRS with dithering (Figures taken from [51])*

The characteristics of the magnetic fluctuation and the H-mode itself shows many similarities to the EDA mode in Alcator C-Mod including similar access conditions connected to a collisionality threshold.

2.1.5 The High Density H-mode (HDH)

In 2001 the island divertor concept, an equivalent solution to the poloidal field divertor of tokamaks, had been realised at the W7-AS stellarator (Garching, Germany) favoured for particle control and mitigation of plasma-wall interaction. It led to the discovery of the new improved ELM-free confinement regime, the High Density H-mode [15]. The exciting new feature of this H-mode was that it coupled high energy confinement to low impurity confinement enabling the achievement of very high densities (up to $4\cdot10^{20}$ m^{-3}) under controlled, quasi-stationary conditions. This means, that it had not been prone to impurity accumulation leading to radiation collapse, the standard and defeating feature of typical high density plasmas. It reached partial detachment, thus substantially reduced power and particle fluxes to the material surfaces. The energy confinement time (τ_e) was enhanced by up to a factor of two ($2\cdot\tau_e^{ISS95}$, where τ_e^{ISS95} is the ISS95 stellarator scaling) whereas there was a significant reduction in the impurity retention times. This is illustrated in figure 2-9 among other variations in the main plasma parameters in an electron density – NBI heating power scan of a series of stationary discharges. An average β value of 3.1 has been achieved with no

evidence for β-stability limit. These properties are essential elements of a good confinement regime, making it an excellent candidate for future operation of helical fusion devices such as stellarators or stellarator reactors. In fact, the HDH mode is a favoured operational regime of the next (step) device, the Wendelstein 7-X stellarator (R=5.5m, a_{eff}=0.5m) now under construction in Greifswald, Germany.
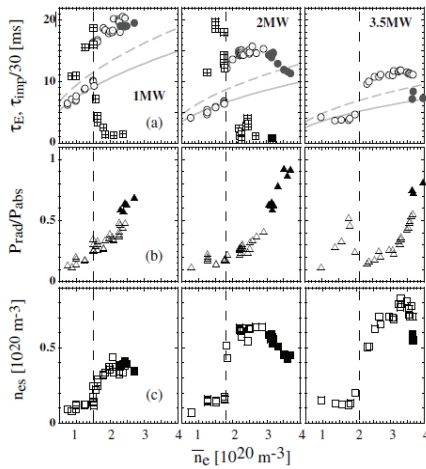

Figure 2-9 Density scan of various plasma parameters at three NBI heating power values, namely the electron (τ_E) and impurity (τ_{imp}) confinement time including the curves of the related ISS95 (solid line) and the dedicated W7-AS (dashed line) scaling, the radiated power fraction (P_{rad}/P_{abs}) and separatrix electron density (n_{es}). Open and solid symbol represent attached and detached plasmas respectively. The dashed vertical line represents the transition to the HDH regime. (Figure taken from [15].)

The HDH mode existed above a power-dependent density threshold (n_e^{th}), after either an ELMy or a quiescent H-mode phase in the high collisionality plasmas. This regime was only accessible via NBI heating as the needed threshold density lay above the cut-off density ($n_e^{cut-off}$=1.2·10^{20} m^{-3}) of the available ECRH heating scheme. To reliable enter this regime the operational scenario required a rapid density build-up by gas puffing during the NBI initiation at the start of the discharge. It had been observed both in divertor and limiter plasmas as well. Figure 2-10 shows the operational space of the different H-modes on W7-AS in form of an electron density – heating power diagram. The HDH mode could not yet be reproduced at the other large-scale stellarator LHD, indicating that the transition physics is not well understood.

Generally entering the HDH phase the density profile severely flattens at a higher density value and a very sharp gradient forms at the plasma edge, whereas in contrary the electron temperature profile increases but retains its shape as shown in figure 2-11. The

35

fundamental change in the radiation profile measured by a bolometer[12] array is shown in the figure as well. The normal confinement is plagued by increasing impurity accumulation in the core as shown by the time evolution of the profiles. On the contrary the HDH phase shows an edge localised radiation moving gradually inward as detachment sets in at higher densities relatively stationary in time.
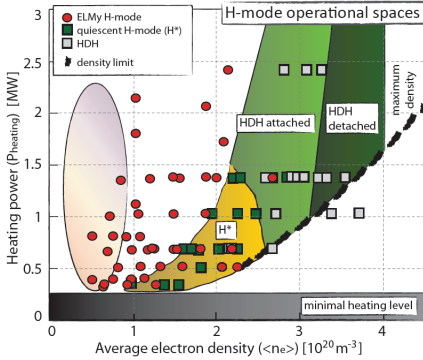

Figure 2-10 Operational space of the different H-mode confinement regimes of W7-AS in the absorbed power vs. average density plane in divertor configuration but slightly varying island size based on both, density ramp experiments and under stationary conditions. The density limit is calculated from [52]. (Figure based on [9])
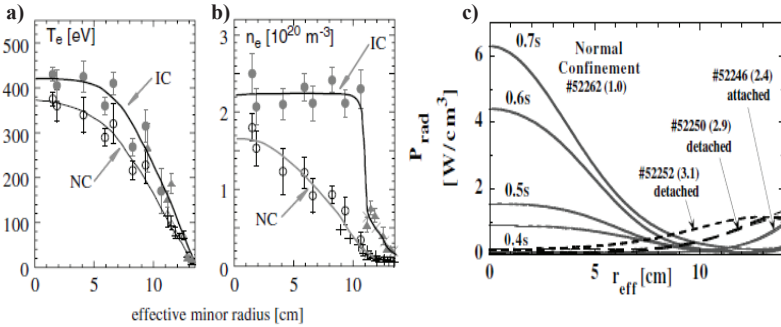
*Figure 2-11 Comparison of electron temperature (**a**) and density (**b**) profiles as well as radiation (**c**) profiles for the normal confinement and the HDH regime (here entitled IC as improved confinement) (Figures taken from [15])*

The investigations showed that the improved energy confinement time is related to the broader temperature profile [15]. Based on neoclassical calculations this, together with temperature screening, would reduce the inward pinch but due to the steep density gradient it

---

[12] Bolometer: plasma diagnostics measuring the total radiation of the plasma.

would still confine impurities in the plasma core. Also comparing the Quiescent and HDH phase in a dedicated single discharge, where the transition has been triggered by a slight increase of the electron density, showed no significant difference in the form of the electron density and temperature profiles (figure 2-12a). So the significantly increased impurity transport in the HDH case cannot be solely related to the density profile. The impurity flushing observed in the experiments could be reproduced by assuming enhanced impurity diffusion in the plasma edge in the calculations (figure 2-12b) [53]. The underlying mechanism for this is however yet unclear. The HDH regime shares many similarities with the previously introduced EDA mode, where the present QC modes are the mechanism invoking the impurity flushing. Such or a different mode that might be involved in the impurity transport has not been identified at W7-AS.
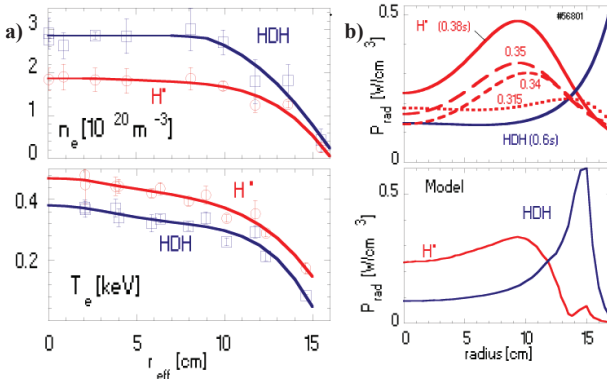

Figure 2-12 a) *Experimental electron density, temperature profiles for quiescent and HDH plasmas.* ***b)*** *Experimental and modelled radiation profiles for quiescent and HDH plasmas. Figure taken from [53]*

2.2 Pellet physics

Injection of small pieces of different solid materials called pellets [54,55] into plasmas is a well established fuelling, controlling and diagnostic method in fusion plasma physics. Frozen Hydrogen isotope pellets (H, D, planned T and DT in ITER) are commonly used for fuelling to maintain the required fuel content of the plasma (large pellet size, deep penetration) or to trigger ELMs (small pellet size, shallow penetration). Furthermore core fuelling by large pellets can be used to decouple core and edge parameters achieving peaked

density profiles. Impurity pellet of high Z material on the other hand are used for diagnostic purposes and for fast reduction of the plasma temperature during disruptions.

2.2.1 Pellet theory

Theoretically, the interaction of cryogenic pellets with the magnetized plasma is a complex 3D phenomenon, where for a proper description the use of time-dependent MHD and atomic physics models are required. It can be divided into three main phases: preheating, ablation and the transport of the ablated material.

The pellet entering the plasma is suddenly directly exposed to a large number of energetic particles. At first – due to the difference in the thermal velocities of electrons and ions – the pellet surface will be charged negatively, and the arising classic electrostatic shielding reduces the electron and increases the ion flux until the two equal. During this short period the surface of the pellet is subject to competing processes, i.e. sputtering, blistering and mechanical erosion. The phase ends as the pellet surface reaches the sublimation energy. The length of this first preheating phase thus depends through the sublimation energy on the pellet material. For impurity pellets such as carbon (E_{subl}=7.5 eV) or lithium (E_{subl}=1.6 eV) this phase takes considerably longer than for hydrogen isotopes (E_{subl}=0.01 eV). The duration of this phase is however in the submicrosecond range and thus negligible compared to the second phase.

In the ablation phase the energy transported by the background plasma particles (~eV-keV) start to ablate the pellet surface. Due to the low sublimation energy of the Deuterium ice (~0.005eV) a neutral cloud is formed around the pellet on a very fast, 100 ns time scale shielding the pellet from the background plasma particles. The ablation process here is self-regulating as the neutral cloud with radius R_{nc} always self-adapts to complete the shielding. When the shielding is complete ablation stops, however it is reduced continuously due to the expansion of the cloud and then ablation restarts again. During spherical expansion, the cloud is further heated and its particles become ionised. When the ionisation degree reaches a few percent, with increasing conductivity the magnetic field is frozen in the cloud and the radial expansion of the then ionised cloud stops at radius R_{ic}. The ablatant material is then confined in a flux tube of R_{ic} radius and – with the cross-field motion stopped – the expansion continues along the magnetic field with a cloud length of Z_{ic}. This is called a channel flow. The pellet cloud structure just described is illustrated on the schematic figure 2-13. The pellet leaves part of its ionized cloud attached to the magnetic field as it travels across the field line. Detached from the pellet, this ablatant material then gets transported toward the low field side by the drift due to the gradient of the magnetic field [11].
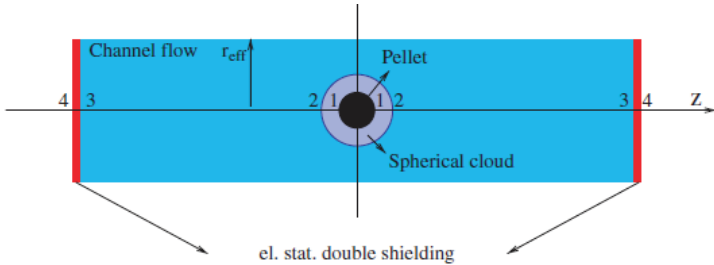
Figure 2-13 *Cloud structure around the pellet with the different shielding regions indicated as follows: 1-pellet surface, 2-spherical cloud surface, 3- channel flow surface, 4-cloud surface. Z points in the direction of the magnetic field, whereas r_{eff} is the effective radius of the flux tube (Figure taken from [56])*

The ablation rate, the number of eroded particles from the pellet material per second, is defined by the balance between the available energy flux and the flux required to remove the particles from the pellet (dissociation, ionisation and acceleration). The magnitude of different shielding mechanism play a crucial role in process, as they determine what fraction of the background plasma particles, that is the incoming energy flux, actually reaches the pellet. The main shielding mechanisms by order of importance include:

a) gas dynamics, i.e. shielding of the neutral and/or ionized part of the pellet cloud due to collisions between the cloud and incident plasma particles. This is responsible for the ionization and heating of the ablated material in the cloud. Hydrogen isotopes are generally completely shielded due to their low sublimation energy, whereas in case of impurity pellets the shielding is only partial.

b) electrostatic shielding due to the possible negative charge of the cloud with respect to the background plasma. The arising negative potential repels electrons and accelerates ions, thereby lowering the electron energy flux at the cloud periphery and the pellet surface as well.

During the last three decades a number of models have been developed to predict the ablation rate using different approximations of varying complexity. In early models only gas shielding had been considered assuming spherical cloud expansion and mono-energetic background electron beam. The best known hydrodynamic model developed for Hydrogen pellets is called the **Neutral Gas Shielding (NGS)** model [57,58]. This hydrodynamic model assumes steady-state, shock-free transonic flow and spherical symmetry for the energy flux

reaching the pellet and its cloud and also for the expansion of the ablated material. Based on the above assumptions, the ablation rate scaling can be derived analytically in the following closed form:

NGS ablation scaling: $dN/dt = 4.12 \cdot 10^{16} \cdot r_p^{1.33} \cdot n_e^{0.33} \cdot T_e^{1.64}$ [m,m^{-3},eV]   (2-9)

where dN/dt is the ablation rate, i.e. number of ablated particles per second, r_p is the pellet radius, n_e and T_e are the local electron density and temperature values.

Due to the importance of the gas dynamics, the NGS model sufficiently reproduces the experiments with moderate injected heating power and is still widely in use. In case of high injected heating powers fuelling efficiency degrades and over-ablation is observed, often localised in case of ECRH or ICRH, i.e. localised high-energy electron or ion heating. In case of ion heating this is due to the immediate increase of the ablation rate due to the deposited energy of the hot ions in the plasma cloud and pellet surface. High energy electrons on the other hand heat the ice in volume yielding and thus can cause the sublimation of the whole pellet.

In the next step ablation models were developed that took into account more shielding effects, first still in a simplified form later in a more comprehensive way. The **NGSE** model complemented the neutral gas shielding with the electrostatic shielding. On the other hand the **LLP code** described the change in the ionized cloud expansion geometry going from spherical to "cigar-shaped", i.e. elongated along the magnetic field line [59]. One of the present ablation codes, the **Hybrid code** combined the previous models by describing the neutral spherical neutral cloud by the NGS model and the dynamics of the ionized cloud elongated along the field lines by the LLP code [56]. The comparison of the mentioned models is summarized in table 2-1 regarding the shielding mechanism included in the models. Due to the complex nature of these codes the ablation rate cannot be derived analytically in a closed form as a simple power law as in case of the NGS model.

Table 2-1 *Comparison of the theoretical ablation models/codes regarding shielding types included in the models*

Name	NGS	NGSE	LLP	Hybrid
Spherical cloud	X	X	-	X
Channel flow	-	-	X	X
Electrostatic double shield	-	X	X	X

It should be noted that although the prediction of present ablation codes for present day tokamaks generally agree with the NGS model. Due to the difference in the plasma

parameter regime and the arguments given before, the extrapolation to reactor size devices differs by about a factor of 1.5-3. Furthermore it is an experimental fact, that the ionized ablatant is more-or-less periodically separated from the pellet [11]. This process is not modelled in detail, only approximated by some of the models. Thus experimental investigation is crucial in understanding and separating the different physical mechanism in pellet physics.

2.2.2 Pellet experiments

In experimental pellet physics, local measurement of the ablation rate is hard. At the RFX device ablation rate was estimated using the simultaneous evaluation of line integrated density measurements [60], otherwise a rough estimate is given by the measurement of the H_α light emitted by the ionized cloud that is proportional to the ablation rate except a slight temperature dependence through the ratio of the excitation and ionisation rate of Hydrogen isotope atoms. Generally experiments measure the penetration depth of the pellet, the distance it travels in the plasma until it is fully ablated and/or the deposition of the pellet material.

Discussions at the IAEA Technical Meeting of Pellet Injection (1993, Naka, Japan) motivated the establishment of a **International multi-machine Pellet Ablation DataBASE (IPADBASE)** containing a controlled set of experimental data on pellet parameters (pellet mass often expressed as number of particles in the pellet, velocity, penetration depth) and background plasma parameters (electron temperature and density profiles, magnetic configuration, auxiliary heating) that may be involved in the ablation process. Accordingly IPADBASE [14] contains data on Hydrogen and Deuterium pellet events injected from the low field (outer) side from several experiments with different magnetic configuration and auxiliary heating including JET, Tore Supra, DIII-D, TFTR, ASDEX Upgrade, JIPP T-IIU, RTP and T-10. Table 2-1 shows the range of selected experimental parameters excluding events from the database where the heating method (e.g. ECRH, lower Hybrid) causes suprathermal electron population.

As a multi-machine database covering a wide range of pellet and plasma parameters, the dataset was well suited to establish an experimental penetration depth scaling. The form of the scaling law was chosen to be a power-law of the NGS ablation rate scaling variables, i.e. pellet mass (m_p), velocity (v_p), central electron temperature ($T_{e,0}$) and density ($n_{e,0}$) with the penetration depth (λ) normalized to the minor radius (a).

IPADBASE penetration depth scaling: $\lambda / a = C \cdot T_{e,0}^{\alpha} \cdot n_{e,0}^{\beta} \cdot m_p^{\gamma} \cdot v_p^{\delta}$ (2-10)

Table 2-1 *Range of selected experimental parameters of IPADBASE*
(Ohmic, NBI and ICRH plasmas)

Device	v_p [m/s]	m_p [10^{20}]	I_p [MA]	B_t [T]	$n_{e,0}$ [10^{20} m^{-3}]	$T_{e,0}$ [keV]	P_{aux} [MW]
ASDEX-Upgrade	**240-1200**	**1.7-4.3**	**0.6-1.0**	**1.3-2.7**	**0.2-2.2**	**0.25-3.5**	**0.8**
DIII-D	630-1100	1.0-7.5	0.8-2.0	1.6-2.1	0.22-1.3	1.4-4.2	0-11.5
FTU	1300-1800	0.4-1.8	0.3-0.9	5.6-7.0	1.0-2.0	1.0-1.9	0
JET	460-1350	3.0-80.0	2.2-5.2	2.8	0.22-0.76	1.5-4.2	0-13.5
JIPP T-IIU	650	0.4-0.6	0.1-0.2	2.95	0.15-0.35	0.4-1.2	0
RTP	850-1050	0.3-0.5	0.08	2.2	0.38-0.43	0.65-0.85	0
T-10	400-800	0.2-0.45	0.2-0.4	2.85	0.4-0.75	1.0-2.8	0
TFTR	1000-2250	14-35	1.6	4.4	0.17-0.49	5.8-7.7	0-21.0
Tore Supra	600-3300	0.5-36.0	0.6-2	2.5-4.1	0.17-0.72	1.5-5.0	0-5.4

For comparison the NGS ablation rate scaling had been converted to penetration depth scaling assuming linear density and temperature profile forms. The regression analysis has been carried out on the whole database (excluding heating methods causing suprathermal electron populations) as well as on separate devices with significant variation in the scaling variables, and on the subset of data with no auxiliary heating, i.e. ohmic plasmas. Regression results are shown in Table 2-2 including the multiple correlation coefficient R [61] measuring the strength of dependence of the penetration depth on the four variables.

Table 2-2 *Experimental pellet penetration depth scaling exponents based on the IPADBASE datasets*

Device	C	$T_{e,0}$	$n_{e,0}$	m_p	v_p	R
JET	0.031	-0.89	-0.3	0.24	0.41	0.91
DIII-D	0.15	-0.6	0.23	0.1	0.27	0.76
Tore Supra	0.146	-0.84	0.07	0.18	0.27	0.70
ASDEX Upgrade	**0.208**	**-0.41**	**0.07**	**0.06**	**0.18**	**0.69**
All databases	0.079	-0.51	-0.03	0.12	0.32	0.67
All ohmic	0.076	-0.45	0.08	0.11	0.35	0.82
NGS model	0.079	-0.56	-0.11	0.19	0.33	

The experimental results reinforce the central role of electron temperature and significant roles of the pellet mass and velocity in the penetration. Except for the DIII-D result, the electron density exponent is relatively small, and scatters in both negative and positive direction. The significant variation in the exponents of the respective regression

variables and multiple correlation coefficients suggest that the scaling form may not yet be optimal, and could be improved by better description of the electron temperature and density profiles, inclusion of additional regression variables, nonlinear and cross-variable terms.

The IPADBASE collected information only on pellets injected from the outboard side. Due to the grad B drift effect mentioned before, the deposited material is however pushed down on the magnetic gradient, toward the outboard side. Thus to achieve deep fuelling, i.e. that the deposited material would be transported toward the center of the plasma, it is favourable to inject the pellets from the inboard side, where the drift acts in favour in contrast to the outboard launch, where it transports the material outward of the plasma [62]. Figure 2-14a shows the toroidal cross-section of a tokamak with the two injection geometry and the schematic figure of pellet's path and deposited material. Figure 2-14b shows the increase in the fuelling efficiency (increase in the target plasma particle content divided by the nominal pellet particle content) in an experiment with same pellet and plasma parameters.
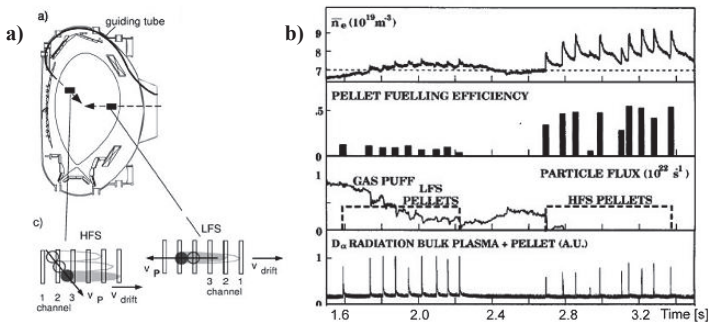

Figure 2-14 a) *Vessel cross-section with LFS and HFS injection geometry and the corresponding schematic sketch of the pellet's path and deposited material. (Figure taken from [11])* *b)* *Comparison of LFS and HFS pellet injection under identical pellet and plasma condition in the temporal evolution of plasma electron density, pellet fuelling efficiency, gas puff levels with the LFS and HFS pellet windows indicated and finally the D_α radiation where each spike corresponds to a pellet event. (Figure taken from [62])*

Although the new injection geometry is technically more difficult primarily due to the complicated guiding tube geometry used to transfer the pellet from the injector to the inner side of the vessel, the major tokamak experiments (including ITER) all adopted this approach.

A corresponding high field side pellet ablation database is not yet available with statistically sufficient amount of data to obtain a reliable penetration depth scaling.

Chapter 3

Plasma diagnostics and
Numerical Methods

The chapter presents a description of the plasma diagnostics analyzed in detail in this work and their respective analysis tools. Pellet diagnostics and the implemented statistical methods are introduced in 3.1, whereas fluctuation diagnostics to examine instabilities in the high density H-mode in 3.2 and 3.3 that is correlation analysis of density and time-frequency analysis of magnetic fluctuations. Detailed description of the measurements principles of other diagnostics can be found in [1,63]. Other diagnostics mentioned in the thesis are shortly described in the footnote at their first appearance and are included in the notations list at the end of the thesis for quick reference.

3.1 Statistical analysis of pellet events

The aim of this work was to develop a multi-machine pellet ablation database and use statistical techniques to analyze the datasets in order to establish a penetration depth scaling law on important pellet and plasma parameters. As the study presented here is focused on ASDEX Upgrade HFS pellet injections, first the experimental setup is introduced followed by a summary of present day pellet diagnostics and an overview on the implemented statistical concepts and methods.

3.1.1. The ASDEX Upgrade experimental setup and pellet diagnostics

The ASDEX Upgrade tokamak developed a well optimised HFS pellet injection system [64,65] consisting of a storage cryostat type pellet source, a centrifuge accelerator and a guiding tube system as illustrated in figure 3-1. The system is capable of delivering pellets of typical nominal pellet masses (1.4-3.8 $\times$ 10^{20} particles corresponding to 1.4-1.9 mm pellet

radius) with "moderate" to "very high" pellet velocities (240-1000 m/s) into the plasma at a poloidal injection angle of 72 degrees to the midplane from the magnetic high field side. HFS pellet injections require the pellet to be transferred from the centrifuge to the plasma through long curved guiding tubes. This results in massive pellet mass reduction and imposes restrictions on the maximum attainable pellet velocity as well. The grounds for this destruction are mainly the excessive mechanical stress due to uncontrolled impact of the pellet on the guiding tube wall and the high centrifugal pressure in small radius bends. The impact is reduced by the so-called Leidenfrost effect, formation of an insulating gas cushion underneath the pellet when sliding through the tube. However, heat transfer into the pellet through the insulating gas cushion is a further mechanism causing pellet destruction occurring at high velocities and small curvature radii of the guiding system. Thus the high curvature looping type experimental setup of the AUG guiding tube system – optimized for high speed and reasonable mass throughput – is accountable for the uniquely high HFS pellet velocities of the injection setup compared to the international values of ≤500 m/s.
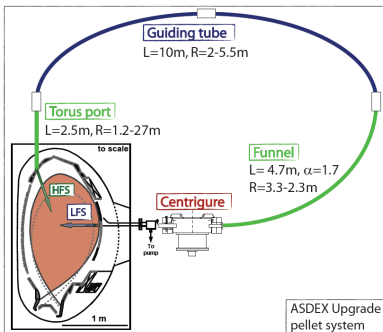

Figure 3-1 *The HFS pellet injection setup of the ASDEX Upgrade experiment.*

The determination of the three pellet parameters – mass, velocity and penetration depth – is essential in any pellet ablation study. The common approaches to measure these pellet parameters are summarized below.

Pellet mass. The most straightforward way to measure the pellet mass is by the **cavity** measurement. A cavity is a resonator into which a microwave signal is injected with a detector measuring the strength of the reflected signal. As the pellet enters the cavity its dielectric strength modifies the cavity's resonant frequency with the change being proportional to the pellet's mass. In practice the frequency of the injected signal is adjusted in a way to maximize the sensitivity to the given pellet mass range used, thus different cavities
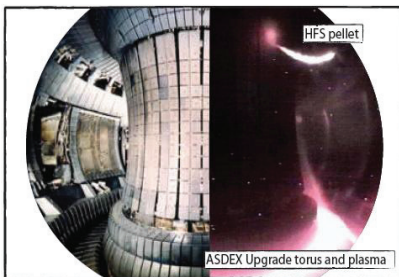
are used for 'small' and 'large' pellets. The detector output signal produces a Gaussian shape with its peak proportional to the pellet mass.

The second most common measurement of the pellet mass is through the **shadowgraphy** method, where two camera lines perpendicular to each other record a picture of every pellet before entering the plasma from the two angles. The 'shadow' of the pellets is then used to estimate their 3D shape and thus their volume and the corresponding pellet mass.

Pellet velocity. The pellet velocity can be determined in two ways: a) time of flight measurement between two fixed points along the injection trajectory such as light barriers or cavities assuming that the velocity remains constant or b) in case of a centrifuge based injection system from the revolution frequency of the centrifuge arbour.

Pellet penetration depth. The penetration depth of the pellet is either determined by the time of flight measurement using a photodiode signal measuring the length of the D_α emission of the pellet or by camera measurements capable of determining the 3D pellet path and cloud properties as well in case of a fast-framing multi-camera system. The curved pellet path, i.e. deviation in the toroidal and/or poloidal direction from the injection line shown in figure 3-2, is due to the asymmetry of the background electron or ion distribution. This creates an unbalance in the ablation of the different sides of the pellet, and the resulting rocket effect accelerates the pellet in the direction of slower ablation rates [66].

The penetration depth is ultimately the length the pellet travels in the plasma during its ablation in specific cases along a curved pellet path. It can be defined either from the beginning of the detected ablation or the pellet crossing the separatrix until the end of the detected ablation. The length between the starting and ending point can further vary as the length along the curved path or straight line, in meters or flux surface coordinates. The pellet path can also be separated into parallel and perpendicular components along the injection line. In any case the penetration depth can be defined and measured in a number of ways, and thus has to be explicitly stated in every analysis.

Figure 3-2 *HFS pellet injection at AUG*

3.1.2 Statistical methods

In the absence of theoretical understanding of given plasma phenomena, scaling laws are a common approach used in fusion plasma physics to predict given plasma quantities. The simplest empirical approach is then to accumulate data from several fusion devices for a large range of quantities and derive the scaling laws through statistical analysis. First the statistical properties of the dataset are analyzed, then model selection methods are applied to determine the statistically important parameter in the physical process under investigation. Log-linear regression is then used to obtain a scaling law based on these parameters. Finally to check the scaling law linearity and error analysis is applied to each regression parameter.

Statistical description of dataset. To best describe the pellet datasets **univariate statistics** are used to describe the ranges and distribution of the given parameters, and **correlation matrix** is used to describe the relation of the parameter to each other [67]. Estimated values of the standard deviation, skewness and kurtosis are defined as follows, where for a sample record $\{x_i, i=1, \dots N\}$, $\bar{x} = 1/N \cdot \sum_i x_i$ denotes the empirical mean of the distribution:

Standard deviation:
$$s = \left(\frac{1}{N-1} \sum_i (x_i - \bar{x})^2 \right)^{1/2} \tag{3-1}$$

Skewness:
$$\hat{\gamma}_1 = \frac{N}{(N-1)(N-2)} \sum_i \left(\frac{x_i - \bar{x}}{s} \right)^3 \tag{3-2}$$

Kurtosis:
$$\hat{\gamma}_2 = \frac{N(N+1)}{(N-1)(N-2)(N-3)} \sum_i \left(\frac{x_i - \bar{x}}{s} \right)^4 - \frac{3(N-1)}{(N-2)(N-3)} \tag{3-3}$$

Empirical datasets are usually not homogeneously distributed in variable space and they can be also correlated resulting from technical or scientific limits and parametric dependences, correspondingly. The relation of the parameters can be given in form a correlation matrix, where the correlation coefficient between two variables as given below measures the strength of correlation between the two parameters. As it can be seen from the definitions the square root of the variance is called standard deviation.

.

Variance
$$\text{var}(x) = \frac{1}{N-1} \sum_i (x_i - \bar{x})^2 \tag{3-4}$$

Covariance
$$\text{cov}(x, y) = \frac{1}{N} \sum_i (x_i - \bar{x})(y_i - \bar{y}) \tag{3-5}$$

Correlation coefficient $\quad\quad \operatorname{cov}(x, y) = \dfrac{\operatorname{cov}(x, y)}{\sqrt{\operatorname{var}(x) \cdot \operatorname{var}(y)}}$ $\quad\quad\quad\quad$ (3-6)

Model selection procedure. A common approach is to fix the regression variables a priori based on a certain theory. In this work, an alternative approach is used to study many possible parameters that can be physically relevant, that is a statistical approach was implemented to select the statistically relevant parameters of pellet ablation. In theory to find the best fitting subset of regression variables all possible subsets have to be compared. In practice, however, this concept may prove extremely time consuming and unrealizable due to the large number of regression variables and their many combinations. Also the chance of overfitting the dataset is prominent in such cases. In our case two model selection algorithms described in [67] have been used to find a good subset of variables. These methods are the following:

The **Forward Selection Method** starts with one variable, and in each step the variable that causes the largest decrease of the 'Residual Sum-of-Squares' is added to the model, i.e. the variable having the highest partial correlation with the dependent variable (excluding the variables already inside the model). The variables are included as long as they all pass the Student t-test at a predefined confidence level.

The reverse procedure is called the **Backward Elimination Method**. It starts with all the variables included in the model and in each step the variable whose elimination causes the smallest increase of the 'Residual Sum-of-Squares' is excluded from the model. The variables are thrown out one by one until all the variables inside the model pass the Student t-test at the predefined confidence level.

Scaling law. The scaling law is derived using a log-linear regression technique using the parameters determined through the statistical model-selection procedure. The form of the scaling law is set a priori to be a power function:

$$Y = C \cdot \left(\prod_{i=1}^{p} X_i^{\alpha_i} \right) \cdot E \quad\quad\quad\quad (3\text{-}7)$$

which is a linear model on a logarithmic scale, i.e.

$$\ln Y = C' + \sum_{i=1}^{p} \alpha_i \cdot \ln X_i + \ln E \quad\quad\quad\quad (3.8)$$

49

where Y is the dependent variable, C is a constant, E is the error, p is the number of regression parameters, $\alpha_1, ..., \alpha_p$ are the exponents of regression parameters $X_1, ..., X_p$. After taking the natural logarithm on both sides, the coefficients α_i $(i=1,...,p)$ can be estimated by applying multiple linear regression. The **statistical significance** of the variable is measured by the ratio of the estimated exponent and its standard deviation. Furthermore to describe not only the variable's significance, but its variation as well, the **statistical relevance** is used. It takes into account the variable's parameter range to judge the practical influence of the variable's exponent. The statistical relevance is the product of the variation of the variable (logarithm of the maximum over the minimum of the variable) and the absolute value of its exponent [67].

Statistical significance: $\qquad R_i = \alpha_i / \sigma_i$ $\qquad\qquad\qquad\qquad$ (3-9)

$\qquad$ where σ_I is the standard deviation of the exponent

Statistical relevance: $\qquad D_{stat}^i = \alpha_i \cdot \ln\left(\dfrac{\max(X_i)}{\min(X_i)}\right)$ $\qquad\qquad$ (3-10)

Linearity. The linearity of each parameter can be analysed by plotting the variable against its **reduced residual**. For a given scaling law, the reduced residual corresponds to the ratio of the dependent variable and the scaling law while omitting the parameter under investigation, thereby excluding from the analysis other known dependences.

Reduced residual $\qquad RR(X_m) = \dfrac{Y}{f\left(X_i\right)_{i=1..n, i\neq m}}$ for scaling law $\quad Y = f(X_i)_{i=1...n}$ $\qquad$ (3-11)

$\qquad$ **Error-in-variables method.** The usual limitation of the ordinary least square procedure (OLS) is that it assumes that only the response variable, e.g. the penetration depth, and none of the regression variables are measured with an error. A graphical version of the errors-in-variables technique [67] can be applied to address in a simplified way the effect of measurement errors. Specifically the reduced residuals can be plotted against the studied variable, both normalised to their respective measurement errors to make the size of the errors on both axes the same. The slope of the main axis of a 95% prediction ellipse fitted to the data is obtained and scaled back to provide an estimate of the actual exponent that takes the measurement error of the variable into account. The inclusion of the measurement errors tends

to increase the absolute values of the estimates of the given exponent, and is considered to be an improvement of the exponents obtained by OLS [68].

3.2 Correlation studies of density fluctuations

3.2.1 The Lithium Beam Emission Spectroscopy (Li-BES) diagnostic

By observing light emitted by a neutral beam injected into hot plasma, it is possible to gain spatial and temporal information on density fluctuations in the long wavelength range (structure size of about a cm) believed to be important regarding the understanding of anomalous transport. At the W7-AS stellarator a 20-66 keV Lithium beam had been operated with strong Hungarian involvement providing vital information on core and edge density fluctuations from the Li (2p-2s) resonance line (radial resolution: 0.5cm, time response: $\leq$0.2ms, density range: $< 10^{18} - 10^{20}$ m^{-3}) [69]. Additional measurements for the fast fluctuations have been performed in certain measurement campaigns on a subset (typically 16) of observation channels with 1 µs time resolution. The radial range of the diagnostic depends on the plasma density. At low densities ($\sim 10^{19}$ m^{-3}) it covers half of the plasma radius, whereas at higher densities it can be limited to the outer 1-2cm due to strong beam ionization. The background due to the radiation of the plasma itself is obtained by periodically switching on and off the Lithium beam.
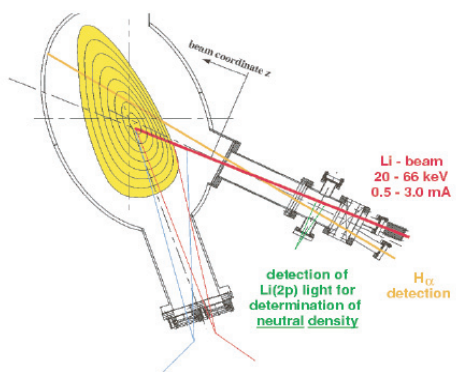

Figure 3-3 *Diagnostic layout of the Li-BES on W7-AS*

The proper density reconstruction method taking into account the light emitted at a given radius is affected by the entire plasma layer between that position and the plasma edge, including diagnostic limits and the methods viability is presented in detail in [69,70].

3.2.2. Correlation analysis

Due to the fact that the increased temporal resolution of the Li-beam measurement, i.e. the regime where fluctuations can be studied leads to the increase of the noise level and thereby to the breakdown of the density reconstruction method [70], correlation analysis of data proved to be a reasonable way. For repetitive phenomena, statistical properties such as correlation functions can be determined with high accuracy if the signals are sampled for a sufficiently long period.

As the emitted light depends on density and is mostly independent of the temperature in case of Li-beams, the autocorrelation functions of the beam light fluctuations (correlation at one place as a function of time delay) already give valuable information on the studied region. However as the beam light is not a local function of the plasma electron density, these light correlation function may differ considerably from density autocorrelation functions. Thus where density reconstruction is possible, the analysis of the correlation of the reconstructed density fluctuations is favourable. A method also exists which can infer the correlation functions of plasma density fluctuations from the correlation functions calculated from the beam light fluctuations.

The autocorrelation (AC) function for S signal at Z position for τ time lag is calculated as:

$$C^A(Z,\tau) = \int_0^T \widetilde{S}(Z,t)\widetilde{S}(Z,t+\tau)dt,\qquad(3\text{-}12)$$

where $\widetilde{S}$ denotes the fluctuating part of the signal as $S(Z,t) = \overline{S}(Z) + \widetilde{S}(Z,t)$, t is time and T denotes the measurement time (τ is in the µs timescale, T is in the 0.01-1 s range). In some cases this function is called autocovariance in the literature and the autocorrelation function arises by normalizing with the RMS function level. In this thesis Eq. 3-12 will be called autocorrelation function. The autocorrelation functions can be corrected for the photon noise contribution [70] affecting the first 5 µs if the beam light fluctuations are confined to a band sufficiently below 1 MHz.

Observed autocorrelation functions of the Li-beam diagnostic typically have one of the following forms [70,71]:

a) **triangle-like** AC functions correspond to sudden profile changes and slow relaxations and can be usually found in the edge and SOL region of the plasma. $B_\perp$ transport is probably involved.

52

b) **wave-like** AC functions are usually found in the plasma edge, but never in the SOL region. They are the density component of MHD waves and thus correlate well with magnetic fluctuations.

c) **peak-like** AC functions are typical SOL turbulence features, but can easily be found in the edge as well. It is detected by Langmuir probes as well. As they do not exhibit well defined frequencies, they are considered to be the signature of plasma turbulence.
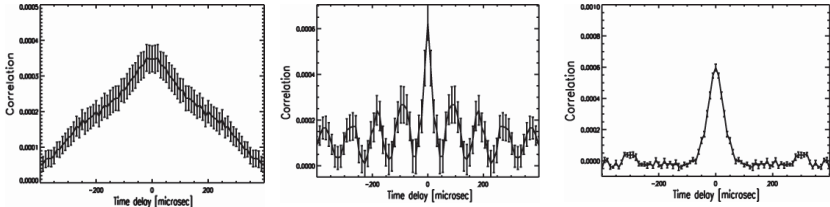

Figure 3-4 *Typical phenomena in the autocorrelation function of electron density fluctuations measured by the Li-BES diagnostics*

3.3 Time-frequency analysis of magnetic fluctuations

3.3.1 The Mirnov coil system

The temporal change of magnetic field components can be measured by sets of orthogonal, small cross-section, multiple-turn coils (figure 3-5) positioned on the inside of the vacuum vessel to determine the local field values normal and parallel to the vessel surface. The induced voltage in the coils is proportional to the time derivative of the component of the local magnetic field perpendicular to the plane of the coil. These coils measuring the magnetic field fluctuations are generally referred to as *Mirnov coils* and are commonly used to study MHD waves or instabilities.
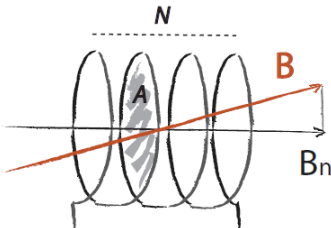

Figure 3-5 *Principle of the Mirnov probe – a coil measuring the magnetic field component along the coil axis (B – magnetic field, B_n – measured magnetic field component, N – number of turns in the coil of area A)*

Induced voltage: $\qquad V = N \cdot A \cdot \dot{B}_n \qquad$ (3-13)

MHD instabilities in the plasma are studied by their caused magnetic field perturbations. These, even in case of small amplitude instabilities, can be picked up by the Mirnov coils due their rotation with the plasma and diamagnetic velocities leading to timescales 3-4 magnitude shorter than the typical changes in the equilibrium magnetic field.

The primary information, such as frequency, amplitude and their time evolution, on the MHD instabilities is obtained from time-frequency analysis of the Mirnov signals, such as Fourier or Wavelet analysis. Often a larger set of Mirnov coils are arranged at different poloidal and toroidal locations to determine the structure of the magnetic perturbations as well. It should be stressed that the Mirnov coils do not give information on the radial localization of these instabilities.

Beside wall-mounted Mirnov coils, in some cases *reciprocating Mirnov probes* (MRCP) are used as well to probe the mode structure of given MHD instabilities. A few (1-3) small Mirnov coils are mounted on a dynamic rod and slowly inserted toward the plasma radially measuring the radial increase and decay of the mode's amplitude. The method takes advantage of the fact that mode amplitude decays exponentially with a decay rate dependent on the mode number.

The investigations on W7-AS were conducted on three poloidal arrays of Mirnov coils and the reciprocating Mirnov probe:

- *MIR-1 Channels 1-16:* poloidal array of 16 Mirnov probes sampled at 350 kHz on Module 1, recorded for limited time interval ~ 0.3-0.5 s
- *MIR-354 Channels 1-8:* poloidal array of 8 Mirnov probes sampled at 1 MHz on Module 3, recorded for a very short time intervals ~ 0.05s
- *MIR-354 Channels 9-16:* poloidal array of 8 Mirnov probes sampled at 1 MHz on Module 5, recorded for a very short time intervals ~ 0.05s
- *MIRTIM Channel 1:* a single Mirnov probe from the MIR-354 array sampled at 250 kHz, recorded for the whole length of the discharge.
- *MRCP Channel 1-2:* two Mirnov coils measuring the parallel and normal component of the magnetic field inserted into the plasma over a given time interval, sampled at 1 MHz, recorded for a short time interval ~0.05s.

3.3.2 Fourier analysis tools

Fourier analysis, a family of mathematical techniques based on decomposing signals into sinusoidal waves, is a well-established method to analyze fluctuations. In its basic form

represented by the Fourier series, a stationary sample x(t) periodic with a period T (thus fundamental frequency f=1/T) can be decomposed into sinusoidal waves as follows: (3-14)

$$x(t) = \frac{a_0}{2} + \sum_{i=1}^{\infty} (a_i \cos 2\pi i f t + b_i \sin 2\pi i f t) \qquad a_i = \frac{2}{T} \int_0^T x(t) \cos 2\pi i f t \, dt$$

i=0,1,2…

$$b_i = \frac{2}{T} \int_0^T x(t) \sin 2\pi i f t \, dt$$

i=0,1,2

The discrete finite range Fourier transform will be defined on the other hand as:

$$x(t) = \int_{-\infty}^{\infty} X(f) e^{2\pi j f t} df \text{ where the spectral magnitude is } X(f) = \int_{-\infty}^{\infty} x(t) e^{-2\pi j f t} dt \qquad (3\text{-}15)$$

Spectrogram is a common way to describe a time-varying spectrum. For a sample x(t) from a nonstationary process, the time interval (T) is divided into time segments (T_B=N·Δt, where N is the data values and Δt is the sampling interval for each discrete Fourier calculations) and the time averaged Fourier transforms are computed for each segment.

Time averaged Fourier magnitude: $SG_{xx}(f, t_i) = \frac{1}{T_B} \left| \int_{(i-1)T_B}^{iT_B} x(t) \cdot e^{-j2\pi f t} dt \right|$ where i=1,2,..T/T_B

(3-16)

 The magnitude of the obtained time-averaged Fourier transforms are then plotted over time and frequency in a 3D plot called the spectrogram. The spectrogram inherently involves a compromise between the time and frequency resolution that has to be decided in each specific case separately based on the properties and characteristics of the data and involved phenomena. The typical presentation of the spectrogram in fusion is a two-dimensional display of time versus frequency where the color value of the data point is proportional to the spectral magnitude. The spectrogram method used in the thesis uses linear continuous transforms and is described in detail in [72].

Chapter 4

Result I.

High Field Side Pellet Studies

Hydrogen isotope pellet injection became the leading technique for core fuelling and ELM control tool of modern fusion devices. In both applications, the key parameters are the penetration depth and the resulting particle deposition profiles. Large fuelling pellets have to reach beyond the pedestal region for effective core fuelling, whereas small ELM pacing pellets have to reach about the pedestal top for reliable ELM triggering [73]. As ITER relies on HFS pellet injection, for reliable extrapolation a suitable dataset and scaling analysis is needed.

The purpose of this project was the development of a multi-machine HFS database, first of its kind for HFS injection, with right quantity and quality of ablation data for statistical analysis to establish a penetration depth scaling. Secondary aim was to provide an adequate dataset with selective single parameter scans to benchmark and judge the weak and strong points of ablation models. Beside this case-to-case comparison of model simulation and data, comparison of the obtained statistical and known experimental scalings can also provide information on the accuracy of specific ablation models.

The first part of the chapter introduces the database developed at ASDEX Upgrade and Tore Supra tokamaks, later extended with DIII-D pellet data as well. The chapter continues to describe the statistical analysis conducted on the ASDEX Upgrade subset of the database that enabled the establishment of an empirical HFS pellet penetration depth scaling law including linearity and error analysis. The results are validated by dedicated experiments conducted at ASDEX Upgrade and compared to a theoretical model. The chapter concludes with discussion and considerations for the ITER device.

4.1 The international High Field Side Pellet Ablation Database (HFS-PAD)

The HFS-PAD database is a multi-machine pellet ablation database gathering Hydrogen isotope pellet data injected vertically or from the high field side of fusion devices to complement the LFS data in the international pellet ablation database, IPADBASE [14]. The database is based on the single HFS injection line at ASDEX Upgrade and three of the injection lines at Tore Supra (vertical, upper HFS and midplane HFS), later extended by HFS pellet data from DIII-D. The multi-machine database covers an extensive pellet and plasma parameter range shown in table 4-1.

The largest dataset based on AUG pellet injections is further divided into three subsets with 509, 197 and 30 pellet events respectively. The first two basic datasets are separated by diagnostic upgrade of the diode system measuring the D_α emission determining the penetration depth and pellet mass. The third set is a dedicated magnetic field scan to support the result of the statistical analysis.

Table 4-1 *Parameter range of the HFS-PAD database for the available three devices respectively including the number of pellets, pellet velocity, final (AUG, TS) or nominal (DIII-D) pellet particle content (i.e. at the end or start of the injection line), average (AUG, TS) or central (DIII-D) electron temperature and density.*

Device	pellet number	v_p [m/s]	m_p [10^{20} particles]	T_e [keV]	n_e [10^{20} m^{-3}]
ASDEX Upgrade (AUG)	736	240-1000	0.14-3.14	0.95-6.17	0.20-1.05
Tore Supra (TS)	81	61-265	0.47-2.73	0.26-0.89	0.16-0.40
Device	pellet number	v_p [m/s]	nominal m_p [10^{20} particles]	$T_{e,0}$ [keV]	$n_{e,0}$ [10^{20} m^{-3}]
DIII-D	9	118-223	7.25	1.5-5	0.17-0.72

To have the necessary confidence in an empirical scaling, the analysed dataset has to have large number of events spreading preferably homogenously a large parameter range and have uncorrelated variables as much as this is possible. All the datasets of the HFS-PAD database have been analysed, however only the first subset of AUG (consisting of 509 pellet events) gave the confidence for a possible reliable scaling. The analysis presented in the thesis is thus restricted to this AUG dataset that will be described in detail in the followings.

ASDEX Upgrade dataset 1. (2001-2004)

Data were collected from available HFS Deuterium pellet experiments without dedicated discharges in the period 2001-2004. After careful selection, the dataset was formed based on 509 pellet events from 37 type-I ELMy H-mode Deuterium discharges, heated mainly by neutral beam injection. The collected quantities cover a wide range of main plasma parameters (such as plasma density, temperature, energy, current, magnetic field, safety factor) and pellet parameters (pellet mass, velocity, penetration depth). The database also includes geometrical factors characterizing the plasma shape (e.g. elongation[13], lower and upper triangularity[14], minor radius, flux-surface distances) and heating schemes (ohmic, NBI, ECRH, ICRH). In total 25 parameters from 14 validated diagnostic measurements were collected. All plasma parameters were evaluated immediately prior to the pellet entering the plasma. An overview of the parameters that are deemed important for the scaling analysis is presented in table 4-2. In this table, notation and the units of parameters used are also indicated, as well as their parameter range and some univariate statistics. In table 4-3 the relationship between the parameters is described in form of the correlation matrix. It is to be noted that the dataset is not entirely homogenous and uncorrelated. Standard operational scenarios subject to operational and technical limitation lead to correlation, whereas the standard settings of specific experimental studies (e.g. always fast, small pellets for ELM pacing) cause inhomogeneity. These are the reasons that the observed correlation coefficients tend to be much larger than the expected value of the standard error for uncorrelated data (estimated by $SE = 1/\sqrt{N-1} = 0.044$, where N=509 is the number of pellet events).

The data acquisition algorithms developed to determine the main pellet and plasma parameters have been written in the IDL (Interactive Data Language) programming language for ASDEX Upgrade (later rewritten in MATLAB for Tore Supra). The following considerations were made regarding the electron temperature, density, pellet mass and penetration depth.

Electron temperature and density. For the electron temperature and density average values had to be taken since electron temperature and density profiles were not retrievable or accurate enough for every pellet event. The line-averaged density is taken from the fringe-jump corrected line-integrated density of the interferometer[15] signal crossing the midplane of the plasma divided by twice the plasma minor radius, i.e. $\bar{n}_e = \int n_e dl / (2 \cdot a)$.

---

[13] Elongation: geometrical parameter obtained ratio of the plasma half-height and half-width.
[14] Triangularity: geometrical parameter describing the plasma shape's deviation from an ellipse to D-shape.
[15] Interferometer: plasma diagnostic providing electron temperature profiles.

Table 4-2 *Univariate statistics of experimental parameters.*

Parameter name	Symbol	Unit	Range	Mean	Std. dev.	Skewness	Kurtosis
Average electron temperature	$\overline{T}_e$	keV	0.34 – 1.78	0.94	0.22	0.67	0.33
Average electron density	$\overline{n}_e$	10^{19} m^{-3}	3.01 – 10.6	7.57	1.75	-0.10	-0.89
Toroidal magnetic field	B_t	T	1.74 - 2.67	2.26	0.31	0.25	-1.61
Plasma current	I_p	MA	0.69 - 1.02	0.94	0.10	-1.16	-0.31
Safety factor	q_{95}		3.66 – 6.03	4.47	0.55	0.18	-1.08
NBI heating power	P_{NBI}	MW	0 – 9.80	3.00	1.63	1.03	1.59
Pellet particle content	m_p	10^{19}	0.69-15.11	3.84	2.48	1.19	1.36
Pellet velocity	v_p	m/s	240 – 1000	705	253	-0.20	-0.92
Pellet penetration depth	λ	m	0.09 - 0.46	0.25	0.08	0.03	-1.25
Plasma minor radius	a	m	0.48 - 0.54	0.51	0.01	-0.29	-0.08
Plasma volume	V_{plasma}	m^3	12.19 – 14.73	13.78	0.52	-0.97	0.65
Elongation	κ		1.35-1.80	1.69	0.04	-1.30	8.00
Triangularity (lower)	δ_{lower}		0.48 - 0.54	0.36	0.03	0.82	4.07
Triangularity (upper)	δ_{upper}		-0.04 – 0.38	0.12	0.08	-0.18	-0.60

Table 4-3 *Correlation matrix of experimental parameters.*

	$\overline{T}_e$	$\overline{n}_e$	B_t	I_p	q_{95}	P_{NBI}	m_p	v_p	λ	a	V_{plasma}	κ	δ_{lower}	δ_{upper}
$\overline{T}_e$	**1**													
$\overline{n}_e$	**-0.66**	**1**												
B_t	-0.37	0.29	**1**											
I_p	-0.13	**0.64**	-0.23	**1**										
q_{95}	-0.30	**0.56**	**0.78**	0.32	**1**									
P_{NBI}	**0.75**	**-0.62**	-0.40	-0.39	**-0.51**	**1**								
m_p	0.16	-0.21	0.35	-0.28	0.19	0.21	**1**							
v_p	0.11	-0.07	-0.42	-0.07	-0.42	0.19	**-0.73**	**1**						
λ	**-0.67**	0.43	**0.70**	-0.12	0.47	**-0.52**	0.35	-0.38	**1**					
a	**-0.65**	0.50	0.41	0.31	0.36	**-0.70**	-0.15	-0.15	0.49	**1**				
V_{plasma}	-0.46	**0.67**	0.07	**0.64**	0.19	**-0.59**	-0.33	0.08	0.21	**0.71**	**1**			
κ	0.35	0.12	-0.40	0.33	-0.25	0.28	-0.12	0.24	-0.35	0.47	0.27	**1**		
δ_{lower}	-0.02	0.44	0.28	0.35	0.47	-0.02	0.04	-0.25	0.17	-0.04	0.09	0.19	**1**	
δ_{upper}	-0.28	**0.70**	0.32	**0.53**	0.50	-0.25	0.06	-0.28	0.34	0.25	0.47	0.30	**0.83**	**1**

*The strongest correlations (|correlation|>0.5) are indicated with bold face.

An estimated average electron temperature is calculated from the total plasma energy (W_{MHD}) as $\overline{T}_e = W_{MHD}/\left(3 \cdot \overline{n}_e \cdot V_{plasma}\right)$, where V_{plasma} stands for the plasma volume.

Pellet mass. High field side pellet injections are technically more challenging as the pellet has to be guided from the pellet injector placed on the outer side of the tokamak to the high field side. This results in a curved guiding tube, and consequently in a considerable pellet mass reduction depending on the pellet velocity. Due to the significant mass reduction in the guiding tube (figure 4-1) the nominal pellet mass cannot be used. Whereas due to the large scatter of the pellet mass at the end of the guiding tube, the nominal pellet mass multiplied by an average reduction factor – no matter how carefully determined – is also not sufficiently accurate for scaling studies where the variation of the variable is significant. This means that even if there are cavity and shadowgraphy measurements that provide good measurement of the local pellet mass along the injection line, they are useless unless they are positioned just before the entrance to the vacuum vessel. As this was not the case at AUG, two other methods were considered to estimate the actual pellet particle content reaching the plasma: a photodiode measuring the pellet's primarily D_α line emission (figure 4-2a) and the increase of the line averaged electron density from the DCN interferometry (figure 4-2b).

Figure 4-1 The transferred (i.e. the ratio between the final and nominal) pellet particle content as a function of the pellet velocity. The final pellet particle content is taken from the integration of the D_α measurement calibrated by density profile deconvolution. The average and the standard
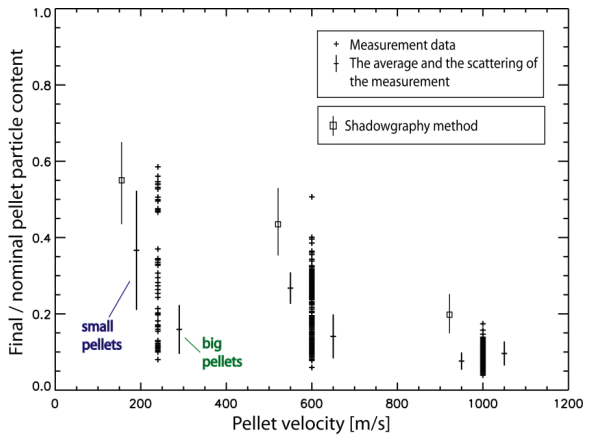
deviation of this ratio have been indicated along the measurement points, for the two nominal pellet particle contents used at ASDEX Upgrade, namely $1.4{\cdot}10^{20}$ and $3.8{\cdot}10^{20}$ which are denoted as small and big pellets on the figure. The results from the shadowgraphy analysis are taken from Lang et al. [64], i.e a dedicated study conducted for small pellets after the optimisation of the looping system.
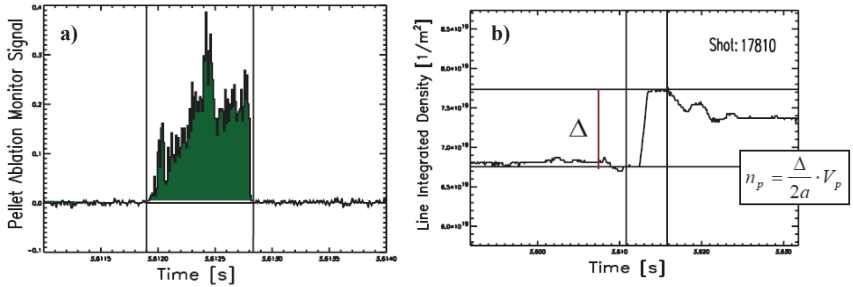
Figure 4-2 Pellet mass estimations: **a)** *from the integration of the ablation rate monitor, and* **b)** *from the increase of the plasma density (a-minor radius, V_p – plasma volume)*

In the first case, the D_α emission of the pellet is proportional to its ablation rate [74], thus integrating the D_α emission (i.e. light emission of the pellet) for the pellet's lifetime, a quantity proportional to the pellet mass can be obtained. Relative calibration for this method was carried out based on another set of discharges by density profile deconvolution using a DCN laser interferometer cross-checked by the Thomson scattering system[16] [64]. The second method considered was a simplified version of the calibration, i.e. a pellet particle content estimation from one line-of-sight of the DCN interferometer. This method was rejected later as a routine approach for the present investigations as it always underestimates the pellet mass due to the particle loss caused by the prompt ELM triggered by the pellet. In case of larger pellets this effect is however less pronounced and acceptable for calibration purposes. Following the IPADBASE convention the pellet mass is given in units of pellet particle content.

Pellet penetration depth. The pellet path can be separated into parallel and perpendicular components along the injection line. In this analysis deviation from the straight pellet path, i.e. acceleration in the perpendicular direction due inhomogeneous heating of the pellet [66] is neglected in the analysis. The penetration depth of the pellet is usually retrieved in two ways, using simple photodiode measurements (figure 4-3a) or sophisticated fast-framing camera systems (figure 4-3b). In case of AUG, both methods were analysed. For the single camera system automatic pellet recognition and pellet path acquisition algorithm had been developed, however time-integrated frames were only available for 81 pellet events from the 509.

---

[16] Thomson scattering system: plasma diagnostic providing electron temperature and density profiles.

The study thus focused on the photodiode signal – as mentioned before – ordinarily used to monitor pellet ablation by measuring the light emitted by the ablatant material of the deuterium pellet. The penetration depth is thus determined as the duration of the primarily D_α radiation times the velocity of the pellet assuming the pellet retains its parallel velocity (experimentally a good assumption). It strictly applies to pellet path parallel to the injection line [66], the penetration depth we were interested in anyhow.
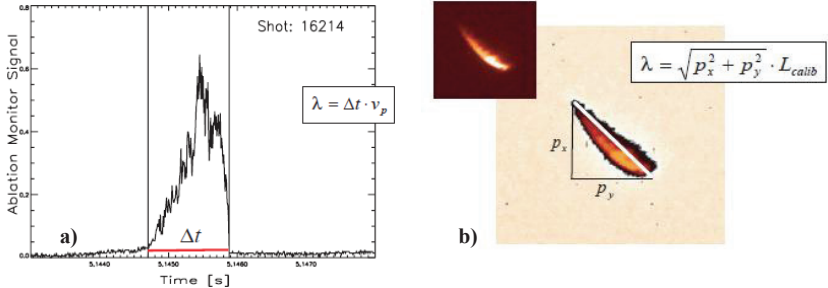
Figure 4-3 Pellet penetration depth determination: *a)* from the pellet ablation monitor signal and *b)* from the camera

4.2 High field side penetration depth scaling

The high field side penetration depth scaling was derived on the basis of the ASDEX Upgrade dataset I of the HFS-PAD database. Contrary to previous empirical penetration depth scalings with theory based variable selection (m_p, v_p, $T_{e,0}$, $n_{e,0}$), in this statistical approach, the penetration depth relevant parameters were determined through statistical model selection procedures using a scaling form derived with log-linear regression technique. For the statistical analysis IDL and SAS statistical libraries were used.

Model selection. Two statistical model selection methods, the forward selection (table 4-4) and backward elimination (table 4-5) had been applied to the dataset with the confidence level set to 95% assuming a power function form for the scaling following common approach.

Scaling form: $$Y = C \cdot \left(\prod_{i=1}^{p} X_i^{\alpha_i} \right) \cdot E \tag{4-1}$$

As possible candidates all parameters inside the database were considered except the heating schemes: namely the pellet parameters: pellet mass and the pellet velocity; the plasma parameters: average electron temperature and density, plasma current, toroidal magnetic field and the safety factor; and finally the geometrical factors: elongation, lower and upper

triangularity. Following the common approach, the penetration depth has been normalised to the minor radius of the tokamak, however the variation in this parameter is not sufficient to make an accurate scaling with the tokamak size possible.

Table 4-4. Forward selection algorithm applied to the ASDEX Upgrade dataset 1. In each step one variable with the highest statistical relevance is included (indicated by bold-face). The exponent(±standard deviation) and its statistical relevance (R) is indicated for each variable in each step as well as the RMSE of the scaling fit of the given step. The sixth step ends the procedure as the electron density values are below the pre-set value of Student t-distribution for confidence level of 95%.

Step	ln C	B_t	Te	m_p	v_p	κ	n_e	RMSE
1	0.60 (±0.06) R=9.55	-1.69 (±0.08) **R=21.93**						0.2328
2	0.21 (±0.06) R=3.58	-1.27 (±0.07) R=18.30	-0.63 (±0.04) **R=15.49**					0.1928
3	-0.37 (±0.07) R=5.06	-0.78 (±0.08) R=10.47	-0.72 (±0.04) R=19.38	0.16 (±0.01) **R=11.33**				0.1723
4	-0.65 (±0.08) R=7.74	-0.65 (±0.08) R=8.50	-0.75 (±0.04) R=20.62	0.25 (±0.02) R=12.30	0.16 (±0.03) **R=6.06**			0.1665
5	-1.37 (±0.19) R=7.36	-0.68 (±0.08) R=21.21	-0.80 (±0.04) R=21.21	0.26 (±0.02) R=13.03	0.17 (±0.03) R=6.37	1.38 (±0.32) **R=4.30**		0.1637
6	-1.43 (±0.18) R=7.74	-0.76 (±0.08) R=9.85	-0.96 (±0.06) R=17.23	0.25 (±0.02) R=12.29	0.15 (±0.03) R=6.00	2.32 (±0.40) R=5.76	[-0.19] [(±0.05)] [R=3.77]	0.1616

Empirical scalings are often expressed in the form of power functions where it is assumed that the underlying model is linear in the regression parameters as well as in the logarithm of the regression variables. In order to investigate this assumption for our case, the deviation from linearity has been studied for each parameter and a significant deviation has been found for the pellet velocity as shown later in figure 4-6. As the pellet velocity dependence is clearly nonlinear, a quadratic term of the pellet velocity on logarithmic scale has been included. On the ordinary scale that means that $\lambda \sim v_p^{\alpha + \beta \cdot \ln v_p}$. For simplicity, the pellet velocity has been arbitrarily divided by 420 m/s to obtain easily interpretable regression coefficients when a quadratic term is included ($\tilde{v}_p = v_p / 420\,\text{m/s}$).

Table 4-5. *Backward elimination algorithm applied to the ASDEX Upgrade dataset I. In each step one variable with the lowest statistical relevance is excluded from the scaling (indicated by bold-face). The exponent(±standard deviation) and its statistical relevance (R) is indicated for each variable in each step as well as the RMSE of the scaling fit of the given step. The procedure ended as all the remaining variables pass the Student t-test at the pre-defined level with confidence level of 95%.*

Step	1	2	3	4	5	6
$\ln C$	-1.23 (±0.25) R=5.00	-1.22 (±0.25) R=4.99	-1.22 (±0.25) R=4.96	-1.07 (±0.23) R=4.66	-1.43 (±0.18) R=7.74	-1.37 (±0.19) R=7.36
$\underline{m_p}$	0.25 (±0.02) R=11.32	0.25 (±0.02) R=11.58	0.24 (±0.02) R=11.47	0.25 (±0.02) R=12.43	0.25 (±0.02) R=12.29	0.26 (±0.02) R=13.03
$\underline{v_p}$	0.16 (±0.03) R=5.43	0.16 (±0.03) R=5.42	0.15 (±0.03) R=5.17	0.16 (±0.03) R=6.32	0.15 (±0.03) R=6.00	0.17 (±0.03) R=6.37
$\underline{T_e}$	-0.96 (±0.07) R=13.38	-0.95 (±0.07) R=13.39	-0.95 (±0.07) R=13.35	-1.02 (±0.06) R=16.90	-0.96 (±0.06) R=17.23	-0.80 (±0.04) R=21.21
n_e	-0.21 (±0.08) R=2.50	-0.22 (±0.08) R=2.80	-0.17 (±0.07) R=2.37	-0.26 (±0.06) R=4.57	-0.19 (±0.05) **R=3.77**	
$\underline{B_t}$	-1.14 (±0.21) R=5.34	-1.09 (±0.19) R=5.74	-0.87 (±0.13) R=6.70	-0.70 (±0.08) R=8.74	-0.76 (±0.08) R=9.85	-0.68 (±0.08) R=9.08
I_p	0.31 (±0.19) R=1.64	0.27 (±0.17) **R=1.59**				
q_{95}	0.53 (±0.23) R=2.30	0.48 (±0.21) R=2.33	0.25 (±0.15) **R=1.70**			
$\underline{\kappa}$	1.85 (±0.47) R=3.90	1.81 (±0.47) R=3.88	1.92 (±0.46) R=4.17	2.31 (±0.40) R=5.75	2.32 (±0.40) R=5.76	1.38 (±0.32) R=4.30
δ_{lower}	0.34 (±0.16) R=2.04	0.27 (±0.1) R=2.70	0.28 (±0.10) R=2.76	0.26 (±0.10) **R=2.57**		
$1+\delta_{upper}$	-0.14 (±0.29) **R=0.49**					
RMSE	0.1603	0.1601	0.1604	0.1607	0.1616	0.1637

Both methods described above yielded the same result, i.e. the statistically significant parameters in an HFS penetration depth scaling are: the pellet mass and velocity (both first

and second order terms), average electron temperature, toroidal magnetic field and the plasma elongation. The estimated form of the HFS penetration depth scaling law was found to be:

$$\lambda/a = C \cdot m_p^{\alpha_1} \cdot \tilde{v}_p^{\alpha_2 + \alpha_3 \cdot \ln \tilde{v}_p} \cdot \overline{T}_e^{\alpha_4} \cdot B_t^{\alpha_5} \cdot \kappa^{\alpha_6} \tag{4-2}$$

The logarithm of the above given scaling form has been fitted to the dataset using an ordinary least square fit (OLS) algorithm [68], utilizing the fact that the model is still linear in the logarithm of the regression parameters and assuming a relative measurement error of 15% for the penetration depth and not any errors in the regression variables. The goodness of the fit is shown in figure 4-4 and is expressed by a root-mean-square-error (RMSE) value of 16 %. The results are collected in table 4-6, where, besides the exponent and error of each regression variable, their statistical significance and relevance are also indicated. The error indicates one estimated standard deviation of the estimated exponents.

Table 4-6 *HFS penetration depth scaling results. (Scaling constant: C=0.25+/-0.04)*

	m_p	$v_p^{I.}$	$v_p^{II.}$	$\overline{T}_e$	B_t	κ
Exponent	**0.22**	**0.24**	**-0.34**	**-0.67**	**-0.41**	**1.28**
Standard deviation	0.02	0.03	0.05	0.04	0.08	0.31
Stat. significance	11.11	8.87	6.89	16.52	4.96	4.14
Stat. relevance	0.68			1.11	0.17	0.36
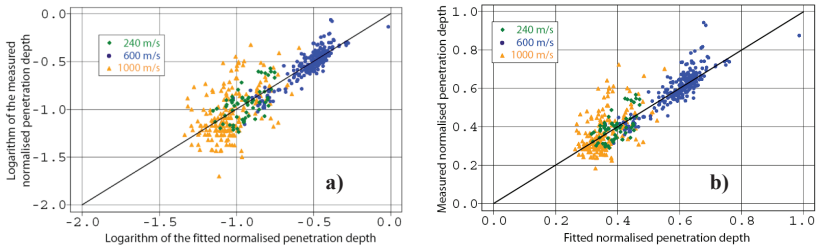
Figure 4-4 *Comparison of the normalised penetration depth with the HFS scaling on the **a)** logarithmic and **b)** ordinary scale.*

The usual limitation of the ordinary least square procedure is that it assumes that only the response variable, i.e. the normalised penetration depth in our case, and none of the regression variables are measured with an error. In reality the estimates of the measurement

errors in the plasma parameters, as taken from [75], are 1.1% (a), 12% ($\overline{T}_e$), 1% (B_t) and 4% (κ). The measurement error in the pellet velocity is about 0.25% [64], in the pellet mass approximately 20% (estimated based on the calibration method). A graphical version of the errors-in-variables technique has been applied to address the effect of measurement errors in a simplified way, the largest being the errors of the average electron temperature and the pellet mass. Specifically the reduced residuals were plotted against the studied variable, both scaled with their respective measurement errors to make the size of the errors on both axes the same. The reduced residuals correspond to the ratio of the normalised penetration depth to the power-law scaling, while omitting, the variable being investigated. The slope of the main axis of a 95% prediction ellipse fitted to the data is obtained and rescaled to provide an estimate of the actual exponent that takes the measurement error of the variable into account. In our case the exponent of the pellet mass decreased to 0.3 well within one standard deviation. The exponent of the average electron temperature decreased to - 0.78, though still retaining its leading role in the ablation process. This means that to improve our scaling, more precise measurement of the electron temperature (profiles), pellet mass and penetration measurements would be required.
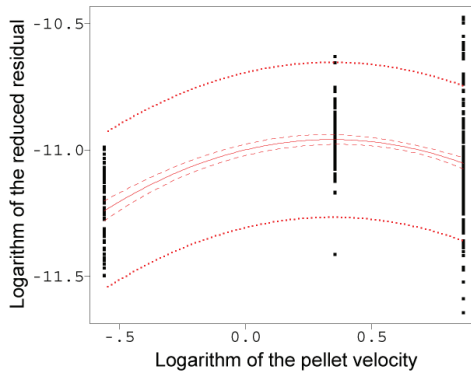
Figure 4-5 *Reduced residual plot regarding the pellet velocity.*

The pellet velocity dependence has been explored in detail and the nonlinearity is illustrated by the reduced residual plot on a logarithmic scale in figure 4-5. In the figure the solid curve corresponds to the least-square fit to the reduced residuals that in our case take the following form based on the obtained scaling:

$$\frac{\lambda / a}{C \cdot m_p^{0.22} \cdot T_e^{-0.67} \cdot B_t^{-0.41} \cdot \kappa^{1.28}} \qquad (4\text{-}3)$$

Two bands are plotted: the outer band (dotted line) represents a 95% local prediction band of the response variable, and the inner band (dashed line) a 95% local confidence band for its mean. In the former case, the 'scatter' (i.e. 2 standard deviations) of the individual points is effectively 'added' to the uncertainty of the mean.

The statistical reasons have been explored based on the correlation matrix shown in table 4-3 and correlation with other parameters was found insufficient to produce this effect. The 95% prediction band and mean indicate that there is a definite deviation from linearity, though not necessarily to this extent. Although the reason for this extent is still unclear the large scatter in the case of the 1000 m/s velocities may indicate the following effect. The fastest (1000 m/s) pellets are subject to the extreme conditions in the HFS pellet guiding tube. Therefore, the pellet ice quality may be significantly reduced and the broken parts of the pellet arriving together with the pellet may introduce a systematic error into the pellet mass and penetration depth determination, i.e. in the D_α light emission.

4.3 Comparison with present experimental and theoretical scalings

To put the obtained empirical penetration depth scaling into perspective, its relation is examined to the existing empirical and theoretical models. Being the first of its kind regarding HFS pellet injections (due to the scarce availability of HFS pellet data at other devices for proper scaling analysis), the obtained scaling is compared to the empirical LFS penetration depth scaling derived based on IPADBASE, it being the largest existing multi-machine LFS pellet ablation database. Both the scaling obtained on the whole LFS database and the scaling restricted to the AUG subset (with LFS injection carried out along the midplane) is included in the comparison. In the case of the IPADBASE LFS penetration-depth scalings, the regression parameters have been chosen a priori to be the pellet mass, velocity, central electron temperature and density. This was based on the assumption that these parameters are the most likely ones to be involved in the ablation process according to theoretical considerations of the NGS model.

The two theoretical models included in the analysis were the NGS model and the Hybrid ablation code. The NGS model had been chosen despite its simplicity including only the neutral gas shielding of the pellet as it is still widely used and satisfactorily reproduces pellet penetrations depths to a given degree for a large range of pellet and plasma parameters. For a more recent and sophisticated model the Hybrid ablation code had been chosen

incorporating both gas dynamic shielding due to the neutral and ionized part of the cloud and the electrostatic shielding. Whereas in case of the NGS model the ablation rate can be derived in a closed form analytically (Eq. 2-9), to obtain a pertinent scaling for the numerical Hybrid code systematic parameter scans were performed for a variety of input parameters (electron temperature and density, pellet mass and velocity) summarized in table 4-7. The complete factorial design of the dataset is reflected in the null correlation of the input parameters shown in table 4-8.

Table 4-7 Description of the simulated ablation rate dataset of the Hybrid ablation code.

Variables	Symbol	Unit	Range	Exact values
pellet radius	r_p	mm	0.4-1.0	0.4, 0.6, 0.8, 1.0
pellet velocity	v_p	m/s	200-5000	200, 400, 600, 800, 1000, 5000
electron density	n_e	10^{19} m^{-3}	0.5-8.0	0.5, 1, 2, 4, 8
electron temperature	T_e	keV	0.2-3.2	0.2, 0.4, 0.8, 1.6, 3.2

Table 4-8 Correlation matrix of the simulated ablation rate dataset of the Hybrid ablation code

Corr.	r_p	v_p	n_e	T_e	dN/dt
r_p	1				
v_p	0	1			
n_e	0	0	1		
T_e	0	0	0	1	
dN/dt	0.199	0.062	0.258	0.791	1

The NGS model gives the dependence of the ablation rate on the local electron temperature, density and pellet mass while in the Hybrid ablation code the pellet velocity is also included:

Theoretical ablation rate scaling: $\quad \dot{N} = C \cdot m_p^{\alpha} \cdot v_p^{\beta} \cdot T_e^{\gamma} \cdot n_e^{\delta}$ (4-4)

Multi-linear regression using this common scaling form has then been applied to the obtained dataset of simulated Hybrid ablation rates (figure 4-6). The ablation rate scalings of the NGS model and Hybrid ablation code including the results of the regression analysis is summarized in table 4-9.

Table 4-9 Theoretical ablation rate scalings: NGS model and Hybrid ablation code

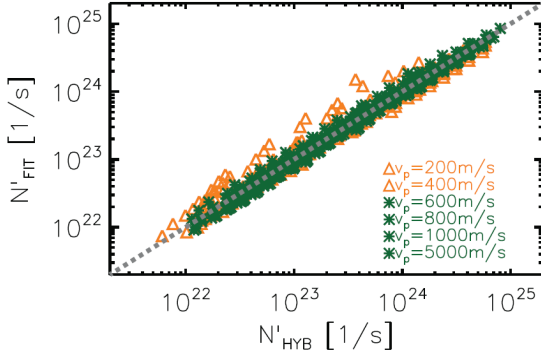| Model:	Scaling type	m_p	v_p	T_e	n_e
NGS model	ablation rate	0.45	-	1.64	0.33
Hybrid model	ablation rate	0.34	0.18	1.58	0.42

Figure 4-6 *Multi-linear regression on the simulation dataset of the Hybrid ablation code.*

In order to compare theoretical scaling with that of the HFS database, the ablation rate scaling had to be transformed into a penetration depth scaling by integrating the differential equation of the pellet radius reduction for the pellet's lifetime using electron temperature and density profiles. Based on common ablation theories, the instantaneous pellet radius change can be approximated by

$$\frac{dr_p}{dt} = C \cdot n_{e(r)}^{\alpha} \cdot T_{e(r)}^{\beta} \cdot v_p^{\gamma} \cdot r_p^{\delta} \tag{4-5}$$

whereby the theories differ in the inclusion of the pellet velocity and the given exponents. The radial scales are normalized to the minor radius (a) giving $\hat{x} = 1 - r/a$ the normalized distance along the pellet path (r being the plasma radius) and $\hat{\lambda} = \lambda/a$ the normalized penetration depth. If the pellet velocity is assumed to be unchanged during the ablation process, then $dt = (-a \cdot d\hat{x})/v_p$ and the equation can be integrated over the pellet's lifetime

$$\int_{r_p}^{0} r_p^{-\delta} \, dr_p = C \cdot v_p^{\gamma} \int n_e^{\alpha} \cdot T_e^{\beta} \, dt \quad \Rightarrow \quad \frac{-r_p^{1-\delta}}{1-\delta} = -C \cdot v_p^{\gamma-1} \cdot a \int_0^{\hat{\lambda}} n_{e(\hat{x})}^{\alpha} \cdot T_{e(\hat{x})}^{\beta} \, d\hat{x} \tag{4-6,4-7}$$

If the temperature and density profiles are known, the integral can be evaluated to calculate the theoretical penetration depth. To derive the theoretical penetration depth scaling analytically, the simplest approximation is a linear electron temperature and electron density profile in the form of $T_e(r) = T_{e,0} \cdot (1 - r/a)$ and $n_e(r) = n_{e,0} \cdot (1 - r/a)$ respectively, where $T_{e,0}$ and $n_{e,0}$ denote the central electron temperature and central electron density. In this case the theoretical penetration depth is given in the form

$$\hat{\lambda} = \frac{\lambda}{a} = \left(\frac{\alpha+\beta+1}{C(1-\delta)\cdot a}\right)^{1/(\alpha+\beta+1)} \cdot n_{e,0}^{\frac{-\alpha}{\alpha+\beta+1}} \cdot T_{e,0}^{\frac{-\beta}{\alpha+\beta+1}} \cdot r_p^{\frac{1-\gamma}{\alpha+\beta+1}} \cdot v_p^{\frac{\delta-1}{\alpha+\beta+1}} \qquad (4\text{-}8)$$

By refining the approximation by a better description of the edge regions, e.g. by including a separate linear term for the edge and the bulk region, it becomes clear firstly that the pedestal region plays an important role, thus the linear approximation of the electron temperature and density profile is not suitable [76]. Furthermore the transformation of the ablation rate power scaling into an appropriate penetration scaling in a form of a power function is analytically not possible. Therefore, for the proper description of the profiles, a typical ASDEX Upgrade type-I ELMy H-mode electron temperature and electron density profile shape (#20043, $\bar{T}_e$ =1.4 keV, $T_{e,0}$=3.1keV, $\bar{n}_e$=6.7·10^{19} m^{-3}, $n_{e,0}$=7·10^{19} m^{-3}) mapped to the straight HFS pellet trajectory has been selected (both profiles are shown on figure 4-7).
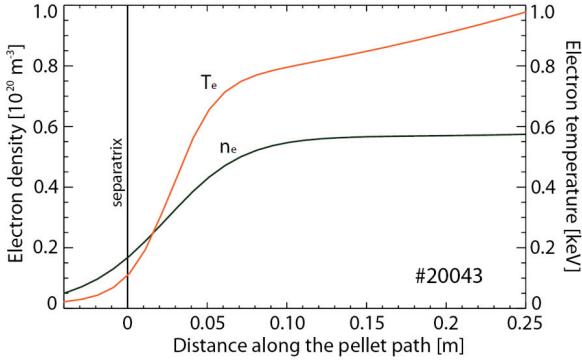
Figure 4-7 *Electron temperature and electron density profile of a typical H-mode ASDEX Upgrade discharge (fitted to discharge #20043).*

The penetration depth was then calculated numerically varying the input parameters (m_p, v_p, $T_{e,0}$, $n_{e,0}$) covering appropriate ranges using the selected temperature and density profiles. Using linear regression analysis the exponents of the penetration depth scaling were calculated for both theoretical models. The results of both transformations are summarised in table 4-10, with the theoretical penetration depth scalings having the following form (with the minor radius becoming an additional regression parameter in the linear profile case):

$$\lambda = C \cdot m_p^{\beta_1} \cdot v_p^{\beta_2} \cdot T_e^{\beta_3} \cdot n_e^{\beta_4} \cdot (a^{\beta_5}). \qquad (4\text{-}9)$$

This form has also been applied to the HFS database by conducting a simple regression for better comparison.

Table 4-10 *Transformation of the theoretical ablation rate scalings to the corresponding penetration depth scaling using a linear and typical AUG profiles mapped to the HFS pellet path respectively.*

Model:	Scaling type	Profile type	m_p	v_p	T_e	n_e	a
NGS model	ablation rate		0.45	-	1.64	0.33	-
	penetration depth	linear profile	0.19	0.34	-0.55	-0.11	0.66
	Penetration depth	**AUG profile**	**0.30**	**0.49**	**-0.71**	**-0.15**	**-**
Hybrid model	ablation rate		0.34	0.18	1.58	0.42	-
	penetration depth	linear profile	0.22	0.27	-0.53	-0.14	0.67
	Penetration depth	**AUG profile**	**0.35**	**0.41**	**-0.69**	**-0.18**	**-**

The linear profile is often used in the literature [14,77] based on the work of Büchl et al [76], and Milora et al [54] who also discuss the effect of different profile shapes. It should however be noted that as shown in table 4-10, in case of the ASDEX Upgrade device the difference between the transformations regarding the linear and the typical experimental profile is about a factor of two in the exponents. In the following, results regarding the typical AUG profile will be used.

The pellet penetration depth scalings used for comparison have a different form than the obtained HFS scaling. As already mentioned in our case, the aim is to put the derived empirical scaling into context with theory and other experiments, and not to validate any of the ablation models. In the table 4-11 the exponents are displayed of the variables occurring in the two theoretical and three empirical scalings respectively. In here obtained scalings the standard deviations and for the main HFS and LFS scalings the statistical relevancies are also indicated. It should be mentioned that in case of the two theoretical scalings the exponent of the electron temperature and density are the same whether central values or average values are used. The difference is in the value of the regression constant. In case of using central values, the constants would change to $C_{NGS}=0.033$ and $C_{Hybrid}=0.054$ respectively. For the velocity, the three columns are defined as follows: v_p^L is the velocity exponent in the linear case (this applies to Scalings 1,2,4,5); $v_p^{II.a}$ and $v_p^{II.b}$ is the first and second order term in the case of the quadratic dependence on the logarithmic scale (HFS scaling), i.e. the values α_2 and α_3 in (Eq. 4-2) respectively. Please note that the respective dimensions of the parameters are stated in table 4-2, except for the logarithmic quadratic case where the pellet velocity is normalised to 420 m/s.

Table 4-11 *Comparison of the derived HFS penetration-depth scaling to the theoretical models and the present LFS scaling for the ASDEX Upgrade tokamak.*

No.	Exponents	C	m_p	$v_p^{I.}$	$\tilde{v}_p^{II.a}$	$\tilde{v}_p^{II.b}$	$T_{e,0}$	$\overline{T}_e$	$n_{e,0}$	π_e	B_t	κ
1	NGS Model	0.018	0.30	0.49				-0.71		-0.15		
2	Hybrid Code	0.031	0.35	0.41				-0.69		-0.18		
3	**HFS Scaling**	**0.25**	**0.22**		**0.24**	**-0.34**		**-0.67**			**-0.41**	**1.28**
	(Std. dev.)	(0.04)	(0.02)		(0.03)	(0.05)		(0.04)			(0.08)	(0.31)
	Stat. relevance		0.68					1.11			0.17	0.36
4	HFS simple reg.	0.06	0.35	0.23				-0.86		0.03		
	(Std. dev.)	(0.01)	(0.02)	(0.03)				(0.05)		(0.04)		
5	LFS Scaling	0.15	0.06	0.18			-0.41		0.07			
	Stat. relevance		(0.06)	(0.29)			(1.08)		(0.05)			

From table 4-11 it can be concluded that by comparing the exponents of the two theoretical scalings with those of the HFS scaling the tendencies generally agree, even though the values lie considerably outside the two standard deviation range. The simple regression based on the normalised form of Eq. 4-9 (Scaling 4) has been conducted on the HFS database to facilitate the comparison with the two theoretical scalings. It is worthwhile to study the table carefully. The following points can be made.

The pellet mass and electron temperature exponents of Scaling 4 are very similar to the theoretical ones and different from the LFS scaling. The inclusion of the two additional (statistically significant) variables, i.e. the toroidal magnetic field and the elongation, and possibly the changed form of the pellet velocity dependence lead to the lower pellet mass and less pronounced electron temperature dependence in the HFS scaling compared to Scalings 1,2 and 4.

The exponent of the pellet velocity for Scaling 4 is about half of the two theoretical exponents and is very close to the coefficients of the log-linear term in Scaling 3 and is slightly larger than in the LFS scaling. Note, that at the present, the theoretical exponents are considerably larger than those of the three experimental scalings.

Scaling 4 indicates that the electron density is not statistically significant, thus it supports its exclusion in Scaling 3 by the semi-automatic selection procedure. The theoretical exponents (-0.15 and -0.18) are in clear contradiction with the data since they are 5 standard deviations away from the experimental exponents (Scaling 4 and 5). A negligible role of the electron density was also indicated by the IPADBASE scalings (table 2-2), even though in case of the JET and DIII-D scaling the density exponents were somewhat larger than zero but in the opposite direction (-0.3 and 0.23 respectively).

The RMSE of Scaling 3 is 15.7% compared to 17.8% for Scaling 4. This is in agreement with the statistical significance of the three additional terms (B_t, κ, new form for v_p).

Concerning the two new statistically significant variables, their role can be assessed based on the magnitude of the exponent and their expected change in future experiments. The fact is that due to the optimal magnetic geometry the value of the elongation will probably not change significantly and therefore plays no significant role. Contrary to this, the magnetic field values will change considerably – will approximately double its value in ITER to 5.3 T with respect to the standard 2.5T of AUG – and thus may play a more decisive role in the future and needs further exploration for proper extrapolation.

4.4 Magnetic field dependence

Although not included in previous scalings (LFS and the two theoretical scalings), the magnetic field may still be of great importance in the ablation process through the following considerations. First, the ablation rate and therefore the penetration depth as well certainly depend on the cross-field extent of the cloud. The cross-field expansion of the pellet cloud is stopped when ionization sets in at the cloud periphery. How fast this trapping of the cloud occurs depends on the cloud parameters as well as the strength of the magnetic field determining the cross-field extent of the cloud. A stronger compression of the pellet cloud would however (through higher shielding, thus lower ablation rate) result in a slightly positive magnetic field dependence in contrary to the statistical result. On the other hand, the drift effects transporting the ablatant material inward, i.e. toward the plasma center also depend on the gradient strength of the magnetic field.

In order to study the magnitude and direction of the magnetic field effect, dedicated experiments have been planned and carried out at AUG. The aim was to provide a single parameter scan for the magnetic field and electron temperature, the foremost penetration depth dependence. Four ELMy H-mode Deuterium discharges were executed at three different magnetic field values spanning the AUG parameter range (B_t=1.8, 2.5, 3T). The NBI heating power was increased in a stepwise fashion (P_{NBI}=2.5, 5, 7.5, 10 MW) to achieve a suitable variation in the electron temperature (T_{ped}=0.26-0.79keV) as well. The velocity and initial mass of the 30 injected Deuterium pellet were kept the same, i.e. v_p=600m/s and nominal pellet particle content of $3.8 \cdot 10^{20}$ particles were used. The discharges were tailored to be as similar as possible in feed-forward mode, thereby also keeping 2 out of the 5 independent variables of the empirical HFS penetration depth scaling nearly constant (κ, v_p).

In case of the pellet mass, the variation due to the mass reduction of 15(±7)% caused by the transfer through the guiding tube was not enough to determine the pellet mass dependence based on this limited dataset. For the remaining two dependent variables, the scaling had been obtained by ordinary least mean squares regression shown in Table 4-12.

Table 4-12 *Magnetic field dependence and electron temperature dependence of the penetration depth from the dedicated single parameter scan experiments: $\lambda \sim \bar{T}_e^{\alpha_4} \cdot B_t^{\alpha_5}$. The errors denote ±1 standard deviations.*

	T_e	B_t
Statistical scaling	-0.67 (±0.04)	-0.41 (±0.08)
Dedicated scan	-0.57 (±0.08)	-0.63 (±0.02)

The comparison of the statistical and dedicated discharges shows a reasonable agreement for the electron temperature. The direction of the magnetic field dependences agree, although there exists some difference between the experimental exponents. To illustrate the effect of the magnetic field, reduced residuals are used in figure 4-8 to eliminate the influence of m_p and T_e by normalizing the penetration depth to these dominant dependences as shown in the figure.
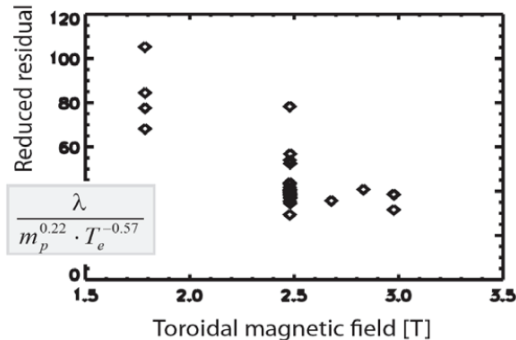
Figure 4-8 *Magnetic field dependence from the dedicated single parameter scan experiments.*

Theoretical investigations of the role of the magnetic field have then been carried out with the Hybrid ablation code in two steps. In the first case, linear scans have been conducted on the electron temperature (T_{ped} = 0.26-0.79 keV based on the standard T_e and n_e profile shapes from combined, standard diagnostics of #20043) and magnetic field (B_t = 1.8-3 T)

parameter regime of the dedicated experiments using the simulation code for 600 m/s large pellets ($3.8 \cdot 10^{20}$ nominal particles). The dedicated runs performed by B. Lovász and K. Gál shown in figure 4-10 show a slight positive dependence on the magnetic field that is in disagreement - even regarding its sign - to the negative magnetic field dependence of the empirical results shown earlier.
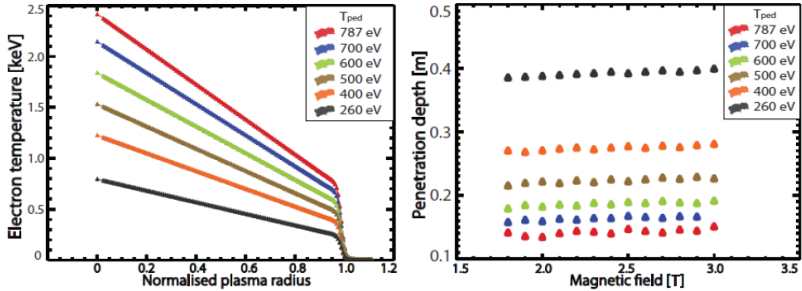
Figure 4-10 *Penetration depths derived by the Hybrid pellet ablation code for the magnetic field range of AUG for different electron temperature profiles.*
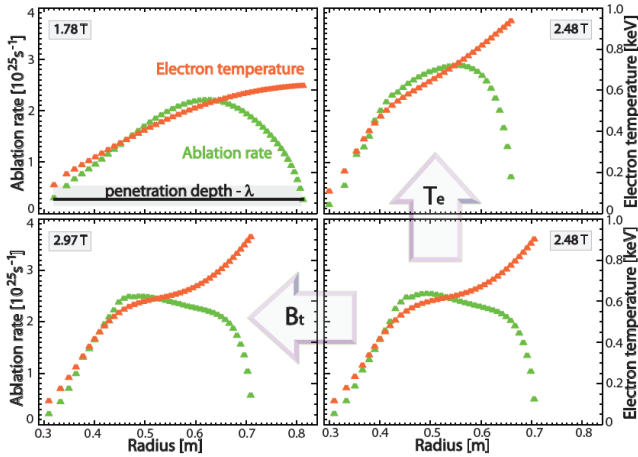
Figure 4-12 *Electron temperature profiles and corresponding Hybrid ablation code simulations for the dedicated magnetic field scan.*

The second step focused on the simulation of the dedicated single parameter scan pellets. Four cases with three different magnetic field values have been highlighted in figure

75

4-11 which shows the experimental electron temperature profiles and the simulated pellet ablation profiles, whereas table 4-13 the corresponding simulated and measured penetration depth values. To decouple the magnetic field and the electron temperature effect, two pairs have been selected where one is kept approximately the same, whereas the other parameter is changed, showing that whereas the increase of T_e (b->c) results in a distinguishable decrease of the penetration depth, the increase of B_t (c->d) however is not captured by the Hybrid code.

No.	B_t	λ Hybrid	λ measured
a)	1.78	0.492	0.538
b)	2.48	0.359	0.399
c)	2.48	0.395	0.402
d)	2.97	0.399	0.364

Table 4-13 *The simulated and measured penetration depth values for the dedicated magnetic field scan.*

4.5 Discussion and considerations for ITER

As mentioned before the presently planned ITER fuelling setup comprises two HFS pellet injection systems providing fuelling by pellets (hydrogen, deuterium, tritium and deuterium-tritium mixture) with pellet masses limited by the maximal affordable density perturbation (less than 10% corresponding to a pellet particle content of about $5.4 \cdot 10^{21}$ and 92 mm^3 pellet size) and pellet velocities of 300 m/s (up to 500 m/s) that are considered necessary to achieve penetration beyond the supposed ELM-affected zone (~15% of the minor radius).

In order to apply the derived HFS penetration depth scaling to the presently foreseen ITER scenario, first the question of the scaling of the penetration depth with the tokamak size has to be addressed. The common approach to normalize the penetration depth is to the minor radius for a direct size scaling. To my knowledge, the scaling of the pellet-penetration depth with tokamak size has not yet been fully investigated in a statistical context. In this case the effect of the normalisation of the penetration depth to the minor radius has been addressed in the following way. The exclusion of the normalisation factor (i.e. regressing with λ instead of λ/a) yields the same estimated exponents well within one standard deviation. Including the minor radius as an additional regression variable yields the same result with a minor radius exponent of 0.13 (+/-0.88) and a statistical significance of 0.14. That means that the minor radius with a little variation ($a = 0.48$-0.54) is not strongly correlated with the other regression parameters. However, the small variation also implies that based on the present single-

machine dataset, the penetration depth scaling with size cannot be resolved. For this purpose, of course, further analysis of a multi-machine dataset (including differently sized tokamaks) is required. Nonetheless, by assuming that the size scaling with the tokamak lies within λ and λ/a, an approximate range of predicted pellet penetration can be obtained for ITER. The proposed pellet velocities for ITER lie in the pellet velocity range where the dependence is still linear for ASDEX Upgrade. Therefore, for these predictions the slope of the linear segment (an exponent of 0.24) is used.

For the operational scenario of the ITER FDR (1998) Design ($\overline{T}_e \sim$ 12.9 keV, B_t = 5.68T, κ_{sep}=1.73, a=2.80 m) described in the ITER Technical Basis [78] the regression with respect to λ and λ/a yield a penetration depth range of 2.5–16% of the minor radius and 2.8-19% with respect to the maximum velocity of 500 m/s. Mainly due to lower average electron temperature and larger elongation of the plasma, in case of the ITER FEAT (2003) Design ($\overline{T}_e$ = 8 keV, B_t=5.3 T, κ_{sep}=1.85, a=2.0 m) described in *Mukhovatov et al.* [79] and the ITER Physics Basis Update [77] the predicted pellet penetration increases to 5-25% of the minor radius and to 6-29% regarding the maximum pellet velocity. In both cases the injected pellet may cross the supposed ELM-affected zone (15% of the minor radius), however the penetration scaling with the tokamak size clearly has to be resolved by extending the HFS database with data from other machines before more reliable predictions can be made. To conduct such a multi-machine analysis, the effect of the injection angle on the penetration depth scaling has to be resolved as well.

It should be pointed out that for fuelling in case of ITER penetration to the top of the pedestal is required. Therefore in ITER, the pedestal region will play, compared to the present day tokamaks, an even more important role in the ablation process. In future scalings, the pedestal electron temperature would be a good regression variable to improve the physical relevance of the presented scaling. On the other hand for ELM triggering studies the linear profile assumption might be sufficient to predict penetration of pellets only outside the top of the pedestal. This means that the scalings based on experiments on present-day machines are valuable for predicting the ELM triggering potential of pellets.

Finally the obtained empirical penetration depth scaling derived through statistical analysis indicated a strong magnetic field dependence of -0.41 ($\pm$0.08), a regression parameter not yet included in present theoretical scalings and verified by the dedicated single parameters scan experiments conducted at AUG. Although the exponent have not been quantitatively reproduced, it supported the relevant role of the magnetic field in pellet penetration with an

exponent of -0.63 (±0.08), thus matching the importance and direction of dependence. At present there is no full theoretical understanding of this phenomena and the Hybrid ablation code also cannot describe the empirical findings showing slight positive dependences. Resulting in possibly significant overestimation of the penetration depth, this discrepancy is worthwhile to be investigated further, especially in the view of higher magnetic fields of future tokamaks such as ITER and perhaps DEMO.

Chapter 5

Result II.

High Density H-mode

In the last two years (2001-2002) of W7-AS, that is from the discovery of the HDH mode until the shut-down, extensive studies have been conducted involving dedicated global parameter scans to find the mechanism responsible for the remarkably low impurity concentration. The mechanism, nonetheless, had not been found. The empirical model established on the experimental result at that time predicted the additional transport mechanism to reside in the plasma edge causing enhanced impurity diffusion in the steep gradient region of the electron temperature and density profiles [53].

The aim of this chapter is first to find and characterize phenomena in the electron density fluctuations measured by the Lithium Beam Emission Spectroscopy (Li-BES) and in the magnetic fluctuations measured by Mirnov coil arrays. Secondly their possible relation to impurity transport is investigated and the results are compared to other devices. It has to be emphasized that this analysis was done well after the closure of the W7-AS experiment. This way, there was no possibility to perform new measurements, only existing data could be analyzed. On the other hand, the obtained information will be important for the design of experiments on the Wendelstein 7-X device to be started in 2014.

5.1 Density fluctuations - Lithium Beam Spectroscopy studies

In case of high densities in the range of 10^{20} m^{-3} characteristic for HDH phases, density fluctuations can only be studied up to about 1 cm inside the separatrix using Li-BES. The autocorrelation function of these density fluctuations mainly features triangle- and peak-like properties, thus to separate the two phenomena and obtain their characteristics a

combination of a Gaussian and two-sided linear function had been fitted to the respective autocorrelation functions.
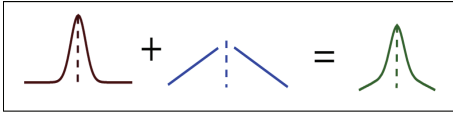
Figure 5-1 The autocorrelation functions are fitted with a combination of a Gaussian and a two-sided linear function.

In order to have a variety of discharges at our disposal, five experimental days with high resolution Li-BES data have been selected for inclusion in the study. The specific experimental days and their main program are shown in tTable 5-1.

Table 5-1 Experimental days included in the analysis and their main program

Date	Main Program
13.03.2002	Transition from H-mode to HDH mode
18.03.2002	High β Program
20.03.2002	High β Program
	Divertor Program, Density Scan
22.03.2002	Fluctuation in Divertor Configuration
	Density Limit with 1.8T and 4 NBI
10.04.2002	HDH-mode
	Laser Ablation
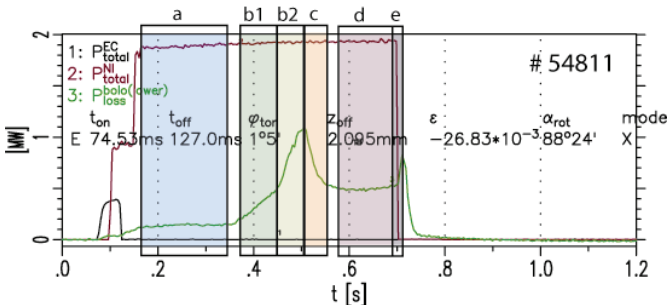
Figure 5-2 An HDH discharge sliced into appropriate time intervals

All discharges with sound plasma parameters and Li-beam signals were sliced into appropriate time intervals depending on their impurity radiation behaviour.

Figure 5-2 shows the time evolution of the impurity radiation (colour green), NBI heating power (red) and ECRH heating power (black). The selected time intervals are shaded with different colours and are characterized by letters from *a* to *e* as follows:

a. start   – stable period at the beginning of the discharge
b. up   – increasing impurity radiation
c. down – decreasing impurity radiation
d. middle – stable impurity radiation (possible HDH phases)
e. end   – transition out of the stable phase

In a given discharge, phases with the impurity radiation increasing/decreasing at a different rate are collected as separate intervals just like the two intervals with increasing radiation denoted b1 and b2 in figure 5-2. Possible HDH phases, denoted 'middle' phases out of the collected 226 time slices were checked for their energy confinement time (estimated as $\tau_E \sim W_{dia}/P_{tot}$, where W_{dia} is the diamagnetic energy of the plasma and P_{tot} the total heating power) and average electron density values to identify HDH phases. Phases with stable impurity radiation, above a given critical density threshold ($n_e^{th} \sim 0.8 \cdot 10^{20}$ m^{-3}) that had high estimated energy confinement time were regarded as HDH phases (51 phases in 40 discharges), whereas phases showing HDH-similar characteristics, i.e. phases with stable impurity radiation but below the density threshold were labelled non-HDH phases (22 phases in 16 discharges) and collected for comparison.

Comparing the starting, unstable ELM-free and HDH phases the following typical behaviour has been observed. The peak-like structure is present in all three phases, whereas the triangle-like phenomenon disappears in the HDH phase. As an example time evolution of a HDH discharge with the three phases in a single discharge is shown in figure 5-3 and the corresponding auto-correlation function (raw and fitted) is shown in figure 5-4. The maximal background contribution is 10^{-4}, $5 \cdot 10^{-5}$ and $5 \cdot 10^{-5}$ respectively (the area below this level is shaded on the figures).
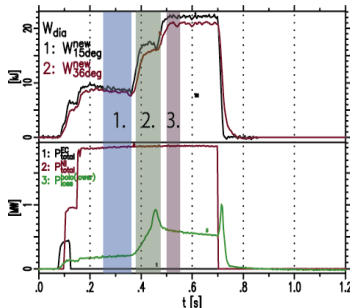
Figure 5-3 *Time evolution of the diamagnetic energy, additional heating powers (NBI and ECRH) as well as the impurity radiation from bolometry radiation for a possible HDH discharge (#54818).*
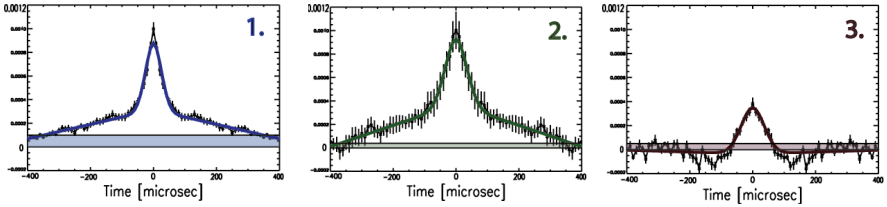
81

Figure 5-4 *Autocorrelation functions for the three time intervals near the separatrix (channel 9). The shaded area indicates the level of background contribution. The autocorrelation functions are corrected for the photon noise peak.*
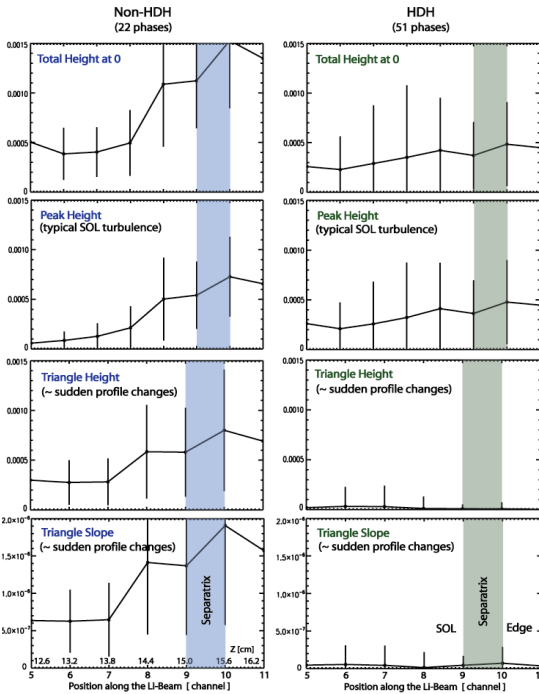

Figure 5-5 *Comparison of various fitted autocorrelation function parameters in the HDH and non-HDH phases along the Li-BES channels. The mean values are connected lines, whereas the error bar indicates the standard deviation through the whole dataset.*

The data were processed in more detail by fitting the autocorrelation functions in all the available Li-beam signals with the above described combination of triangular and Gaussian peaks. The mean and standard deviation of the parameters were calculated for each channel across all shots in the database. Comparison of the 22 non-HDH and 55 HDH phases is shown in figure 5-5. The radial profiles of four fitted autocorrelation function parameters are shown for the available Lithium beam channels (in cm and channel number):

- *total height:* total height of the *raw* autocorrelation function at $\tau=0$,
    i.e. the RMS amplitude of the raw signal
- fitted *triangle height and slope:* height and slope of the triangle-like phenomenon,
    i.e. of the two linear 'triangle' function.
- *peak height:* height of the peak-like phenomenon, i.e. fitted Gaussian function.

Studying the characteristics of the autocorrelation function of Li-beam light fluctuations, two separate phenomena were observed in the SOL-edge region of the plasma (up to about 1cm inside the separatrix): peak-like phenomenon resembling SOL turbulence and triangle-like features caused by sudden profile changes. When comparing the two datasets, the disappearance of sudden profile changes and slight change of the SOL turbulence can be observed in the HDH phase. Besides these two phenomena however no additional mechanism could be identified that may have a role in the impurity flushing feature of the HDH phases. The Fourier analysis of the Li-BES signals did not show the signature of any other relevant instability either.

5.2 Magnetic field fluctuations – Mirnov coil studies
5.2.1 Categorization of magnetic oscillations

Several HDH discharges, including the series used in the Li-beam study, were analyzed concerning the magnetic field fluctuations measured by the Mirnov coil arrays. Density and heating power scans, different magnetic configurations and plasma material (H, D) were studied. Time-frequency analysis of the magnetic perturbations indicated three types of mode activity in the HDH regime:

a, *Low Frequency Oscillations (LFO):* principle frequencies below 50 kHz with higher harmonics as well. This MHD mode is not unique for the HDH phase, it is also present in the quiescent H-mode phase (QH), an ELM-free H-mode phase prone to impurity accumulation, before the HDH transition. Thus these modes were not investigated further.

b, *Quasi-Coherent Modes (QC):* narrow band oscillations in the 50-150 kHz frequency range. The QC modes appear in the Mirnov signals only in the HDH phase just at the transition to HDH as shown in figure 5-6a, thus became the primary focus of this work.

c., *High Frequency Oscillations (HFO):* in some cases higher frequency modes (200-350 kHz) can be found in the Mirnov signals sampled at 1MHz. These modes appear in HDH phases, but are not continuously present. As the high time resolution Mirnov measurement was only available for a short time window (~20ms) in the middle of the HDH phase, thus unfortunately not much information could be obtained on the high frequency modes and its relation to the impurity transport could not be established. During the HFOs, QC modes were also observed on the normal Mirnov channels.
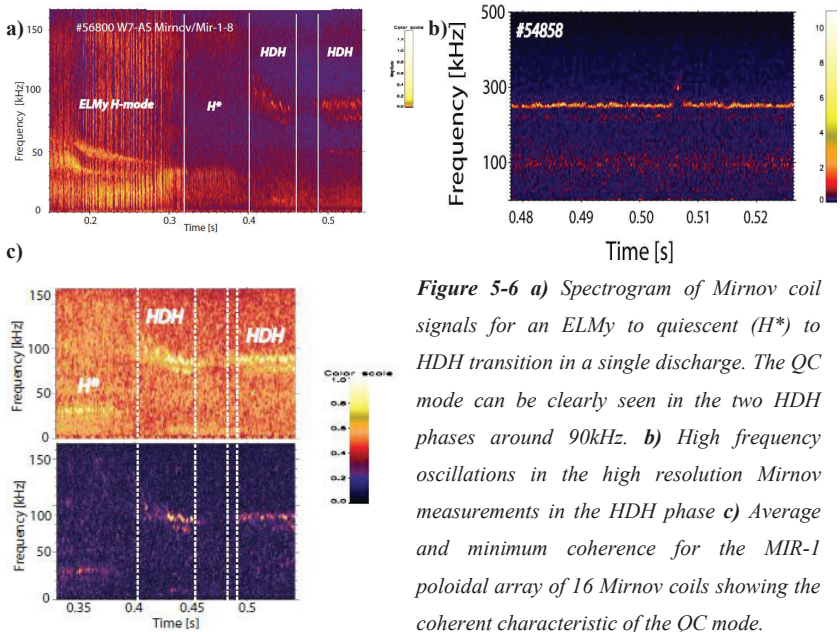
Figure 5-6 a) Spectrogram of Mirnov coil signals for an ELMy to quiescent (H*) to HDH transition in a single discharge. The QC mode can be clearly seen in the two HDH phases around 90kHz. b) High frequency oscillations in the high resolution Mirnov measurements in the HDH phase c) Average and minimum coherence for the MIR-1 poloidal array of 16 Mirnov coils showing the coherent characteristic of the QC mode.

5.2.2 Characterization of the quasi-coherent mode

Best results on the QC modes were obtained studying a series of 20 discharges, where the magnetic configuration was optimized to increase the plasma volume, i.e. the mean minor radius was increased to a=14.07 cm in contrast to the usual values of 11-11.5 cm. This made a drastic different when analyzing magnetic fluctuations with Mirnov coils, as the amplitude of

MHD modes decays exponentially, and thus the additional 2.5 cm could improve the detection of possible instabilities substantially.

The experiments described here is a series of dedicated 20 discharges (#56775-56810) carried out in D plasma with 2 MW NBI heating at an iota value of ι=0.55. Overview of the main plasma parameters compared to a reference quiescent H-mode are shown in figure 5-7.
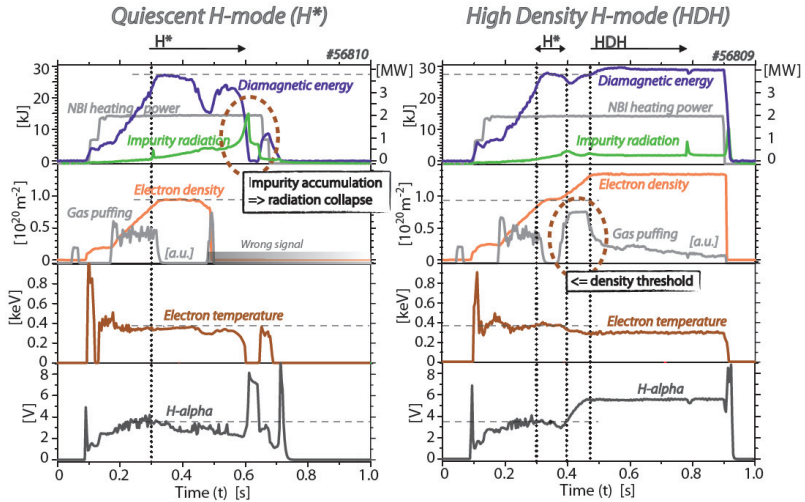

Figure 5-7 *Main plasma parameters of a typical H* and HDH discharge*

The sole difference between the technical setup of the two discharges in figure 5-7 is the additional gas puff at 0.4s to push the plasma over the density threshold into the HDH regime. The quiescent phase ends in radiation collapse due to the accumulated impurities (indicated by the fast increase of the impurity radiation at about 0.6s). The discharge #56809 in the figure comprises of the three typical H-modes of W7-AS starting with the ELMy H-mode phase (~0.2-0.3s), then transitioning into an ELM-free H* mode (~0.3-0.4s) showing rapid impurity accumulation, finally into the stable quasi-stationary HDH phase (~0.48-0.9s). In HDH the steady-state total plasma radiation P_{rad} indicates no impurity accumulation whereas the higher energy content (W) at constant heating power (P_{NBI}) is also a sign of the enhanced energy confinement time ($\tau_e \sim P_{NBI}/W$).

The magnetic equilibria of the large plasma series (figure 5-8) shows that the separatrix is formed by the naturally occurring magnetic islands. This is generally the case at edge iota values of ι_a=5/m with m=8,9,10.., where 5 is due to the five-fold toroidal symmetry of the device. Figure 5-8 shows the location of the low (MIR-1, 350kHz) and high (MIR354, 1MHz) resolution Mirnov channels in relation to the plasma as well.
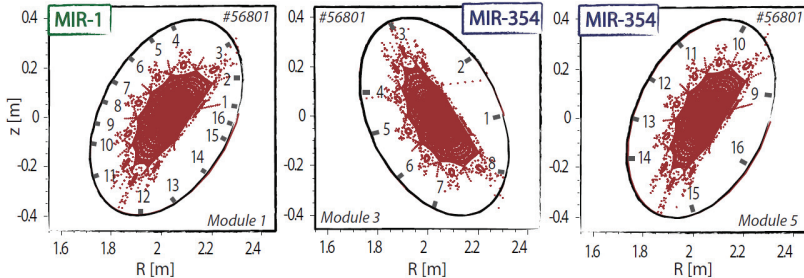

Figure 5-8 *The MIR-1 and MIR-354 poloidal Mirnov coil array setup and magnetic reconstruction of flux surfaces at the cross-section of the Mirnov coil arrays for #56801*

5.2.2.1 Relation to impurity transport

Appearing only in the HDH phase, the key question was the relation of the QC modes to the impurity behavior. Figure 5-9 shows a Mirnov signal spectrogram on the transition from quiescent H-mode to HDH mode just after 0.39s with a short back transition around 0.45s to 0.47s that can be clearly seen on the included impurity radiation. Two modes can be observed in the HDH phase (at 78kHz and 90kHz), where the higher frequency mode correlates well with the onset of the HDH phase, that is, it appears when the impurity radiation increase stops (~0.39s). The mode amplitude decreases significantly in the phase (~0.45-0.47s) where the discharge falls out of the HDH regime. A slightly lower frequency mode appears a bit later, its frequency and amplitude variation is similar to the first mode. This behavior of the first mode is studied in detail in figure 5-10. The upper figure shows the frequencies values where the frequency corresponding to the maximum spectral amplitude for a given time point agrees in at least 10 (grey boxes) and 13 (orange boxes) MIR-1 channels out of 16 channels respectively, i.e. it shows the mode frequency that is present in at least 10 and 13 MIR-1 Mirnov channels. The middle figure shows the mean bandpower corresponding to the frequency band shown on the previous figure between dotted lines. Finally the lower figure shows the time evolution of the impurity radiation.
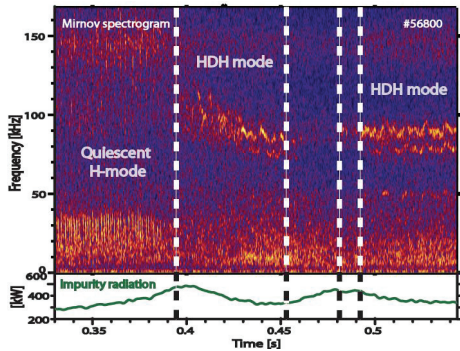
Figure 5-9 Mirnov spectrogram and corresponding impurity radiation from the bolometry signal for a quiescent H-mode to HDH transition showing the appearance of the QC mode.
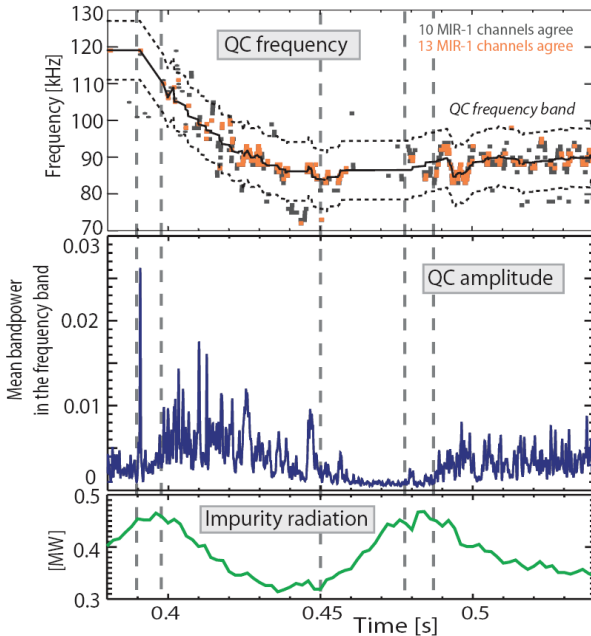

Figure 5-10 Relation of the QC frequency and mean spectral amplitude to the impurity radiation showing good correlation.

The dashed lines in figure 5-10 indicate changes in the impurity behavior as follows:

- 1-2 (0.39 and 0.4s): rolling over and decrease of radiation by entering the HDH phase correlating with the first burst and the following increase in the QC amplitude. The QC mode sweeps down from 120kHz to 90kHz.

- 3 (0.45s): increase of the radiation, backtransition to quiescent H-mode. The QC mode amplitude is very low.

- 4-5 (0.43 and 0.44s): roll over, decrease and stabilization of the radiation by entering the HDH phase again corresponding to a burst and following increase and stabilization of the QC amplitudes at 90 kHz.
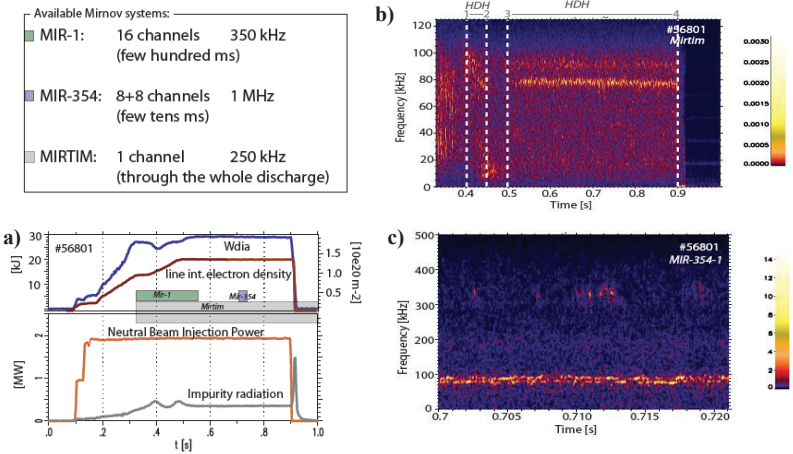
Figure 5-11 a) Overview plot of the plasma parameters for a HDH discharge including the impurity radiation. The available measurement windows for the different Mirnov coil arrays are also indicated. b) Spectrogram of the low resolution Mirnov coil signal . c) Spectrogram of the high resolution MIR-354 Mirnov coil array showing the QC mode throughout the time window and some burst of HFOs around 330kHz.

In the followings the higher frequency mode (sweeping down from 120kHz-90kHz) will be called the QC mode, whereas the lower frequency mode at 78kHz will be denoted the accompanying mode. The presence of the QC mode and its amplitude changes correlate well with the impurity behavior that is at the first burst of the mode, the impurity radiation stops and with increasing amplitude the radiation reduces. Furthermore small burst in the amplitude

correspond to sudden drops in the impurity signal. This is a remarkably good correlation of the QC modes amplitude with the impurity radiation change, making it a prime candidate for the impurity flushing mechanism. It should however be noted that this does not resolve the question, whether the QC modes are responsible for the impurity transport or whether they are just accompanying effect of the real mechanism.

It is important to check whether the QC mode is present through the whole HDH phase and whether the disappearance of the mode also correlates with the HDH-H mode transition. These two points are presented in the following two figures.

The QC mode is present through the whole HDH phase as shown on the only Mirnov channel (lowest time resolution) available throughout the discharge on figure 5-11. The figure indicates the measurement time windows for the different Mirnov coil arrays on a plasma discharge overview plot (figure 5-11a) and shows the corresponding Mirnov spectrograms for the available Mirnov arrays. The QC mode present is present on all of diagnostics in the HDH phase.
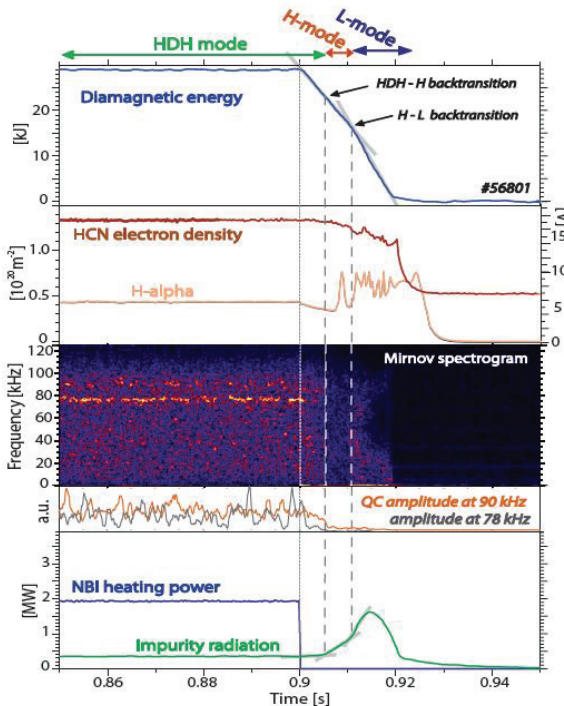
Figure 5-12

Overview plot of the global plasma parameters at the end of the discharge: the diamagnetic energy, electron density from the HCN inter-ferometry, H_α, NBI heating power and impurity radiation. The figure includes the spectrogram of the magnetic fluctuations and the time evolution of the mode amplitudes for the same time period.

Also in order to gain more insight into dynamics of the QC mode and define the driving force behind it, the end phase of the discharge has been studied in detail as shown in figure 5-12. The NBI heating is shut down at 0.9s, and after 5ms the plasma leaves the HDH regime and the impurities start to accumulate anew. At 0.911s the back transition to L-mode can be clearly observed in the change of the diamagnetic energy. The Mirnov signal spectrogram and the amplitude of the QC and the accompanying mode are shown as well. The accompanying mode disappears just after switch off of the NBI system, whereas the QC mode only disappears after the HDH to H* transition. This shows again a very good correlation with the HDH phase strengthening the belief that it can have a significant role in the HDH regime. This result also indicates that accompanying mode at 78kHz is a different mode, as they seem to have different driving mechanism.

5.2.2.2 Localization

The next step was the poloidal and radial localization of two modes at 90kHz and 78kHz (after the frequency stabilizes). Figure 5-13a shows the Poincare plot of the magnetic equilibrium for this plasma series of 20 discharges and indicates the position of the coils in the MIR-1 array. The normalized spectral amplitudes of the two modes are plotted over the Mirnov channels in figure 5-13b for each discharge (dashed lines) separately. The bold green and orange lines represent the average over the 20 discharges for the two modes respectively. Channel 10 is thought to be a broken channel showing no mode activity at all in other discharges and phases as well. Generally it can be said that the two modes show quite a different poloidal amplitude distribution. While the first mode at 90 kHz (showing the good correlation with the impurity behaviour) seems to be detectable on the inboard side where the magnetic islands are present, the lower frequency mode at 78kHz (appearing slightly after the HDH transition) is localized at other poloidal angles. This supports the assumptions that the two modes, the QC mode and the accompanying mode are of different nature.

For radial localization of the QC mode and further information other fluctuation diagnostics such as Li-BES previously and reflectometry, ECE, H-alpha, SXR in addition have also been checked. Unfortunately mainly due to high electron densities, none of them sees the pedestal area and/or they cannot resolve the frequency regime in question. Nonetheless the mode is believed to reside in the pedestal close to the plasma edge. As shown above the Li-beam does not see this mode, therefore it is not located outside the separatrix. On the other hand it should not be too deep in the plasma as the Mirnov coils could still detect them.
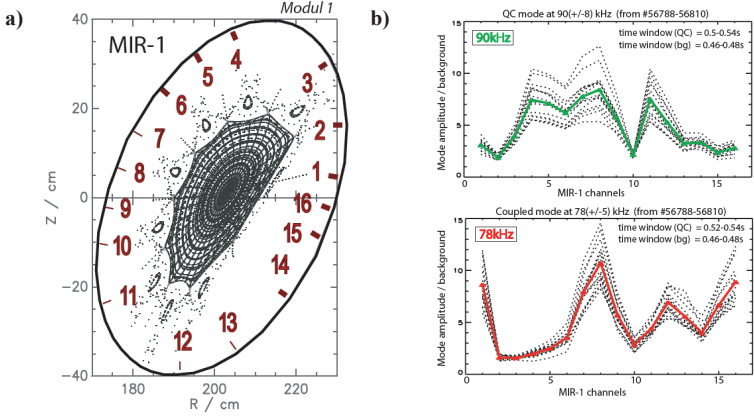
Figure 5-13 a) *Typical plasma equilibrium for the large plasma series and location of the MIR-1 Mirnov coil array.* ***b)*** *Respective and average QC amplitude for the 90 and 78kHz modes respectively.*

5.2.2.3 Mode number

Determination of the mode number have been attempted from the three poloidal Mirnov coil arrays (16, 8 and 8 channels respectively) by time-windowed Fourier decomposition of the signals and analyzing the relative phase shift of the fluctuations. No poloidal mode number could however be obtained, indicating a higher value that the limited number of Mirnov channels could resolve (up to ~ 6). A reciprocating probe housing two poloidal field pick-up coils (MRCP) (figure 5-14), based on the concept of Snipes et al [80], has been inserted into the plasma measuring the radial decay of the magnetic field perturbations along the distance to the separatrix as shown in figure 5-15 in a few discharges showing two modes very similar to the large-plasma series.

As shown in figure 5-15 the amplitude of the modes falls off rapidly, in about 2 cm-s, with the distance from the separatrix with an exponential decay length of k_r~2.82 ($\pm$0.78) cm^{-1} and k_r~ 3.18 ($\pm$0.79) cm^{-1} respectively corresponding to the 90 kHz and 110 kHz modes (by fitting exp(-k_r·r) to the experimental data). By assuming a field aligned perturbation and using the Laplace equation outside the fluctuating current layer (method described in [80]) as it is the case for the MRCP probe, $k_r \approx k_{pol}$ (as $k_t \sim k_{pol} \cdot 0.037$ can be neglected). Thus using this rapid radial decay of the amplitude a rough estimate of the poloidal mode number at that position is around m ~ 40. This is clearly outside of the poloidal resolution of the Mirnov coil system.
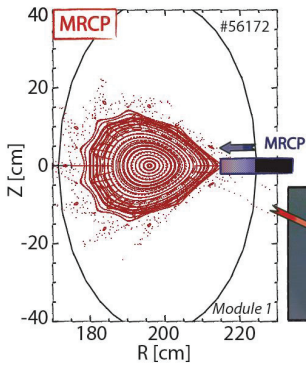
Figure 5-14 *Poincaré plot of the plasma cross-section corresponding to discharge #56172 and of the reciprocating Mirnov probe (MRCP). The probe is inserted slowly into the plasma as indicated by the blue shaded area and arrow.*
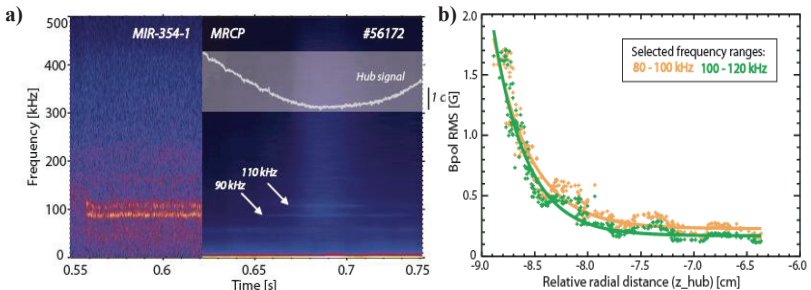

Figure 5-15 (a) *Spectrogram of the magnetic fluctuation measured by the high resolution Mirnov coil array and the MRCP coil including the Hub signal showing the relative distance of the MRCP coil to the separatrix. **(b)** Radial decay of the magnetic fluctuations measured by the MRCP probe in the frequency range of the QC modes respectively.*

5.3 Discussion

Several plasma discharge series have been analyzed with dedicated parameter scans such as density scans for given heating power, magnetic configurations and isotope plasmas (Hydrogen or Deuterium plasmas). Regarding magnetic fluctuations there are two main issues to consider that hindered further analysis:

a) Due to the high mode number and thus the magnetic perturbation amplitude falling off rapidly with distance from the plasma this mode is very hard to detect in magnetic fluctuations in any small cross-section plasmas. Thus the detection and/or the reconstruction of the poloidal structure for identification are not possible.

92

b) The frequency resolution of the long measurement window MIRTIM signal is only 125kHz, very close to the observed frequency of 120-90kHz. Thus even a slight increase in frequency has the result that the mode cannot be detected on this signal, and thus cannot be identified as QC.

The data from the small cross-section plasmas are thus inconclusive as even if some modes could be detected, there is no way to distinguish between QC mode and a possible accompanying mode close in frequency. Thus no further information on the QC mode can be obtained from previous measurements and as the W7-AS stellarator has been shut down and dismantled, new experiments cannot be planned and executed.

Nonetheless the close correlation in the dynamics of the QC mode and the impurity radiation supports the picture that the QC mode can play a key factor in the impurity transport and thus in reducing the impurity concentration in HDH plasmas. The observed QC mode is around 90-120kHz with high poloidal mode number around 40 at the outer midplane. No higher harmonics could be detected. It can be poloidally best observed in the inboard side around the magnetic island structure at the toroidal segment of the MIR-1 Mirnov coil array. Regarding the radial localization, it is likely to reside in the plasma edge inside the separatrix, based on the facts that

- the Li-BES cannot detect it, thus it has to reside inside the separatrix
- it has to be close to the edge as with its high mode number and thus short fall off length otherwise it could not be detected, e.g. in small cross-section plasmas.

Comparing these properties and behaviour to observations in different devices, it can be noted that this mode is similar to the QC modes of the EDA regime of Alcator C-mod and quite different from the EHOs in the Quiescent H-modes of DIII-D or ASDEX Upgrade. In case of the ALCATOR C-mod EDA plasmas were modelled with the BOUT turbulence code and the QC modes were identified as a type of ballooning mode, a resistive X-point mode. Unfortunately turbulence codes are just making the first steps in modelling the complex 3D structure and non-axisymmetry of stellarators. The high density gradients in the edge and the stochasticity of island field line structure make the HDH regime a hard challenge. Hopefully the increase in computational power, development in stellarator turbulence codes and/or experimental results from the new Wendelstein 7-X stellarator will shed new light onto the physics of this promising operational regime and the QC modes.

Summary

Results I.

High Field Side Pellet Studies

A pellet database has been established for Deuterium pellets injected from the high field side of the ASDEX Upgrade and Tore Supra tokamaks, called HFS-PAD database, covering a wide range of plasma and pellet parameters. Statistical analyses performed on the ASDEX Upgrade dataset indicated the importance of five parameters in the ablation process, i.e. electron temperature, pellet mass and velocity, magnetic field and elongation of the plasma (in order of statistical significance). An empirical penetration depth scaling was derived for HFS pellet injections and the results were compared with two theoretical models, the NGS model and the numerical Hybrid ablation code, respectively (the comparison was based on a typical ASDEX Upgrade H-mode electron temperature and density profile). The obtained empirical HFS scaling shows some features that are broadly consistent with these theoretical models; however it differs from them in emphasizing the importance of the magnetic field and plasma elongation in the ablation process. Also in contrast to current ablation theories, the presented scaling (as well as other empirical scalings from IPADBASE) suggests a negligible role for the electron density. It was, however, not the aim to provide an extensive benchmark for these theories. For this, further detailed analysis of the dataset (and an extension of temperature profile information) is needed. For the magnetic field dependence dedicated discharges have been carried out to provide single-parameter scans for the magnetic field and the electron temperature, the foremost penetration depth dependence. The results of these experiments support the previous statistical results.

This contribution is a first step in a study to define an utilizable empirical HFS penetration depth scaling to support the ITER HFS pellet injection system. A tentative extrapolation for the pellet penetration depths in ITER-sized devices has been made, under two explicit, but rather arbitrary, assumptions of the scaling with respect to the size of the machine. However, a reliable HFS penetration depth scaling with size of the machine, preferred for ITER, can clearly not be realized from data from one machine alone, thus a future extension of the database with data from other tokamak devices is required.

In contrast to the present limitations the developed database is suitable for predicting the penetration of pellets into the pedestal region for ELM triggering, thus it is useful for designing a particle control scheme with pellet triggered ELMs on ITER.

Results II.

High Density H-mode Studies

In high density H-mode (HDH) plasmas of the Wendelstein 7-AS stellarator, an ELM-free stable H-mode with high confinement properties, electron density and magnetic field fluctuations were analyzed to find a mechanism that might be responsible for the low impurity concentration of this regime. The studies were carried out using Lithium beam emission spectroscopy and Mirnov coil arrays. Whereas the electron density fluctuations revealed no additional phenomenon, the magnetic measurements indicated an appearance of a quasi-coherent mode just after the transition to HDH. The close correlation in the dynamics of this QC mode and the impurity radiation supports the picture that the QC modes are the key factors in reducing the impurity concentration in HDH plasmas.

The observed QC mode frequency is around 90-120kHz with high poloidal mode number around 40 at the outer midplane. No higher harmonics could be detected. It can be poloidally best observed in the inboard side around the magnetic island structure at the toroidal segment of the MIR-1 Mirnov coil array. The best estimate for its radial location is the pedestal area in the plasma edge. At the Alcator C-Mod tokamak, similar QC modes are known to be responsible for the impurity transport in the ELM-free, stable high density H-mode regime, i.e. the Enhanced D-alpha (EDA) H-mode.

At this time, no definite answer can be given whether the QC mode is the mechanism responsible for the enhanced impurity transport in the HDH regime or it is a by-product of the real mechanism. More information cannot be obtained at the present, but hopefully the new Wendelstein stellarator W7-X, to be started in 2014, will be able to provide new insight into this fascinating regime.

Acknowledgements

First of all I would like to thank you my supervisor Sándor Zoletnik for taking me on as his PhD student and supporting me throughout the years. I would also like to thank Peter Lang for his guidance and encouragement, and Otto Kardaun for his thoughtful help and teaching me that statistics can be more than interesting. Also I would like to thank Prof. Karl Lackner for the valuable discussions. I had a very nice time with all the pellet groups, Paul, Christian and Wolfgang at ASDEX Upgrade, Alain and Nicola at Tore Supra and Daniel, Paul and Robin at JET.

In Greifswald I would like to thank Henning Thomsen for spending hours with me debugging all my accounts and codes and Matthias Hirsch for all the interesting discussions. I would like to thank all the colleagues and friends in Greifswald for giving me such a warm welcome there and always having time for me to discuss details long forgotten. I am especially grateful to Prof. Fritz Wagner who took the time to discuss with me at every visit giving me invaluable hints to HDH regime. On the same topic in Garching, I would like to thank Kent McCormick for his insights and valuable comments regarding this 'fairy tale' regime.

I would like to give a special thank to Kinga Gál for her continuous help throughout the years and assistance day and night. I am grateful to have her as my friend. I would also like to thank Tünde Fülöp for her encouragement and support.

I have had a great time with my friends both from the university Gergely Patay, Juli Fekete, Évi Madarász and István Cziegler and from my old school Balázs, Nóri, Viki, Ádám, Kuci, Matyi who provided me who were always there to cheer me up.

In Hungary I would also like to thank all my colleagues among others Attila Bencze, Tamás Fehér, Gábor Molnár for the nice time at the institute and Gábor Kocsis and Sándor Kálvin for the valuable discussions on pellet physics. I would like to thank Gergő Pokol and Gergely Papp for the nice collaboration on these magnetic modes, being a great help. Also I am very thankful for Nóra Sándor supporting me in the last days of writing with company, programs and snacks.

Finally, but not least I would like to thank my family who were always there to support me. I am grateful for Tibi for the encouragement and for my aunt Etu, providing safe heaven for me either in her home or among thousands of books. I thank Duarte, for the time together and all his great improvisations that balance and inspire me.

This thesis I would like to dedicate to my mom, without her love and support I would not be where I am today.

Publication List

First Authorship

1.   E. Belonohy, O.J.W.F. Kardaun, T. Fehér, K. Gál, S. Kálvin, G. Kocsis, K. Lackner,
     P.T. Lang, J. Neuhauser and the ASDEX Upgrade Team
     „A high field side pellet penetration depth scaling derived for ASDEX Upgrade"
     Nuclear Fusion **48** (2008) 065009
     (refereed journal, impact factor: 3.303, 3 independent out of 4 citations)

(2.) E. Belonohy, M. Hirsch, K. McCormick, G. Papp, G. Pokol, H. Thomsen, S. Zoletnik
      and the W7-AS Team
      „Quasi-coherent mode in the high density H-mode regime of Wendelstein 7-AS"
      to be submitted

Co- Authorship

1.   J. Egedal, W. Fox, E. Belonohy and M. Porkolab
     „Kinetic Simulation of the VTF Magnetic Reconnection Experiment"
     Computer Physics Communications **164** (2004) 29-33
     (1 citation)

2.   K. Gál, E. Belonohy, G. Kocsis, P.T. Lang, G. Veres and the ASDEX Upgrade Team
     „Role of shielding in modeling cryogenic deuterium pellet ablation"
     Nuclear Fusion, **48** (2008) 085005
     (refereed journal, impact factor: 3.303, 2 independent citations)

3.   P.T. Lang, K. Lackner, M. Maraschek, B. Alper, E. Belonohy, K. Gál, J. Hobirk,
     A.Kallenbach, S. Kálvin, G. Kocsis,C.P. Perez van Thun, W. Suttrop, T. Szepesi,
     R. Wenninger, H. Zohm, the ASDEX Upgrade Team and JET-EFDA contributors
     „Investigation of pellet-triggered MHD events in ASDEX Upgrade and JET"
     Nuclear Fusion, **48** (2008) 095007
     (refereed journal, impact factor: 3.303, 9 independent out of 11 citations)

4.   S. Zoletnik, M. Agostini, E. Belonohy, G. Bonhomme, D. Dunai, P. Lang, P. Garcia-Martinez,
     A.D. Gurchenko, C. Hidalgo, A. Kendl, G. Kocsis, C. Maszl, K. McCormick, H. W. Müller,
     S. Spagnolo, E. Solano, S. Soldatov, M. Spoalore, Y. Xu
     „Summary of the Workshop on Electric Fields, Structures ans Self-organisation in Magnetized
     Plasmas (EFTSOMP) 2009. 6-7 July, 2009, Sofia, Bulgaria"
     Nuclear Fusion,**50** (2010) 047001
     (refereed journal, impact factor: 3.303)

5.   P.T. Lang, K. Lackner, M. Maraschek, B. Alper, E. Belonohy, K. Gál, J. Hobirk,
     A.Kallenbach, S. Kálvin, G. Kocsis,C.P. Perez van Thun, W. Suttrop, T. Szepesi,
     R. Wenninger, H. Zohm, the ASDEX Upgrade Team and JET-EFDA contributors
     „ELM pacing investigations at JET with the new pellet launcher"
     Nuclear Fusion, **51** (2011) 033010
     (refereed journal, impact factor: 3.303, 4 independent citations)

Publication in refereed conference proceedings

First Authorship

1. <u>E. Belonohy</u>, G. Pokol, K. McCormick, G. Papp, S. Zoletnik and the W7-AS Team
   „A Systematic Study of the Quasi-Coherent Mode in the High Density H-mode Regime
   of Wendelstein 7-AS"
   PLASMA2007 –
   Greifswald, Germany, 2007
   AIP Conference Proceedings **993** (2007) 39-42

Co- Authorship

1. G. Kocsis, <u>E. Belonohy</u>, K. Gal, S. Kalvin, P.T. Lang, W. Schneider, G. Veres
   and the ASDEX Upgrade Team,
   „Pellet-Plasma Interaction at ASDEX Upgrade"
   PLASMA2005 - International Conference on Research and Applications of Plasmas
   Opole-Turawa, Poland, 2005
   AIP Conference Proceedings **812** (2005) 191-194

Talks, presentations

Oral Contribution at a Conference

1. „A Systematic Study of the Quasi-Coherent Mode int he High Density H-mode Regime of
   Wendelstein 7-AS"
   PLASMA2007 – International Conference on Research and Applications of Plasmas
   October 2007, Greifswald, Germany

Presentations at Workshops and Meetings

1. „The HFS Penetration Depth Scaling"
   Pellet Workshop
   July 2004, IPP Garching, Germany

2. „The High Field Side Pellet Injection Database at ASDEX Upgrade"
   ITER Pellet Injector Design Review Meeting
   April 2005, ITER Garching Joint Work Site, Garching, Germany

3. „Systematic Study of Density Fluctuations on W7-AS"
   3rd Hungarian Plasma Physics and Fusion Technology Workshop
   April 2006, Visegrád, Hungary

4. „Anomalous transport events on the W7-AS stellarator"
   10th Workshopon Electric Fields, Structures and Relaxation in Plasmas
   June 2007, Warsaw, Poland

5. „Quasi-Coherent Signature of the High Density H-mode at the W7-AS Stellarator"
4rd Hungarian Plasma Physics and Fusion Technology
March 2008, Győr, Hungary

6. „Quasi-Coherent Modes in the High Density H-mode of the W7-AS Stellarator"
EFTSOMP2008 – Workshop on Electric Fields, Turbulence and Self-Organisation in Magnetized Plasmas, Satellite Meeting of the 35th EPS Conference on Plasma Physics
June 2008, Hersonissos, Crete, Greece

7. „High Field Side Pellet Database and Penetration Depth Scaling – A Statistical Approach"
Fuelling of Magnetic Confinement Machines Workshop, Satellite Meeting of the 35th EPS Conference on Plasma Physics
June, 2008, Hersonissos, Crete, Greece

8. "Pellet Penetration Depth Scaling Studies"
EFDA Meeting on Fuelling and Particle Control
March 2009, IPP Garching, Germany

9. "Quasi-Coherent Activity in ELM-free H-modes"
EFTSOMP2009 – Workshop on Electric Fields, Turbulence and Self-Organisation in Magnetized Plasmas, Satellite Meeting og the 36th EPS Conference on Plasma Physics
July 2009, Sofia, Bulgaria

10. "Experimental investigations of pellets at JET"
Pellet operations meeting
September 2009, JET, Abingdon, UK

Seminars

1. „Pellet Injection Database and Scaling Studies on the ASDEX Upgrade tokamak"
CRPP Seminar, June 2005
Centre de Recherches en Physique des Plasmas, Lausanne, Switzerland

2. „Pellet-ablációs adatbázis felépítése és vizsgálata"
(Development and Study of the Pellet Ablation Database)
Plasma Physics Seminar, November 2005
KFKI-RMKI Plasma Physics Department, Budapest, Hungary

3. „High Field Side Pellet Database and Scaling Studies – An Application of Statistical Methods in Plasma Physics"
ASDEX Upgrade Seminar, July 2006
Max-Planck-Institut für Plasmaphysik. Garching, Germany

Other publications (conference proceedings, posters)

First Authorship

1. E. Belonohy, S. Kálvin, G. Kocsis, P.T. Lang, D. Reich and U. Vogl
    „Analysis of HFS Pellet Injection at the ASDEX Upgrade Tokamak"
    Annual Meeting of the Hungarian Physical Society
    Szombathely, Hungary, 2004

2. E. Belonohy, S. Kálvin, O. Kardaun, G. Kocsis, K. Lackner adn P.T. Lang
    „High Field Side Pellet Injection Database and Penetration Depth Scaling"
    DPG2005 – 69th Annual Meeting of the German Physical Society
    Berlin, Germany, March 2005

3. E. Belonohy, S. Kalvin, O. Kardaun, G. Kocsis, K. Lackner, P.T. Lang and
    the ASDEX Upgrade Team,
    „High Field Side Penetration Depth Scaling Studies at ASDEX Upgrade"
    32nd EPS Conference on Plasma Physics
    Tarragona, Spain, June 2005
    Europhysics Conference Abstracts **29C** (2005), P-2.097

4. E. Belonohy, A. Bencze, G. Papp, G. Pokol and S. Zoletnik
    „Systematic Density Fluctuation Study ont he W7-AS Stellarator"
    3rd CMPD & CMSO Winter School on Plasma Transport and Turbulence
    UCLA, Los Angeles, USA, January 2007

5. E. Belonohy, A. Bencze, G. Papp, G. Pokol, K. McCormick, S. Zoletnik and the W7-AS Team
    „Density and Magnetic Fluctuation Studies ont he Wendelstein 7-AS Stellarator"
    34th EPS Conference on Plasma Physics
    Warsaw, Poland, June 2007
    Europhysics Conference Abstracts **31F** (2007) P-2.046

    (*3 independent citations*)
    PPCF Student Poster Prize (Magnetic Confinement Section)

6. E. Belonohy, M. Hirsch, K. McCormick, G. Papp, G. Pokol, H. Thomsen, A. Werner,
    S. Zoletnik and the W7-AS Team
    „Edge Instabilites in the High Density H-mode operation of W7-AS"
    35th EPS Conference on Plasma Physics
    Hersonissos, Crete, Greece, June 2008
    Europhysics Conference Abstracts 23D (2008), P2.034

7.. E. Belonohy, M. Hirsch, K. McCormick, G. Papp, G. Pokol, H. Thomsen, A. Werner,
    S. Zoletnik and the W7-AS Team
    „Quasi-Coherent Modes in the High Density H-mode Regime of W7-AS"
    18th International Toki Conference – Development of Physics and Technology of
    Stellarators/Helitrons en route to DEMO
    Ceratopia Toki, Japan, December 2008

8. E. Belonohy, K. Gál, O. Kardaun, P.T. Lang, B. Lovász and the ASDEX Upgrade Team
    "Magnetic field dependence of pellet penetration"
    37th EPS Conference on Plasma Physics
    Dublin, Ireland, June 2010
    Europhysics Conference Abstracts 34A (2010) P5-143

Co- Authorship

1. S. Kalvin, <u>E. Belonohy</u>, K. Gal, G. Kocsis, P.T. Lang, G. Veres and
    the ASDEX Upgrade Team,
    „Investigations of Cryogenic Pellet Cloud Dynamics"
    31st EPS Conference on Plasma Physics
    London, United Kingdom, June 2004
    Europhysics Conference Abstracts **28G** (2004) P-5.150

2. S. Kalvin, <u>E. Belonohy</u>, K. Gal, G. Kocsis, P.T. Lang, G. Veres and
    the ASDEX Upgrade Team,
    „Investigation of Pellet-Plasma Interaction on ASDEX Upgrade"
    32nd EPS Conference on Plasma Physics
    Tarragona, Spain, June 2005
    Europhysics Conference Abstracts **29C** (2005), P-2.078

3. P.T. Lang, K. Lackner, B. Alper, <u>E. Belonohy</u>, D. Frigione, K. Gál, A. Geraud, L. Garzotti,
    G. Kocsis, T. Loarer, A. Loarte, M. Maraschek, G. Saibene, R. Sartori, J. Schweizer,
    T. Szepesi, R. Wenninger, H. Zohm, ASDEX Upgrade Team and JET-EFDA contributors
    „Investigating pellet phyics for ELM pacing and particle fuelling in ITER"
    22nd IAEA Fusion Energy Conference
    Geneva, Switzerland, October 2008

4. D. Frigione, L. Garzotti, E. Giovannozzi, F. Koechl, P.T. Lang, B. Alper, E. Belonohy,
    A. Boboc, K. Gal, G. Kocsis, Y. Liang and JET-EFDA contributors
    "Particle deposition, transport and fuelling in pellet injection experiments at JET"
    23rd IAEA Fusion Energy Conference
    South-Korea, October 2010

5. P.T. Lang, B. Alper, <u>E. Belonohy</u>, D. Frigione, K. Gál, G. Kocsis, K. Lackner,
    T. Loarer, M. Maraschek, F.M. Poli, G. Saibene1, S.E. Sharapov, T. Szepesi,
    R. Wenninger, H. Zohm, ASDEX Upgrade Team and JET-EFDA contributors
    "Pellet investigations related to ITER ELM pacing and particle fuelling"
    35th EPS Conference on Plasma Physics
    Hersonissos, Crete, Greece, June 2008
    Europhysics Conference Abstracts 23D (2008), P1.101

6. L. Garzotti, P.T. Lang, A. Alonso, B. Alper, <u>E. Belonohy</u>, A. Boboc, S. Devaux,
    T. Eich, D. Frigione, K. Gál, A. Géraud, G. Kocsis, F. Köchl, K. Lackner,
    A. Loarte, P. J. Lomas, M. Maraschek, H. W. Müller, G. Petravich, G. Saibene,
    J. Schweinzer, H. Thomsen, M. Tsalas, R. Wenninger and JET-EFDA contributors
    "Investigating pellet ELM triggering physics using the new small size pellet launcher at JET"
    37th EPS Conference on Plasma Physics
    Dublin, Ireland, June 2010
    Europhysics Conference Abstracts 34A (2010) P5-143

7. P.T. Lang, W. Suttrop, <u>E. Belonohy</u>, R. Fischer, J. Hobirk, O.J.W.F. Kardaun, G. Kocsis,
    B. Kurzan, M. Maraschek, P. deMarne, A. Mlynek, P.A. Schneider, T. Szepesi, E. Wolfrum,
    and the ASDEX Upgrade Team
    „High density H-mode operation by pellet injection and ELM mitigation with the new active
    in-vessel saddle coils in ASDEX Upgrade"
    38th EPS Conference, Strasbourg, France, June 2011
    Europhyics Conference Abstracts 35G (2011) O3.112

Notations

References

[1] J. Wesson, Tokamaks 2nd edition (The Oxford Engineering Science Series - 48), Oxford University Press, Oxford 1997

[2] P.M. Bellan, Fundamentals of Plasma Physics, Cambridge University Press, 2006

[3] Fusion – an energy option for the future, CD-ROM, Association Euratom – FOM2005

[4] Intergovernmental Panel on Climate Change (IPCC) Fourth Assessment Report: Climate change 2007: The Physical Science Basis, (editors: S. Solomon, D. Qin, M. Manning)

[5] IPP Summer University for Plasma Physics, Greifswald 2005 (editors: H.W. Müller, M. Hirsch)

[6] Key World Energy Statistics 2010, International Energy Agency (http://www.iea.org/textbase/nppdf/free/2010/key_stats_2010.pdf)

[7] E. J. Doyle *et al.* 2007 *Nuclear Fusion* **47** S18

[8] Fusion Science and Technology Special Issue: ASDEX Upgrade, *2003 Fusion Science and Technology* **44** 569, (editor: A. Herrmann)

[9] M. Hirsch *et al.* 2008 *Plasma Physics and Controlled Fusion* **50** 053001

[10] E. Marmar *et al.* 2009 *Nuclear Fusion* **49** 104014

[11] H.W. Müller *et al.* 1999 *Physical Review Letters* **83** 2199

[12] Kupschus P. *et al* 1997 *Europhysics Conference Abstracts* **21A**, part I (ECA) 45

[13] P.T. Lang *et al* . 2003 *Nuclear Fusion* **43** 1110

[14] Baylor L, Geraud A. *et al.* 1997 *Nuclear Fusion* **37** 445

[15] K. McCormick *et al.* 2002 *Physical Review Letters* **89** 015001

[16] F. Wagner *et al.*1982 *Physical Review Letters* **49** 1408

[17] V. Erckmann *et al* 1993 *Physical Review Letters* **70** (14) 2086

[18] H. Biglari *et al.* 1990 *Physics of Fluids B* **2** 1

[19] M. Greenwald 2002 *Plasma Physics and Controlled Fusion* **44** R27

[20] ITER Physics Basis 1999 *Nuclear Fusion* **39** 2175

[21] F. Troyon *et al.* 1984 *Plasma Physics and Controlled Fusion* **26** 209

[22] U. Stroth *et al.* 1996 Nuclear Fusion **36** 1063

[23] Wagner, F. *et al* 1982 *Proceedings of the Thirteenth Conference on Plasma Physics and Controlled Nuclear Fusion Research (IAEA, Vienna)*, vol. I, pp. 277-90.

[24] J.W. Connor *et al.* 1998 *Physics of Plasmas* **5** 2687

[25] P.B. Snyder *et al.* 2004 *Nuclear Fusion* **44** 320,

[26]   G.T.A. Huysmans *et al.* 2001 *Physics of Plasmas* **8** 4292

[27]   D. Thomas *et al.* 2005 *Physics of Plasmas* **12** 056123

[28]   A. Burckhart *et al.* 2010 *Plasma Physics and Controlled Fusion* **52** 105010

[29]   P.B. Snyder *et al.* 2007 *Nuclear Fusion* **47** 961

[30]   ASDEX Team 1989 *Nuclear Fusion* **29** 1959

[31]   T.E. Evans *et al.* 2004 *Physical Review Letters* **92** 235003

[32]   P.T. Lang *et al.* 2004 *Nuclear Fusion* **44** 665

[33]   A. Herrmann *et al.* 2002 *Plasma Physics and Controlled Fusion* **44** 883

[34]   K. H. Burrell *et al.* 2002 *Plasma Physics and Controlled Fusion* **44** A253

[35]   K.H. Burrell *et al.* 2009 *Nuclear Fusion* **49** 085024

[36]   W. Suttrop *et al.* 2003 *Plasma Physics and Controlled Fusion* **45** 1399

[37]   W. Suttrop *et al.* 2004 *Plasma Physics and Controlled Fusion* **46** A151

[38]   N. Oyama *et al.* 2005 *Nuclear Fusion* **45** 871

[39]   W. Suttrop *et al.* 2005 *Nuclear Fusion* **45** 721

[40]   P.B. Snyder *et al.* 2004 *Nuclear Fusion* **44** 320

[41]   P.B. Snyder *et al.* 2005 Physics of Plasmas **12** 056115

[42]   M**.** Greenwald *et al.* 1997 *Nuclear Fusion* **37** 793

[43]   M. Greenwald *et al.* 2000 *Plasma Physics and Controlled Fusion* **42** A263

[44]   J.A. Snipes *et al.* 2001 *Plasma Physics and Controlled Fusion* **43** L23

[45]   X.Q. Xu *et al.* 2000 *Physics of Plasmas* **7** 1951

[46]   A. Mazurenko *et al.* 2002 *Physical Review Letters* **89** 225004

[47]   J. Myra *et al.* 2000 *Physics of Plasmas* **7** 4622

[48]   R.E. Slusher *et al.* 1984 *Physical Review Letters* **53** 667

[49]   G. R. Tynan *et al.* 1994 *Physics of Plasmas* **1** 3301

[50]   H. Ninomiya *et al.* 2002 *Fusion Science and Technology* **42** 7

[51]   K. Kamiya *et al.* 2003 *Nuclear Fusion* **43** 1214

[52]   L. Giannone *et al.* 2002 *Plasma Physics and Controlled Fusion* **44** 2149

[53]   K. McCormick *et al.* EPS2003 *Europhysics Conference Abstracts* Vol. **27A** P-1.1

[54]   S.L. Milora *et al.* 1995 *Nuclear Fusion* **35** 657

[55]   B. Pegourie 2007 *Plasma Physics and Controlled Fusion* **49** R87

[56]   K. Gál *et al.* 2008 *Nuclear Fusion* **48** 085005

[57]   P.B. Parks *et al.* 1977 *Nuclear Fusion* **17** 539

[58]   P.B. Parks and R.J. Tumbull 1978 *Physics of Fluids* **21** 1735

[59]   L.L. Lengyel *et al.* 1999 *Nuclear Fusion* **39** 791

[60] A. Canton *et al.* 2001 *Plasma Physics and Controlled Fusion* **43** 225

[61] Bevington P R, Data reduction and error analysis, McGraw-Hill, New York 1969

[62] P.T. Lang *et al.* 1997 *Physical Review Letters* **79** 1487

[63] Special Issue on Plasma Diagnostics for Magnetic Fusion Research
      2008 *Fusion Science and Technology* **53** Vol 2 281

[64] P. T. Lang *et al.* 2003 *Review of Scientific Instruments* **74** 3974

[65] C. Andelfinger *et al.* 1993 *Review of Scientific Instruments* **64** 983

[66] T. Szepesi *et al.* 2007 *Europhysics Conference Abstracts* Vol. **31I** P4.037

[67] O.J.W.F. Kardaun, 2005 *Classical Methods of Statistics* Springer Verlag

[68] Fuller W.A. 1987 *Measurement Error Models* (New York: Wiley)

[69] K. McCormick *et al.* 1996 *IPP Report* IPPIII/21

[70] S. Zoletnik *et al.* 1998 *Plasma Physics and Controlled Fusion* **40** 1399

[71] S. Zoletnik *et al.* 1999 Physics of Plasmas **6** 4239

[72] G. Pokol *et al.* 2007 *Plasma Physics and Controlled Fusion* **49** 1391

[73] L. Garzotti *et al.* 2010 *Europhysics Conference Abstracts* Vol. **34A** P2.131

[74] D. H. McNeil 1989 *Journal of Nuclear Materials* **162–164** 476

[75] O.J.W.F. Kardaun *et al.* 2004 *Europhysics Conference. Abstracts* Vol. **28G** P5.145

[76] K. Büchl *et al.* 1987 *Nuclear Fusion* **27** 1939

[77] Progress in the ITER Physics Basis 2007 *Nuclear Fusion* **47** S1

[78] ITER Technical Basis1999 *Nuclear. Fusion* **39** 2137

[79] V. Mukhovatov *et al.* 2003 *Nuclear Fusion* **43** 942

[80] J. A. Snipes *et al.* 2001 *Plasma Physics and Controlled Fusion* **43** L23

Kivonat

A fúziós plazmafizika egyik legfontosabb feladata a fúziós berendezésekben a szennyezőprobléma megoldása az első kísérleti fúziós reaktor kísérlethez, az ITER-hez vezető úton. A plazmaösszetartás javulásával a szennyezők, jelenleg főként a plazmát körülvevő szilárd felszínekből származó részecskék összegyűlnek a plazma belsejében kisugározva annak energiáját, ami az esetek többségében a plazmakisülés végét jelenti. A fúziós reakció során keletkező hélium eltávolítása szintén alapvető feladat. A szennyezők ellenőrzött ki- és befelé irányuló transzportja gyakran a plazmaszél egyik instabilitásához köthető. A leggyakrabban használt plazmaszél instabilitás az ún. Edge Localised Mode (ELM), ami periodikusan anyagot juttat ki a plazmából ezzel biztosítva a megfelelő transzportot. Megfelelő irányítás nélkül azonban az ELM jelentős hőterhelést jelent a berendezés belső falaira, ami a berendezés jelentős károsodásához vezethet akár pár napra is lecsökkentve egy fúziós reaktor élettartamát.

Az egyik fejlesztés alatt álló módszer az ELM-ek ellenőrzött kezelésére fagyott hidrogénizotóp jégdarabkák, ún. pelletek belövése a plazmába. A pelletek ELM-ek keltésével megsokszorozzák azok előfordulását, ezzel csökkentve méretüket és a belső falra érkező hőterhelést. A pelletek másik alapvető alkalmazási területe a fúziós reakció során felhasznált anyag utánpótlása. A berendezés nagy mágneses terű (HFS - High Field Side), azaz belső oldaláról való belövés esetén a pelletről leváló sűrű anyagfelhő a plazma belseje felé gyorsul a grad B drift hatására, ami az anyagutánpótlási teljesítmény jelentős növekedéséhez vezet. Ez alapján az ITER fúziós reaktor jelenleg elfogadott anyagutánpótlási módszere a pellet belső, nagy mágneses oldalról való belövése. Mind az anyagutánpótlásban, mind az ELM-ek keltésében kulcsszerepet játszik a pelletek behatolási mélysége. A dolgozatom egyik célja ezért egy több fúziós berendezést átölelő nemzetközi adatbázis létrehozása HFS pellet eseményekre, amely tartalmazza a pelletek adatai mellett a fontosabb plazmát leíró paramétereket is. Az adatbázis a német ASDEX Upgrade és a francia Tore Supra fúziós berendezések pelletkísérleteire épül. Az ASDEX Upgrade berendezés adatait statisztikai módszerekkel vizsgálva meghatároztam a pelleket behatolási mélységének parametrikus függését, majd a felállított kísérleti HFS pellet behatolási mélység skálát összehasonlítottam a jelenleg elfogadott elméleti modellekkel (semleges felhő árnyékolás modellel és a numerikus Hibrid pellet ablációs kóddal). A mágneses tértől való függést, melyben a statisztikai eredmények jelentősen eltértek az jelenlegi elméletektől kísérletileg is igazoltam az ASDEX Upgrade berendezésen folytatott pelletkísérletekkel.

A dolgozat második fele a transzport szabályzás egy másik, ELM-mentes megoldásával foglalkozik. A magas sűrűségű H-mód a német Wendelstein 7-AS berendezés különlegesen szép, stabil ELM-mentes operációs tartománya, melyben a szennyező részecskéket a belépés után a plazma azonnal kisöpri magából. Ezekben a kisülésekben az ELM instabilitás transzportnövelő hatását egy másik jelenség helyettesíti. A dolgozatban ezt az alacsony szennyező-koncentrációért felelős mechanizmust kerestem és bemutatok egy rendkívül ígéretes jelöltet, a kvázi-koherens módust. Az instabilitás alapvető leírása mellett vizsgálom a szennyezősugárzással való kapcsolatát. Az eredményeket végül összehasonlítom más berendezések hasonló instabilitásaival.

Abstract

The accumulation of impurities in fusion devices is one of the most severe problems in modern fusion plasma physics en route to ITER, the first experimental fusion reactor experiment. The presence of high Z impurity ions coming mainly from the surrounding solid surfaces can give rise to significant radiation losses of the plasma energy that may cause the plasma discharge to end abruptly. Diluting the fuel, the concentration of Helium from the fusion reaction is another problem to be solved. The methods under investigation to control the impurity influx and provide an outward transport commonly involve instabilities of the plasma edge, such as the Edge Localized Modes (ELMs). Although ELMs provide sufficient periodical outward transport of particles, they also pose a grave danger to the device if uncontrolled by their large heat loads onto the first wall elements.

Presently one of the methods under development for ELM control is the injection of small cryogenic hydrogen isotope cubes, called pellets into the plasma. The pellets trigger ELMs thereby increasing the frequency of ELMs and reducing their size and magnitude. Injection of pellets from the inner side that is the High Field Side (HFS) of the device is also the established main fuelling method foreseen for the ITER device. In case of HFS injections the ablating material is accelerated toward the center of the plasma due to the grad B drift, thereby increasing the fuelling efficiency significantly. The penetration depth of the pellet is a key parameter in both cases, in ELM control and fuelling. The thesis thus describes an effort to set up an international multi-machine database of HFS pellet injection events regarding their main and the respective plasma parameters based on the German ASDEX Upgrade and French Tore Supra fusion experiments. In case of the ASDEX Upgrade dataset the parametric dependences of the penetration depth has been investigated and an empirical HFS penetration depth scaling has been established. The results are compared to recognized pellet ablation theories (Neutral Gas Shielding – NGS model and the numerical Hybrid pellet ablation code). Furthermore dedicated experiments have been carried out at ASDEX Upgrade regarding the magnetic field dependence in which case theory and experimental results disagree, supporting the experimental results.

The second half of the thesis focuses on a different, ELM-free way of handling the impurity problem. The High Density H-mode (HDH) is a special, stable ELM-free operational scenario of the German Wendelstein 7-AS fusion device, where impurities are immediately flushed out of the plasma upon entering. The thesis here revolves around the search for the mechanism responsible for the low impurity concentration in this regime and presents a promising candidate instability, the Quasi-Coherent (QC) mode. The characteristics of this mode and relation to the impurity behavior are explored. Finally the results are compared to instabilities showing similar behavior at other fusion devices.